Reconfigurable Tunable Microwave Devices Using Liquid Crystal

by

Pouria Yaghmaee

B. Eng (Electrical Engineering-Electronics)
Tehran University-Azad Central, Iran, 2006

M. Eng (Telecommunication Engineering)
The University of Adelaide, Australia, 2008

Thesis submitted for the degree of

Doctor of Philosophy

in

School of Electrical & Electronic Engineering
Faculty of Engineering, Computer & Mathematical Sciences
The University of Adelaide, Australia

July, 2014

THE UNIVERSITY
of ADELAIDE

DEDICATION

"I dedicate this thesis to my wife, Hedy, for without her love and support none of this would have happened".

"To my parents and sister whom always supported me both emotionally and financially".

Contents

Abstract

During the past decades, the applications of communication devices have extended widely, from AM radio receivers initially to newly developed GPS, smart mobile phones, radars, wireless LANs, satellite communications and implantable medical devices. The shortage in the available frequency spectrum for radio communications, the demand for portable wireless devices, and the requirement for more functionality in an even smaller volume, requires the development of new concepts in RF technology. One ideal pathway towards development of such new concepts is reconfiguration.

Today, due to the rapid progress in material science and electronic technology, there is great possibility in designing reconfigurable portable wireless devices which are frequency tunable, flexible and consume low energy. In this thesis, the anisotropic properties of liquid crystals in their nematic phase are exploited as a low-voltage (< 35 V) mechanism for designing tunable wireless devices at a low microwave frequency (L to C-band). To demonstrate the possibility of using liquid crystal technology, three different design approaches were pursued: a liquid crystal tunable resonator, a tunable band-pass liquid crystal filter, both at S-band, and liquid crystal tunable frequency selective surfaces operating at C-band. The results from full-wave electromagnetic simulations, lumped-element circuit models and prototype measurements in all cases indicate around 3.1 to 8.2% of continuous frequency tuning with low insertion loss (< 1 dB).

Given that liquid crystals material are transparent, commercially obtainable and are the only liquid material with tunable characteristics at microwave frequency, they could be ideal, in conjunction with flexible electronics, for designing either external or internal implantable microwave devices where flexibility is of great concern.

Statement of Originality

This work contains no material that has been accepted for the award of any other degree or diploma in any university or other tertiary institution and, to the best of my knowledge and belief, contains no material previously published or written by another person, except where due reference has been made in the text.

I give consent to this copy of the thesis, when deposited in the University Library, being available for loan, photocopying, and dissemination through the library digital thesis collection, subject to the provisions of the Copyright Act 1968.

I also give permission for the digital version of my thesis to be made available on the web, via the University's digital research repository, the Library catalogue, the Australasian Digital Thesis Program (ADTP) and also through web search engines.

Signed

Date

Acknowledgements

I would like to express my deep gratitude to my principal supervisor, Adjunct Prof Bevan Bates. He expressed promptness and concern since my very first email to him, and that has been unchanged throughout the period under his supervision. His friendly and encouraging attitude has been helpful for propelling my work. Bevan's industrial way of thinking inspired me to approach the problems in more practical ways.

A key person whom I am strongly indebted to is my co-supervisor, Professor Christophe Fumeaux. His long experience with microwave frequency design has been of great importance towards my research. He has always given critical and vital comments upon the drafts, without which I would have not been able to complete this thesis. I have endured many hard times in thoroughly revising the drafts to satisfy his strict requirements, but eventually it turned out that it was worth doing so. The best word to describe him would be 'precision and quality research'.

Thanks are also due to all colleagues in the Applied Electromagnetic Research Group, Mr Ali Karimi, Mr Amir Ebrahimi, Mr Shifu Zhao, Mr Longfang Zou, Mr Gerard Rankin, Mrs Echo Niu, Mrs Zahra Shaterian, Dr Withawat Withayachumnankul and Dr Thomas Kaufman under supervision of Professor Christophe Fumeaux. Their critical comments and suggestions towards my presentations and research, not only enhanced my professional knowledge, but also provided a warmth and comfortable environment throughout my PhD research. I particularly would like to acknowledge, Dr Thomas Kaufman, Dr Withawat Withayachumnankul, Mr Ali Karimi, Mr Mehdi Kasaei Kopaei and Mr Amir Ebrahimi, for their ideas, fruitful discussion and assistance towards measurements in the anechoic chamber. It is my pleasure to have great moments with them.

I owe very much to Institute for Microwave Engineering and Photonics people at the Technische Universität Darmstadt (TUD) in Germany under supervision of

Professor Rolf Jakoby, particularly Dr Onur Hamza Karabey who assisted me in the laboratory for fundamental experiments. Significant suggestions were also contributed by Dr Mohsen Sazeghar from TUD and Mr Atsutaka Manabe from Merck KGaA, Darmstadt, Germany.

Other sources of support and assistance, especially towards prototype fabrication has been provided by the Defence Science and Technology Organisation (DSTO), especially Mr Igor Switala, the Australian National Fabrication Facility (ANFF), the Ian Wark Research Institute at University of South Australia, Mr Simon Doe and Mr Dipankar Chugh and Macquarie University in Sydney, Mr Ben Johnston.

During my candidature, administrative work has been assisted by Ms Rose-Marie Descalzi, Mrs Ivana Rebellato, Ms Jodie Schluter, Mr Danny Di Giacomo, and Mr Stephen Guest. Other supporting people include the technical officers, Mr Pavel Simcik, Mr Bradon F. Pullen, Mr Alban O'Brien and Mr Ian Linke, and the IT support officers, Mr Ryan King, Mr David Bowler and Mr Mark J. Innes. The person who helped augment my academic writing skill in the early days was Karen Adams. Major financial support has been provided by Australian Postgraduate Award Scholarship (APA) and Australian Research Council (ARC), under the Discovery Project DP120100661. Travel grants were from the School of Electrical & Electronic Engineering, the University of Adelaide.

Finally deep appreciation goes towards my precious wife (Hedy Minoofar), for her constant love and support towards my research and study. She was there from my first step into the PhD, in the stressful moments, until the final stage, caring, encouraging and cheering me to reach my goals and dream. Without her constant help and love, I would have not reached this stage. Last but not least, I would like to express my appreciation to my parents (Bijan Yaghmaee and Farideh Yaghmaei) and my sister (Pegah Yaghmaie), who always endow me with infinite support. Their voice and advice has given me happiness and success in both professional and social life. No words can fully explain my gratefulness to them.

P. Yaghmaee

Conventions

Typesetting This thesis is typeset using Microsoft word, 2007.

Referencing The IEEE style is used for referencing and citation in this thesis.

Spelling Australian English spelling is adopted, as defined by the Macquarie English Dictionary (Delbridge 2001).

System of units The units comply with the international system of units recommended in an Australian Standard: AS ISO 1000-1998 (Standards Australia Committee ME/71, Quantities, Units and Conversions 1998).

Physical constants The physical constants comply with a recommendation by the committee on Data for Science and Technology: CODATA (Mohr and Taylor 2005).

Frequency bands Microwave frequency bands are defined according to "IEEE Standard Letter Designations for Radar-Frequency Bands," IEEE Std 521-2002 (Revision of IEEE Std 521-1984).

Publications

[1] **P. Yaghmaee,** O. H. Karabey, B. Bates, C. Fumeaux, and R. Jakoby, "Electrically tuned microwave devices using liquid crystal technology," *International Journal of Antennas and Propagation,* vol. 24, pp. 25-35, September 2013. (Chap. 1-2), Journal

[2] **P. Yaghmaee**, T. Kaufmann, B. Bates and C. Fumeaux, "Effect of polyimide layers on the permittivity tuning range of liquid crystal," *IEEE European Conference on Antennas and Propagation (EuCap)*, pp. 3579-3582, March 2012. (Chap. 3), Conference

[3] **P. Yaghmaee,** C. Fumeaux, B. Bates, A. Manabe, O. H. Karabey and R. Jakoby, "Frequency tunable S-band resonator using nematic liquid crystal," *IET Electronics Letters*., vol. 48, no. 13, pp. 798-800, June, 2012. (paper was selected for the "in brief" section of the journal, under Wireless Communications - Body Tuning) (Chap. 4), Journal

[4] **P. Yaghmaee**, A.K. Horestani, B. Bates and C. Fumeaux, "A multi-layered tunable stepped impedance resonator for liquid crystal characterization," *IEEE Asia-Pacific Microwave Conference (APMC)*, PP. 776-778, December 2012. (Chap. 5), Conference

[5] **P. Yaghmaee**, W. Withayachumnankul, A.K. Horestani, A. Ebrahimi, B. Bates and C. Fumeaux, "Tunable electric-*LC* resonators using liquid crystal," *IEEE International Symposium on Antenna and Propagation (AP-S/USNC-URSI)*, July 2013. (Chap. 6), Conference

[6] **P. Yaghmaee,** B. Bates, and C. Fumeaux, "Liquid crystal tunable frequency selective surfaces for microwave frequency switching," in preparation. (Chap. 6), Journal

[7] **P. Yaghmaee,** H. Minoofar, "Electric-*LC* resonators at microwave for oil sensing," accepted in *IET Electronics Letters*. (Chap. 6), Journal

[8] A. Ebrahimi, **P. Yaghmaee**, W. Withayachumnankul, C. Fumeaux, S. Al-Sarawi and D. Abbott, "Interlayer tuning of X-band frequency-selective surface using liquid crystal," *IEEE Asia-Pacific Microwave Conference Proceeding (APMC)*, pp. 1118-1120 November 2013. (Future work), Conference

[9] M. Mohammadzaheri, S. Grainger, M. Bazghaleh and **P. Yaghmaee**, "Intelligent modelling of a piezoelectric tube actuator," *IEEE International Symposium on Innovations in Intelligent Systems and Applications (INISTA)*, pp. 1-6, July 2012.* Conference

[10] A. Ebrahimi, and **P. Yaghmaee**, "A new enhanced differential CMOS colpitts oscillator," *Journal of Circuits, Systems, and Computers*, November 2013.* Journal

Note: Articles with an asterisk are not directly relevant to this thesis

Lists of Figures

List of Tables

Chapter 1

Reconfiguration Mechanisms and Techniques

RECONFIGURATION in a microwave device provides additional levels of functionality for communication systems, enables adaptation with changing system requirements and reduces restrictions caused by environmental conditions. Reconfiguration of frequency response, polarization, and radiation pattern can be achieved through electrical, mechanical, material or other means. This chapter reviews various reconfiguration mechanisms and provides insight into fundamental design approaches to advanced techniques, followed by practical examples that offer important new capabilities for next-generation applications.

1.1 Introduction

Antennas, resonators and filters are essential and critical components for communication and radar systems. In the past century these devices have been developed and enhanced, in terms of their structure, frequency range and their potential applications, especially in the microwave frequency range. The microwave application of these devices varies, from GPS and mobile phones to radars, wireless LAN, satellite communications and more recently biomedical devices. However due to recent demand for portable lower power consumption devices and the development of material science, there is undoubtedly a need for reconfigurable devices with flexibility and frequency tunability.

According to the Oxford, Cambridge and Electronic dictionaries the verb "reconfigure" is defined as "to configure (something) differently", "to arrange something differently" and "to design or adapt to form a specific configuration or for some specific purpose". For this thesis the word reconfigure is defined as:

> "To design or adapt a device in order to form a specific configuration or for some specific purpose".

Passive microwave devices can be categorized into antennas, phase shifters and delay lines, frequency selective surfaces (FSS), resonators and filters. When faced with a new system design, engineers will combine, change and adapt these devices, using theoretical knowledge and general design guidelines as starting points. This allows the development of new structures that produce acceptable results. For example, reconfigurable antennas for portable wireless devices can help to improve a noisy connection or redirect transmitted power to conserve battery life. In large phased arrays, reconfiguration could be used to provide additional capabilities that may result in wider instantaneous frequency bandwidths, more extensive scan volumes, and radiation patterns with more desirable side lobe distributions [20].

According to Bernhard [20] an ideal cost-effective reconfigurable device should be able to alter its *frequency response, polarizations*, and *radiation pattern* independently to accommodate changing operating requirements. These reconfigurations require various mechanisms and their own practical techniques each with their own advantages and disadvantages for a particular application. Some of these techniques [20] that are more relevant to this thesis are discussed below and classified in Table 1.1.

Table 1.1. Studies of various reconfiguration techniques. This table provides a brief overview of frequency response, polarization, radiation pattern and compound methods to achieve reconfiguration and highlights the key mechanisms and techniques.

Reconfiguration	Reconfiguration Mechanisms	Techniques	
Frequency response reconfiguration	Switches Variable reactive loading Structural/mechanical changes Material changes	MEMS switches PIN diodes FETs Optical switches Piezoelectric actuators	Varactors Ferrites Ferroelectrics Liquids Liquid Crystal
Polarization reconfiguration	Switches Material changes	MEMS actuators/switches PIN diodes Ferrite	
Radiation pattern reconfiguration	Structural/mechanical changes Electrical changes Material changes	Piezoelectric actuators PIN diodes MEMS actuators/switches Varactors Ferrites Ferroelectrics	
Compound reconfiguration	Mixed mechanisms	Combination of various techniques *	

* Still a new topic with limited available literature

This chapter describes theory and fundamental design approaches for the above mentioned reconfiguration methods, based on results published to date. This description is followed by a discussion of the advantages of liquid crystals towards achieving frequency response reconfiguration, especially towards applications at low microwave frequencies.

1.2 Frequency response reconfiguration

In most references from the available literature, especially at microwave frequencies, the terms frequency response reconfiguration and frequency reconfiguration are also denoted as frequency response tuning or frequency tunability, since reconfiguration in a device is achieved through shifting the response (centre) frequency. Throughout this thesis the words "frequency tuning" are defined according to McGraw-Hill Science & Technology dictionary [21] as:

> "The process of adjusting [reconfiguring] the inductance or the capacitance or both in a tuned circuit…in order to obtain optimum performance at a selected frequency".

According to Petosa [22] frequency tuning can be classified into two main categories, discrete or continuous. In 2007, Bernhard [20] described discrete frequency tuning as a switching mechanism for operation at distinct or separated frequency bands, while continuous frequency on the other hand allows for smooth transitions between operating bands without skipping over frequencies. To achieve either method a number of mechanisms can be used to change the effective length of the antennas (Table 1.1). These methods are: *switches*, *variable reactive loading*, *structural/mechanical changes* and *material variations*.

1.2.1 Switches

The most common switching techniques used are microelectromechanical systems (MEMS) switches, PIN diodes, optical switches and FETs. Kiriazi et al. [23] demonstrated discrete tuning in a dipole antenna using MEMS switches. In this design through using series of MEMS switches, discrete frequency tuning between 4.86 and 8.98 GHz was achieved. A similar antenna type using silicon photo-conducting switches was also later designed in 2006 by Panagamuwa et al. [19]; in this case using the two silicon photo-conducting switches with infrared laser diodes

enabled resonant frequencies of 2.16 and 3.15 GHz, for closed and open switches respectively (Fig. 1.1).

Gupta et al. [24] illustrated the use of a coplanar waveguide (CPW) for discrete frequency tuning. In this model, the reconfiguration was carried out by switching appropriate slot-line lengths, which results in two operating frequencies at 3.0 and 8.3 GHz and a similar radiation pattern for both cases. Other common methods used for discrete tuning are PIN diodes, as illustrated by Peroulis et al. [25] for a single-fed resonator. The application of a bias voltage allowed changing the effective electrical length resulting in four different achievable resonant frequencies ranging from 540 to 890 MHz. Yang and Rahmat Samii [26] also displayed discrete switching using PIN diodes for microstrip switchable slots, where dual frequency tuning was achieved with unchanged polarization. All switching methods mentioned above share the common approach of discrete frequency tuning through changes in the effective length of a resonant element.

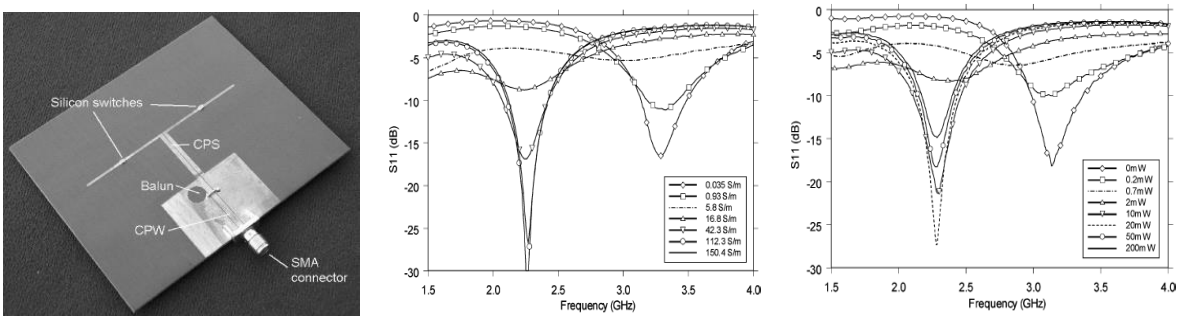

(a) (b) (c)

Figure 1.1. **Silicon switched dipole antenna.** (a) Image of the fabricated dipole antenna, (b) and (c) simulation and fabrication measurements respectively, illustrating resonant frequencies of 2.16 and 3.15 GHz, for closed and open switches for various silicon conductivities, from [19].

1.2.2 Variable reactive loading

Variable reactive loading has much in common with the previously discussed switching method. The only difference between the two is the mechanism used to change the effective length. Variable reactive loading generally allows for a smooth continuous transition, rather than a discrete frequency change. Schaubert et al. [27]

demonstrated in 1980 one of the first reconfigurable patch antennas using two varactor diodes. In this work applying a reverse bias voltage ranging from 0 V to a maximum of 30 V, caused capacitance variation and hence resulted in 50% continuous frequency tuning. In 1991, Kawasaki and Itoh [28] used a FET as a variable reactance to tune a slot antenna structure. A 10% frequency tuning was achieved around the frequency of 10 GHz as a result of altering the bias voltage.

Apart from FETs, MEMS capacitors can also provide an electrostatically actuated variable reactance. An article by Erdil et al. [18] showed discrete frequency shifting for a microstrip patch antenna at K_u-band using MEMS (Fig. 1.2). Moreover a small-sized monopole for micro frequency tuning was proposed by Jung et al. [29], with a PIN diode and a varactor incorporated into a meander-type radiator. The final designed prototype exemplifies discrete frequency switching between 2 and 5 GHz.

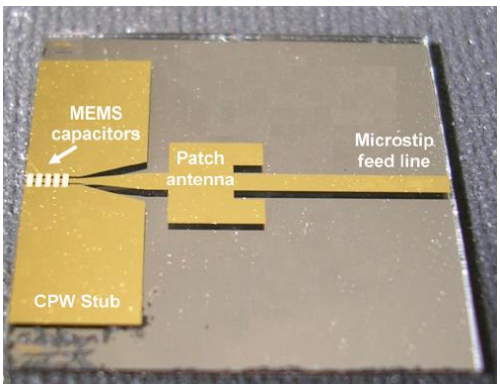

Figure 1.2. **Frequency tunable microstrip patch antenna.** Reconfigurability of the operating frequency is achieved by loading the resonant patch with a coplanar waveguide (CPW) stub on which variable MEMS capacitors are placed periodically. MEMS capacitors are electrostatically actuated with a low tuning voltage (0–11.9 V). The antenna resonant frequency can continuously be shifted from 16.05 GHz down to 15.75 GHz as the actuation voltage is increased from 0 to 11.9 V, from [18].

1.2.3 Structural/mechanical changes

Other practical methods used by researchers for frequency reconfiguration are structural/mechanical variations within the device. Structural changes can deliver larger frequency shifts, whether used for switched or continuous frequency tuning.

The main challenge in this type of tuning lies in changing the physical structure, but at the same time maintaining all other characteristics. An example of this type of tuning is presented in [30], where piezoelectric actuators provides movement of a parasitic element, resulting in an effective bandwidth of about 9%. In that particular realization, the bandwidth and gain of the structure also changed as a function of parasitic element spacing, but could not be individually selected. This example clearly illustrates the difficulty in achieving one kind of reconfigurability without incurring changes in other characteristics. Langer et al. in 2003 [31] also presented frequency variation in a antenna by means of a mechanical method. In their work, the application of an external DC magnetic field resulted in plastic deformation leading to frequency tuning at a microwave frequency.

1.2.4 Material variation

An alternative method for frequency reconfiguration is provided by material variation. Generally in this technique, an applied static electric field is used to change the relative permittivity and an applied static magnetic field is used to change the relative permeability of a material embedded in the devices. These changes in relative permittivity or permeability can result in frequency shifting. The main advantage of this method is the possibility of continuous frequency tuning. Furthermore, the materials used typically have high relative permittivities and permeabilities compared with other commonly used substrate materials, resulting in a size reduction. The most common materials that are frequently used for frequency shifting are ferrite, ferroelectric and more recently liquid crystals.

Pozar and Sanchez were the pioneers who used ferrite materials to achieve tunable devices. In 1988 [32] they demonstrated frequency reconfiguration using a ferrite substrate for a microstrip patch antenna. In their work they achieved 40% of continuous frequency tuning by varying the DC magnetic bias field applied to the ferrite substrate. Properties of ferrite have been further investigated [33, 34]

confirming a shift in the centre frequency through applying non-uniform bias fields and multiple modal field distributions.

A further type of material used for frequency tuning is ferroelectrics. Ferroelectric materials were first discovered by Valasek in Rochelle salt [35]. They are ceramic compounds with unique dielectric properties, i.e. high capacitance density and the ability to be constructed in a very small physical area. Ferroelectrics can be divided into two main categories, thick and thin films. Thick films have been used for several years for designing and manufacturing various large scale devices such as large industrial capacitors. Generally, they require large control voltage (1000 V) and have non-linear temperature behaviour, making them difficult to control. Thin films however maintain a very high capacitance density, making them practical for many applications. The main challenge of thin film applications comes in controlling the material deposition during the manufacturing process. Unlike MEMS, which require the physical mechanical movement of the capacitor plates, ferroelectric thin films require only a voltage change for capacitance adjustment. The capacitance changes simply by the movement of atoms within the material making a capacitance change nearly instantaneous [36].

Barium Strontium Titanate (BST) is a ferroelectric material of particular interest for tunable microwave devices, since it has a high relative permittivity due to a perovskite atomic structure. BST is essentially a solid solution of $BaTiO_3$ and $SrTiO_3$. The relative permittivity of BST can be tuned by applying a quasi-static electric field to the material. Under an applied field, the central Ti atom in the BST unit cell is displaced from its zero field position in the central TiO_6 octahedron. This displacement decreases the relative permittivity. The amount of displacement and therefore the tunability is affected by many factors, including temperature, Ba/Sr ratio and residual strain in the BST film [36, 37]. An example of RF application of BST thin films was presented in 2002 by Tombak et al. [38], based on voltage tunable capacitors. Using metalorganic chemical vapour deposition (MOCVD) method and using integrated thin-BST film, 71% voltage-controlled tunability was achieved.

A more recent work demonstrates using a BST thin film for designing a tunable coplanar waveguide shunt interdigitated capacitor (IDC) [39]. By applying a bias voltage ranging from 0-50 V, a resonant frequency shifting between 11.53-17.51 GHz was achieved. Applications of BST thick films are also illustrated in the literature. For example a band-pass filter based on split ring resonators (SRR) is described in [40], consisting of two SRR, which were tuned through embedded varactors built on BST thick-film ceramic. Results demonstrated frequency tuning between 2.8 and 3.1 GHz and insertion loss of less than 7.5 dB. Sezegar et al. [13] presented in 2011 two compact continuously tunable phase shifters based on screen printed BST thick films, as shown in Fig. 1.3. The proposed strategy provided a differential phase shift of more than 360° at 10 GHz.

In more recent work, published in 2012, Roig et al. [41] reported a tunable frequency selective surface as a transmission array with beam steering capability using a screen printed BST thick-film ceramic. The FSS was designed to behave as a band pass filter and was made tunable by loading it with a BST layer placed beneath the metallic structures. A maximum phase shift of 116˚ degrees was obtained at 10 GHz, while transmission and reflection levels were kept constant. Other examples of BST thick films have been demonstrated in [42, 43].

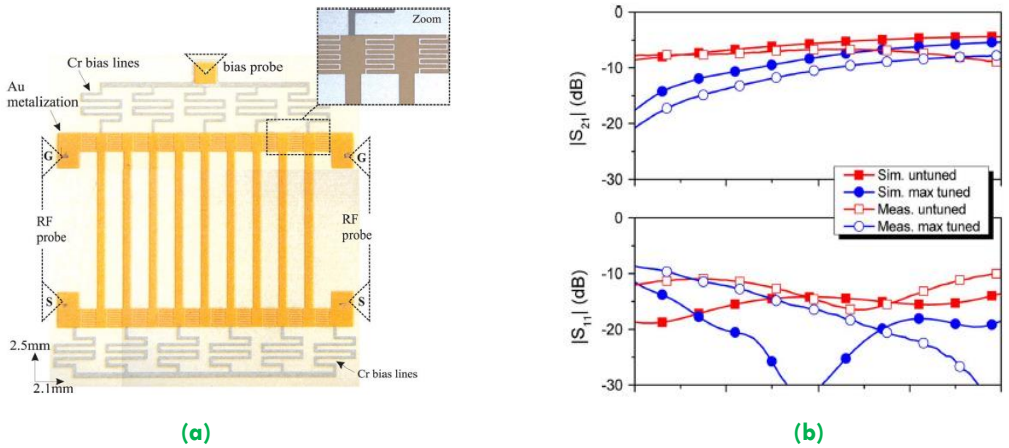

Figure 1.3. **Tunable phase-shifter fabricated on BST thick film.** (a) Photograph of the fabricated phase-shifter, (b) simulation and measurements results. The proposed designs have total lengths of 2.1 and 3.8 mm and provide a differential phase shift of more than 360° and a figure of merit of 51° /dB at 10 GHz, from [13].

1.3 Polarization reconfiguration

In 2000, Boti et al. [9] described polarization reconfigurability as a way to provide protection for interfering signals in varying environments, improve link quality by introducing an additional degree of freedom and for active read/write tracking and tagging applications. Bernhard [20] defined two main methods to achieve polarization reconfigurability, via through material properties variation and through changing the device structure. This type of reconfiguration can take place between different linear polarization right-handed/left-handed circular polarizations, or between linear and circular polarizations. The two methods that can be used to achieve these modifications are using *switches* and *material changes*. One of the main difficulties for polarization reconfigurability is achieving reconfiguration without significant changes to impedance or frequency characteristics of the communication device.

1.3.1 Switches

Various types of switches and material variations are illustrated in the literature. As an example, Fan and Rahmat-Samii [44] demonstrated switchable slots in a microstrip patch antenna with dual-frequency, dual-band circular polarization performance and circular polarization diversity. Furthermore they presented [45] a similar idea for two orthogonal slots incorporated into a patch, combined with two PIN diodes for switching the slots on and off. In their work, the diodes provided a switching option to radiate with either right-hand circular polarization (RHCP) or left-hand circular polarization (LHCP).

Switchable circular polarisation was also demonstrated by Boti et al. [9] using two-slot excitation and beam-lead PIN diodes located on both diagonals of the rectangular patch (Fig. 1.4). Fries et al. [46] used PIN diodes to achieve the switching required for polarization reconfiguration and demonstrated the operation with a prototype antenna. In this paper, switching is attained between linear and circular polarizations or between two circular polarizations using forward and reverse

biasing techniques. Apart from diodes, MEMs switches are also widely used for polarization reconfiguration. Using a MEM actuator within the microstrip patch was presented by Simons et al. [47], where the theory and practical results using MEMs actuators illustrated a circularly polarized radiation pattern.

1.3.2 Material variation

Commonly reported materials used for polarization reconfiguration are ferrite and ferrite films. Rainville and Harackiewicz, [48] used ferrite films to design a single feed antenna. In this study the applied static bias tuned the frequency of the cross-polarized field to create a range of elliptical polarizations.

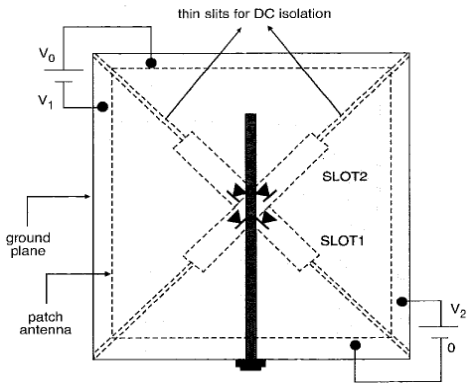

Figure 1.4. Circularly polarized patch antenna with switchable polarization sense.
Slot 1 is ON and Slot 2 is OFF for $V_1 = V_O$ and $V_2 = 0$ (RHCP),
Slot 1 is OFF and Slot 2 is ON for $V_1 = 0$ and $V_2 = V_O$ (LHCP), from [9].

1.4 Radiation pattern reconfiguration

Variation of the antenna current distribution directly determines the radiation pattern. This direct relationship between the current distribution and the resulting radiation pattern makes pattern reconfigurability difficult, but not impossible, to achieve. Three mechanisms can be used to achieve these modifications: *mechanical changes, electrical changes* and *material variation* [20]. The main challenge for radiation pattern reconfiguration is to achieve unchanged frequency characteristics or to compensate for the changes through impedance matching at the terminals.

1.4.1 Mechanical changes

Radiation pattern reconfiguration can be applied through the three methods above. The first of these approaches is mechanical modification, and has been used in [49] for a reflector antenna. In this research, changes in beam shape and direction were observed whilst changing the structure of the reflector. In a more recent work, Washington et al. [50] developed a novel reconfigurable dual-offset contour beam reflector antenna (DCBRA), with a thin flexible conductive sub-reflector. The overall study illustrated mechanical shape variation using a piezoelectric actuator to achieve the desired radiation pattern.

Beam-steering reflectors have a wide range of applications especially for defence. Between 2002 and 2005 Sievenpiper et al. presented a number of reflectors for radiation pattern reconfiguration. In 2002 [51] they created frequency dependent surfaces using an array of small resonators operating at 4.2 GHz. This surface enables reconfiguration of the surface reflection coefficient phase, which results in beam steering. A similar concept but with two-dimensional beam steering was also later realized using varactors [17], as shown in Fig. 1.5. Sievenpiper et al. demonstrated radiation pattern reconfiguration for a leaky wave antenna [52]. In this design, tuning the resonant frequency results in alteration of the tangential wave vector and therefore enables a scanning range of 45^0.

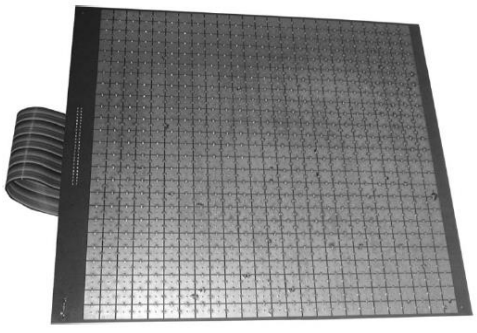

Figure 1.5. Electronically steerable reflector. 25 × 25 cells, with 1125 varactors, which are addressed in rows through the ribbon cable at the left edge. The electronically steerable reflector operates at 4.5 GHz, from [17].

1.4.2 Electrical changes

In 1999, Jung-Chih et al. [53] presented a reconfigurable Vee-antenna using RF-MEMS switches. In this design one end of the antenna is held by rotation hinge lock on the substrate, which allows the arm to rotate with the hinge as the centre of the circle. The antenna arms are pulled or pushed by support bars connected to the actuators with moveable rotation hinges on both ends, which results in beam-shape variation.

Apart from using mechanical changes, researchers have also used electrical changes for radiation pattern reconfiguration. From the practical examples found in the available literature, two main key methods have been used for electrical alterations: parasitic tuning and array tuning. Parasitic tuning is one of the most effective methods used for tuning radiation patterns independently of frequency, resulting in an range of functionalities and wide frequency bandwidth. Array tuning however can result in beam steering similar to traditional phased arrays, but without the inherent costs of phase shifters.

One of the first examples of parasitic tuning was proposed by Harrington [54] in 1978, for an N-port antenna. In this work Harrington controlled the antenna characteristic by impedance loading the ports and feeding one or several of the ports. Mobile communications antennas have also been tuned using parasitic elements [55, 56]. In the late 1984, a paper presented by Dinger illustrated the first realizations of parasitic tuning in a small planar array antenna [57].

In a more recent study in 2004 by Zhang et al. [58], a novel linearly polarized pattern tunable microstrip parasitic array was presented. In this design, the antenna uses four switches to tune the radiation pattern into three variations over a shared 2:1 VSWR bandwidth, which demonstrates potential applications in mobile communication devices and large phased arrays antenna.

Huff et al. [59] also developed a novel pattern and frequency tunable microstrip antenna with linear polarization at around 3.7 GHz which uses switched connections. In this structure one set of connections provided a re-directed radiation pattern while maintaining a common operating impedance bandwidth with the baseline configuration and the second set of connections resulted in operation at a higher frequency band at 6 GHz with broadside patterns. Similar studies but using MEMS switches are presented in the literature [11, 60].

1.4.3 Material variation

Variation of material characteristics can also be used to change resonant current distributions or can be simply used to alter propagation speeds, which in both cases can be exploited for radiation pattern reconfigurability. Henderson et al. [61] illustrated the first case of using ferrite materials for altering the radiation pattern of an antenna in 1988. In this work, a ferrite substrate is positioned above a circular microstrip patch and is magnetized using a permanent magnet in order to apply a bias. Using this concept, he predicted a possible beam tilt of around 15°.

Apart from ferrites, ferroelectric materials have also been known for radiation reconfiguration. In 2006 Lovat et al. [62], demonstrated a fixed-frequency scanning antenna, covered with a two-dimensional periodic array of slots in a conducting plate. Beam direction variation in this particular antenna is simply realized by applying an RF signal and tuning the permittivity of the ferroelectric through applying an external bias voltage between the top periodic array and the bottom ground plane. Various other examples for ferroelectric materials, such as a scannable leaky-wave antenna, are available in literature [63, 64].

1.5 Compound reconfiguration

Decoupling of the frequency response from the radiation pattern is a challenging task. In the recent literature, several researchers achieved this ability to independently reconfigure either resonant frequency, radiation pattern, or bandwidth and named it compound reconfiguration [20]. An example is demonstrated by Huff and Bernhard in 2003 [11] for a spiral antenna (Fig. 1.6) which provides broadside radiation operation at two different frequencies or end-fire radiation characteristics at one of these frequencies. The design of these compound devices for a specific application typically requires the use of optimization tools, such as genetic algorithms, and the design and control mechanisms can become more complex in this case.

Pringle et al. [65] demonstrated a compound reconfigurable aperture antenna by changing the switches from open to closed or vice versa. The planar array in this design is optimized using a genetic algorithm. Even though there are a number of papers on compound reconfiguration, much more research is required to achieve practical devices.

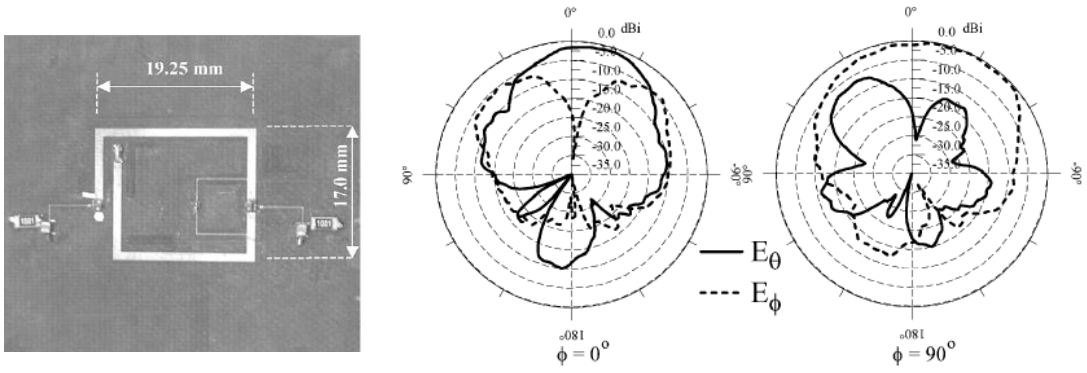

(a) (b)

Figure 1.6. Fabricated antenna with MEMS switches. (a) Fabricated antenna with Radant MEMS switches, (b) Measured broadside configuration radiation pattern for two cut-planes Ø = 0° (left) and Ø = 90° (right). Two Radant MEMS single-pole single throw (SPST) switches are used to reconfigure the radiation patterns of a resonant square spiral microstrip antenna, from [11].

1.6 Conclusion and summary

The main focus of this thesis is on the frequency response reconfiguration/frequency response tuning, due to higher microwave application and fabrication simplicity. As discussed, there is a vast quantity of available literature for designing various components based on MEMS, PIN diodes and optical switches. Several antenna components have been discussed, including such as microstrip antennas, Vee antennas, slot antennas, or dipoles have been discussed. A common drawback of frequency reconfiguration is the discrete switching mechanism, resulting in discrete frequency bands and frequency skipping. Other drawbacks, especially for MEMS switches, are their high manufacturing cost, which have impeded the development of these devices in the past decade. However, since these types of switches demonstrate fast switching with high accuracy, they are still mainly used for military applications and less for commercial purposes.

Other methods discussed in the literature for designing microstrip antennas, slot antennas, monopoles, leaky-wave antennas, FSSs and reflectors are variable reactive loading such as varactors, FET's or piezoelectric actuators. Although these tuning mechanisms show promising results, nevertheless they lack in flexibility. Furthermore due to their high dielectric loss tangent (tan δ) at high microwave frequencies, they are mainly useful for lower microwave frequency designs (< K_a-band).

Several reconfigurable structures based on Ferrites and ferroelectric materials such as microstrip antennas, band pass filters, resonators and phase shifters has also been discussed in the recent literature. Most of the devices discussed in this section are mainly applicable for RF and low microwave frequency (< 5 GHz), since they exhibit high dielectric loss at higher microwave frequencies. Apart from this drawback, BST, the most common ferroelectric material used for frequency tuning, requires a very high voltage of 100-200 V for thick film. Additionally, BST is characterized by a high

permittivity in both thin and thick film forms (ε_r = 100-700), which complicates fabrication and limits applications.

Liquid crystals are a promising alternative for the methods discussed above. Liquid crystals are dielectric materials in liquid form; they can be integrated in flexible electronics, have low dielectric loss tan δ, especially at Ka band and above (< 40 GHz) and require low bias voltage (< 30 V) [66]. Liquid crystal dielectric materials have recently been discussed for microwave and millimetre-wave frequency applications, where they have showed promising results in terms of both tunability and performance especially at higher frequencies, where the performance of other devices such as varactors degrades.

The rest of this thesis will focus on the properties and characteristics of liquid crystals as dielectric materials. It starts with a review of the available literature (Chap. 2) and continues with descriptions of our contribution towards designing a tunable liquid crystal resonator, high S-band tunable resonator, band pass filter and frequency-selective surface structure (Chap. 3-6).

Chapter 2

Physical Properties and Applications of Liquid Crystal

LIQUID CRYSTALS are dielectric materials in the form of a liquid, in which a certain order in the arrangement of the molecules results in anisotropy in the electrical, mechanical, magnetic and optical properties. The physical properties of these materials enable their use as tunable materials that can be exploited in radio-frequency devices such, resonators, antennas, filters and phase shifters. Due to their flexibility as a liquid dielectric and because of their anisotropic characteristics, they have been used widely in telecommunication devices, display technologies, and RF and microwave devices. This chapter provides a comprehensive overview of the properties of liquid crystal material, followed by practical examples of these promising materials for microwave and millimetre-wave technologies.

2.1 Liquid crystal background

2.1.1 The history and discovery

Freidrich Reinitzer (1857-1927) and Otto Lehmann (1855-1922) are known as the two scientists who initially discovered liquid crystals, through experiments on a substance called cholesterol benzoate in 1888 [67]. This discovery was achieved when Austrian scientist F. Reinitzer observed two distinct melting points when experimenting on the cholesteryl benzoate ($C_{34}H_{50}O_2$) also called 5-cholesten-3yl benzoate. The mixture turned to a cloudy liquid (melting point) at a temperature of around 145 °C and as the temperature increased to approximately 179 °C, it became transparent (clearing point), as illustrated in Fig. 2.1.

In March 1889 the discovery was reported to O. Lehmann at the Technical University Karlsruhe in Germany for further investigation. O. Lehmann discovered both liquid and crystal characteristics in this material, hence named it "*Über fliessende krystalle*" in German, translated to "*liquid crystal*" in English [68]. The discovery of liquid crystal remained largely unnoticed in the early 20th century, and as a result the material remained unknown for almost 80 years. Even though in the early 1960s a few universities and research centres, such as Merck in Darmstadt (Germany), were carrying out research on liquid crystals, barely any industries were using these materials for practical applications [69].

The real research and fundamental understanding of these materials started around 1965 to 1969, after the successful creation of liquid crystals at room temperature by a scientist named Hans Keller [69]. Right after this discovery the investigation of liquid crystal applications started, and through these studies liquid crystals became enormously useful in various aspects of telecommunications, lasers, display technologies (e.g. LCD) and even medicine and biology.

2.1.2 Lyotropic and Thermotropic

As discussed, liquid crystal molecules consist of solid/crystalline (long-range orientation order) and liquid/isotropic states [70]. Increasing the temperature from T_1 to T_2 changes their state from solid/crystalline state to a liquid crystal state and then to a liquid/isotropic state, in a reversible process. The temperature T_1 is generally referred to as the melting point and the temperature T_2 as the clearing point (Fig. 2.1) [69].

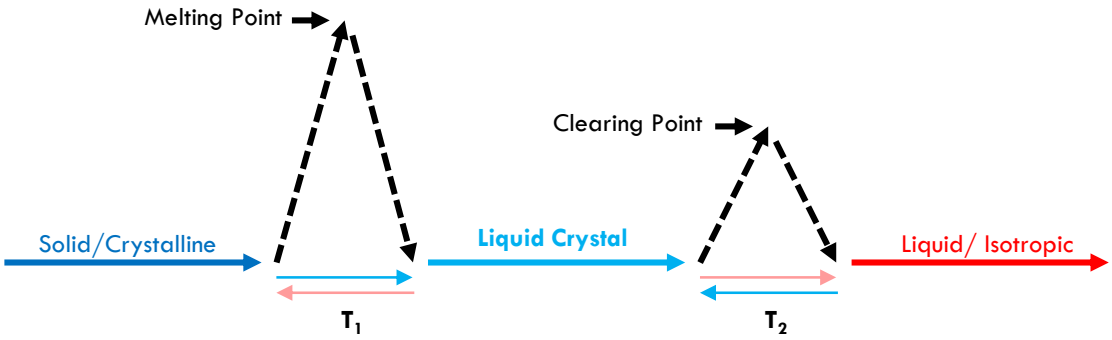

Figure 2.1. Liquid crystal states. In this transition as the temperature is increased, the solid/crystalline material is transformed to liquid crystal phase at temperature T_1 and by raising the temperature to T_2 it is further transformed to liquid/isotropic phase, from [3].

Liquid crystals can be classified as *lyotropic* or *thermotropic* [3]. Lyotropic materials change phase when mixed with a certain type of solvent. Thermotropic materials on the other hand change phase with temperature, but only in a certain temperature range. Thermotropic materials can also be divided as either isotropic, with random molecule arrangement or nematic, with definite molecule order or pattern. Within a certain temperature range, the liquid crystal can transition through several phases, changing from *cholesteric* to *smectic* and finally *nematic* (see Fig. 2.2) [71].

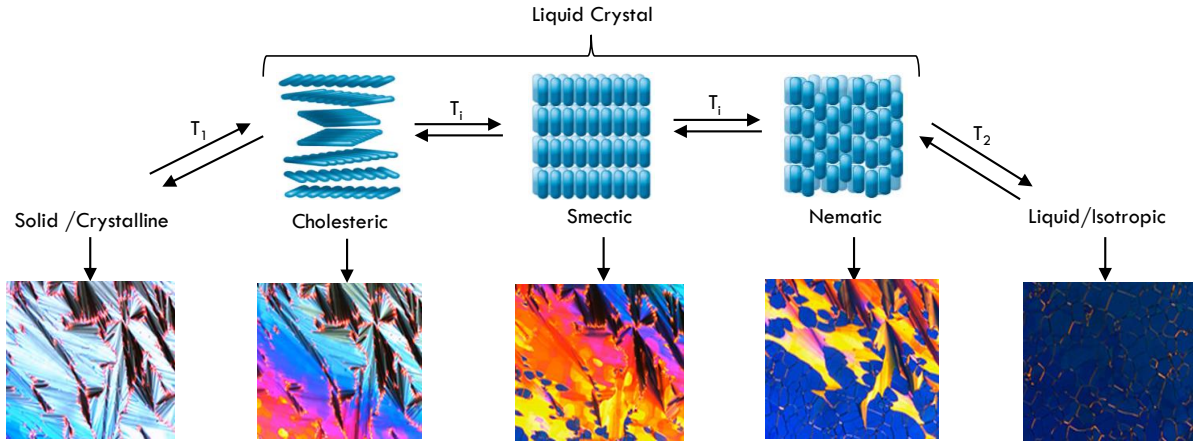

Figure 2.2. Liquid crystal phase. In this image liquid crystal textures is observed using polarized optical microscopy as the molecule undergoes a phase change. The initial phase is the solid/crystalline phase, with molecules being in a rock-hard form and as temperature increases, the molecules enter subsequently cholesteric, smectic, nematic and liquid/isotropic phase change respectively, from [4].

The cholesteric phase, as seen in Fig. 2.2 has a slightly twisted molecule orientation, resulting in a spiral formation, while the smectic phase consists of many variations of the phases in which the molecules in each layer tilt at an angle from the previous layer. Throughout the rest of this thesis, only the nematic phase is considered and its anisotropic properties are used. For this reason, the rest of the discussions will be based on nematic liquid crystal and its electrical material characteristics and properties.

2.2 Liquid crystal-nematic phase

The nematic phase is the most commonly used phase of liquid crystals, especially at microwave and millimetre wave frequencies. The word *"nematic"* comes from a Greek word *"nemato"*, denoting thread-like shape, and is used due to the elongated shape of the liquid crystal molecules (see Fig. 2.2) [72, 73]. In this phase of liquid, through applying an external bias voltage, the electric field in the liquid crystal affects the orientation of the molecules. At low voltages the effect is slight but it increases as the voltage (and the resulting field strength) increases. When the

applied voltage reaches a certain level, all molecules are orientated stably along the direction of the electric field.

2.2.1 Isotropic and anisotropic states

The word *isotropic* in physics is defined as "identical in all directions; invariant with respect to direction" [74, 75]. In a single crystal, the physical and mechanical properties often differ with orientation. When the properties of a material are the same in all directions, the material is said to be isotropic. In full-wave electromagnetic simulation software, isotropic materials are defined by a single constant value (scalar).

However *anisotropic* in physics is defined as "differing according to orientation, as light scattered by a liquid crystal" [74, 75]. The physical characteristics of anisotropic materials are described by anisotropic tensors. For example, for liquid crystal, the anisotropy permittivity tensor exhibits a relative permittivity $\varepsilon_{\parallel}$ in the director direction $\vec{n}$ (the average direction of the molecular axes) and $\varepsilon_{\perp}$ in orthogonal directions [76-78].

In a typical capacitive arrangement, where a liquid crystal cell is sandwiched between two metal electrodes and no bias voltage is applied (V_b = 0 V), the initial alignment of the liquid crystal molecules is achieved through coating the boundary surfaces (preferably the top and bottom layer of the cell) with a thin layer of polyimide film and then mechanically rubbing them using a velvet cloth. The rubbing creates microscopic grooves in the polyimide surfaces (Fig. 2.3) and enables preferred alignment for the liquid crystal molecules in the unbiased state, which leads to higher frequency tuning [66, 79] (Fig. 2.4 (a) and (b)). In electromagnetic simulations, these extremely thin polyimide layers can be neglected to a good approximation.

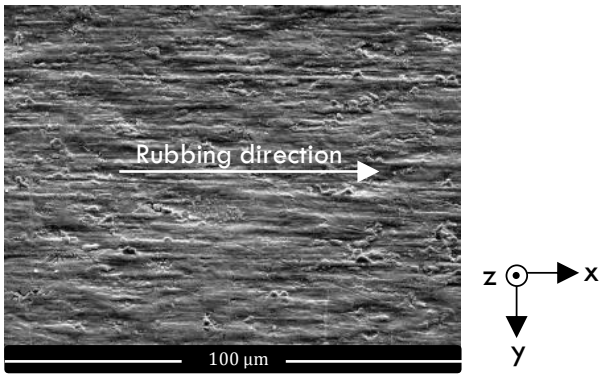

Figure 2.3. Polyimide rubbing direction. Scanning electron microscope (SEM) image of a copper patch coated with a 0.3–0.4 µm thickness of polyimide film and mechanically rubbed along the x-axis.

In this initial case (V_b = 0 V), the director $\vec{n}$ will be parallel to the metallic layers (which are here defined as parallel to the xy plane) and the relative permittivity tensor relevant for the inter-layer material is defined as

$$\overleftrightarrow{\varepsilon_{\perp}} = \begin{pmatrix} \varepsilon_{\parallel} & 0 & 0 \\ 0 & \varepsilon_{\perp} & 0 \\ 0 & 0 & \varepsilon_{\perp} \end{pmatrix}. \tag{2.1}$$

For this case, the scalar effective relative permittivity determining the capacitance can be approximated as $\varepsilon_{eff} = \overleftrightarrow{\varepsilon}_{\perp(z,z)} = \varepsilon_{\perp}$, since the molecules tend to orient along the x-axis while the electric field is predominantly in the z-direction. This is commonly known as the perpendicular state (Fig. 2.4 (b)).

As bias voltage V_b starts to increase from $V_{th} < V_b < V_{max}$, where V_{th} corresponds to the voltage well above the Frederiks threshold [80] along the z-direction and V_{max} corresponds to the maximum applied voltage, the orientation of the director $\vec{n}$ continuously changes from the perpendicular to the parallel state [73]. The random distribution of the liquid crystal molecules in this case can be described by the order parameter S, expressed by

$$S = \langle {}^{3}/_{2} \ \cos^2\theta - {}^{1}/_{2} \rangle \tag{2.2}$$

where in this equation θ is the average angle between the molecular axis and the director $\vec{n}$ (average direction in a volume element of a liquid crystal sample) and < >

corresponds to the mathematical expectation operator, averaging the orientation of all molecules [81, 82].

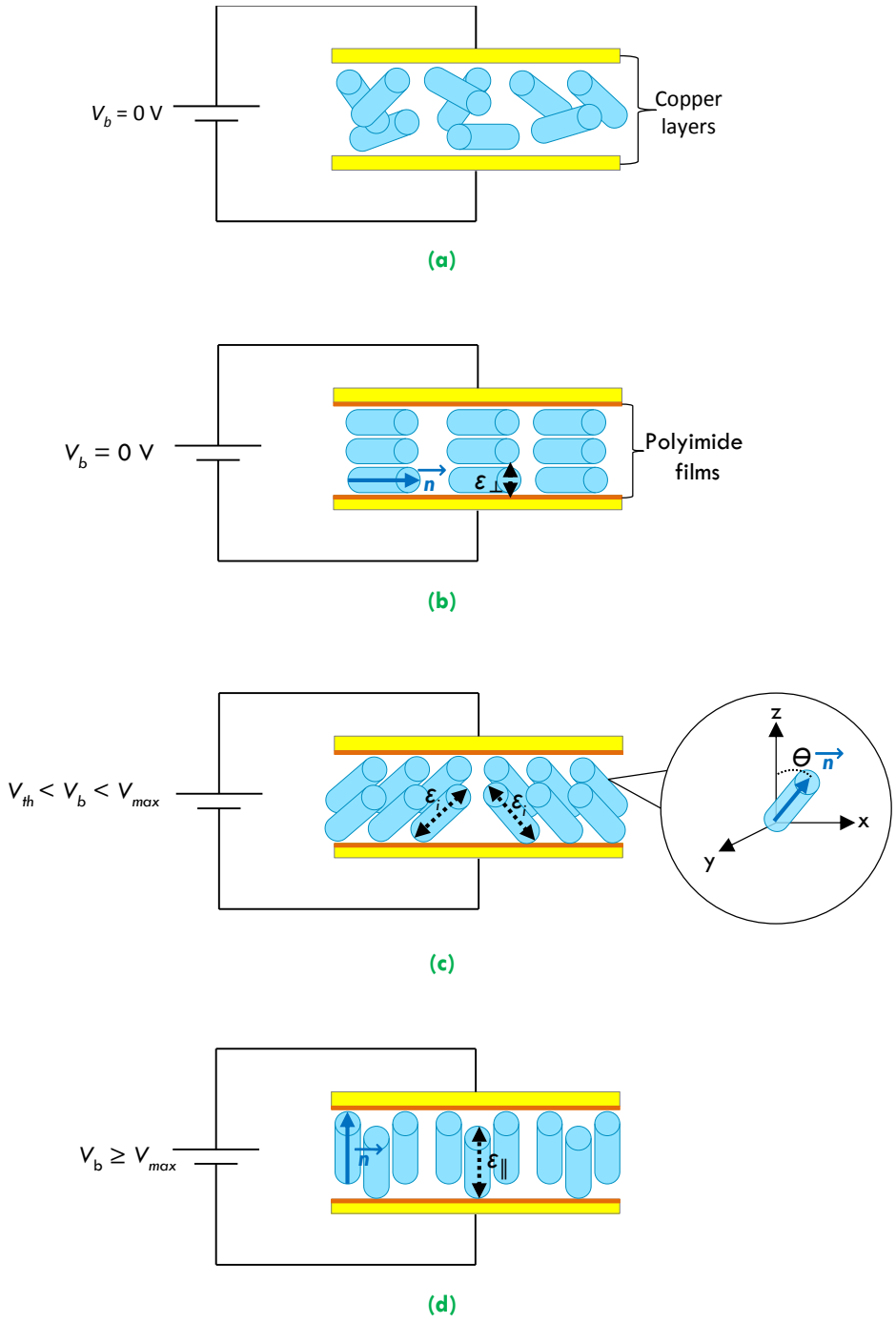

Figure 2.4. Liquid crystal molecule orientation. Liquid crystal molecule orientation in different states (a) no-polyimide films, random orientation, (b) polyimide films, perpendicular state ($\varepsilon_{eff} = \varepsilon_\perp$), (c) intermediate state ($\varepsilon_{eff} = \varepsilon_i$) and (d) parallel state ($\varepsilon_{eff} = \varepsilon_\parallel$).

The difference between the perpendicular and parallel state is identified as the dielectric anisotropy $\Delta\varepsilon$ of the liquid crystal molecules and can be expressed as

$$\Delta\varepsilon = \varepsilon_{\parallel} - \varepsilon_{\perp}. \tag{2.3}$$

By taking into account $\Delta\varepsilon$ and using $\otimes$ as the tensor product of two vectors, the permittivity tensor for the intermediate state can be defined by [73, 83]

$$\overleftrightarrow{\varepsilon} = \varepsilon_{\perp} \cdot \overleftrightarrow{1} + \Delta\varepsilon \cdot (\vec{n} \otimes \vec{n})$$

$$= \varepsilon_{\perp} \cdot \begin{pmatrix} 1 & 0 & 0 \\ 0 & 1 & 0 \\ 0 & 0 & 1 \end{pmatrix} + \Delta\varepsilon \cdot \begin{pmatrix} n_x^2 & n_x n_y & n_x n_z \\ n_x n_y & n_y^2 & n_y n_z \\ n_x n_z & n_y n_z & n_z^2 \end{pmatrix} \tag{2.4}$$

which can be expressed as

$$\overleftrightarrow{\varepsilon_i} = \begin{pmatrix} \varepsilon_{\perp} + \Delta\varepsilon \sin^2\theta & 0 & \Delta\varepsilon \sin\theta \cos\theta \\ 0 & \varepsilon_{\perp} & 0 \\ \Delta\varepsilon \sin\theta \cos\theta & 0 & \varepsilon_{\perp} + \Delta\varepsilon \cos^2\theta \end{pmatrix}. \tag{2.5}$$

For the case when the rubbing direction of the polyimide is along the x-axis (see Fig. 2.3 and Fig. 2.4 (c)), the effective relative permittivity in this case becomes $\varepsilon_{eff} = \overleftrightarrow{\varepsilon_i}_{(z,z)} = \varepsilon_i$, due to E-field along the z-axis.

Further, as the bias voltage reaches up to a maximum voltage ($V_b \geq V_{max}$), the liquid crystal molecules become stable, due to parallel alignment of the liquid crystal molecules. In this state the relative effective permittivity (ε_{eff}) gradually aligns along the director $\vec{n}$, which results in the permittivity tensor becoming

$$\overleftrightarrow{\varepsilon_{\parallel}} = \begin{pmatrix} \varepsilon_{\perp} & 0 & 0 \\ 0 & \varepsilon_{\perp} & 0 \\ 0 & 0 & \varepsilon_{\parallel} \end{pmatrix}. \tag{2.6}$$

This tensor describes a full alignment of the liquid crystal director along the static electric field lines associated to the applied voltage. The effective relative permittivity in this case becomes $\varepsilon_{eff} = \overleftrightarrow{\varepsilon_{\parallel}}_{(z,z)} = \varepsilon_{\parallel}$, given that the liquid crystal

molecules orient along the z-axis and present an effective permittivity along the z-direction. This is generally referred to as the parallel state, i.e. the bias electric field point parallel to $\vec{n}$, Fig. 2.4 (d).

From the description above, it becomes clear that the bias-dependent transition from perpendicular to parallel state provides a continuous variation of the effective permittivity between perpendicular and parallel states.

2.2.2 Tuning range and tunability

The material tuning commonly referred to as frequency tuning/frequency variation/tunability (τ) can be expressed as a function of the highest and lowest resonant frequencies f_h and f_l as

$$\tau = \left(\frac{f_h - f_l}{f_h}\right) \times 100\% \tag{2.7}$$

or

$$\tau = \left(\frac{f_h - f_l}{f_l}\right) \times 100\% \tag{2.8}$$

depending on which frequency is chosen as a reference. Alternatively, the tunable range/tuning range (τR) caused by this variation can also be expressed as [77, 84]

$$\tau R = \left(\frac{2(f_h - f_l)}{f_h + f_l}\right) \times 100\%. \tag{2.9}$$

The material quality factor η can also be defined by the relation between tunability and the maximum dielectric losses ($\tan \delta$), according to

$$\eta = \frac{\tau}{\max(\tan \delta)}, \tag{2.10}$$

or

$$\eta = \frac{\tau R}{\max(\tan \delta)}, \tag{2.11}$$

which will differ depending on whether the material is used in perpendicular (tan $\delta_{\perp}$) or parallel (tan $\delta_{\parallel}$) configuration.

Fig. 2.5 schematically illustrates the evolution of the relative permittivity and the equivalent loss tangent between the two extreme states (perpendicular and parallel) when the bias voltage is increased from V_{th} until V_{max} as a function of the applied bias voltage.

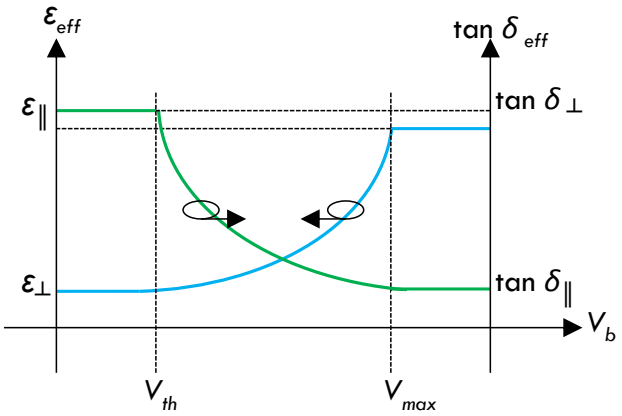

Figure 2.5. Effective relative permittivity and loss tangent as function of the applied bias voltage. Effective relative permittivity behaviour between perpendicular ($\varepsilon_{\perp}$) and parallel ($\varepsilon_{\parallel}$) states and loss tangent (tan $\delta_{\perp}$ and tan $\delta_{\parallel}$) as function of the applied bias voltage (V_b).

For available liquid crystal mixtures, the typical relative permittivity value for the perpendicular ($\varepsilon_{\perp}$) state is around 2.2 to 2.8, while for the parallel ($\varepsilon_{\parallel}$) state is between 2.6 and 3.5. The resulting insertion loss in practical devices depends on the topology, material and operational frequency [51, 76]. Table 2.1 illustrates the properties of some of the most common liquid crystal (nematic) samples used at microwave and millimetre-wave frequencies. The listed values might slightly vary, depending on the working frequency and temperature.

Table 2.1. Properties of some of the most common liquid crystal (nematic) samples. Properties of liquid crystals at 20 °C temperature, as specified at the given operating frequency.

Samples	Permittivity		Dielectric anisotropy	Loss tangent		Operating frequency
	$\varepsilon_{\perp}$	$\varepsilon_{\parallel}$	$\Delta\varepsilon$	tan $\delta_{\perp}$	tan $\delta_{\parallel}$	f (GHz)
K15 (5CB)	2.72	2.90	0.18	0.03	0.03	1-10
BL037	2.35	2.61	0.26	0.06	0.06	1-10
BL006	2.62-2.69	3.11-3.12	0.49-0.43	0.0015-0.007	0.0035-0.0036	4.8-8.7
E7	2.72	3.17	0.45	0.12	0.02	5-6

2.2.3 Switching time

The switching time / tuning speed of liquid crystal in general depends on several factors, including the liquid crystal layer thickness, viscosity of the liquid crystal type, temperature and the surface treatment (e.g. polyimide type). Various equations and theories for calculating the switching time have been discussed. Oseen and Frank were the two first scientists who formulated the fundamentals of the elasticity theory of liquid crystals back in 1920's, and thus it is now known as Oseen-Frank theory, defining the balance between elastic and electric torque exerted by the applied field [85].

The dynamical response and the viscous torque was later described by Erickson and Leslie, known as response time/free relaxation time (t_0), expressed by

$$t_0 = \frac{\gamma_1 d^2}{K_{11}\pi^2} \tag{2.12}$$

which can be applied to parallel, perpendicular and even twisted alignment. In this equation, γ_1 is the rotation viscosity of the liquid crystal, d is the cavity thickness and K_{11} represents the torque. According to this equation the response times are proportional to the cavity thickness squared, meaning that they can be improved by reducing the liquid crystal cell thickness. For liquid crystal technology at microwave frequency these thicknesses are around $5 \leq d \leq 500$ µm [66]. The above equation can be further refined by considering the rise and decay time, depending on the applied bias voltage [85] to t_{rise} and t_{decay}, defined as

$$t_{rise} = \frac{t_0}{\left|\frac{V}{V_{th}} - 1\right|} \tag{2.13}$$

and

$$t_{decay} = \frac{t_0}{\left|\frac{V_{rem}}{V_{th}} - 1\right|} \tag{2.14}$$

where in this equation V_{rem} is the remaining voltage after the bias voltage is removed, also known as the final state of the relaxation. The absolute value in denominator illustrates that this equation is valid for both $V_{rem} > V_{th}$ and $V_{rem} < V_{th}$. From Eqns. (2.13) and (2.14), it can be stated that the higher the voltage step while switching, the faster the tuning process will be, while the same holds true for the switching off, i.e. the lower V_{rem} the faster the response time will be.

2.3 Liquid crystal microwave devices

One of the early attempts at using liquid crystals in RF applications was reported by Truesdale [86] in 1972, who used a liquid crystal sensor to measure the near-field radiation pattern. In 1978, Anders demonstrated the initial investigation of the rectangular microstrip patch element using liquid crystal [87], but the work which illustrated application of liquid crystals in the microwave range was by Bui-Hai and Martinez [5] in 1983 (Fig. 2.6).

Owing to the anisotropic properties of liquid crystal and compound mixtures, there are many reported devices which use liquid crystal to achieve electrical tuning. In the next section liquid crystal tunable devices designed for operation at microwave and millimetre-wave frequencies are discussed. The description of these devices is divided into four main categories: 2.3.1-*resonators and filters*, 2.3.2-*phase shifters and delay lines*, 2.3.3-*antennas* and 2.3.4-*frequency-selective surfaces and metamaterials*.

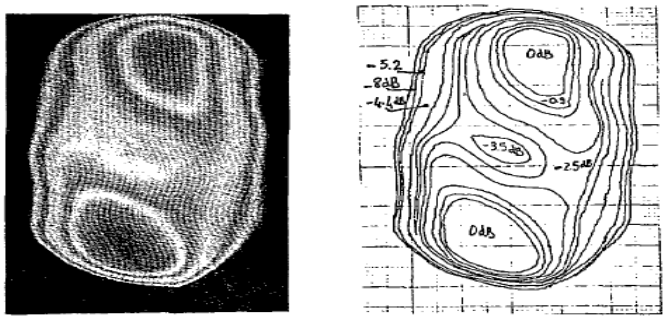

Figure 2.6. Electromagnetic energy distribution. Using liquid crystal at microwave frequency of 7 GHz for visualization of electromagnetic radiation pattern, from [5].

2.3.1 Resonators and filters

Tunable resonators and filters which exploit the dielectric anisotropy of liquid crystal have been discussed in the literature. One of the examples of liquid crystal resonators was reported in [88]. The study illustrated a half-wavelength open-circuited stub resonator and a second-order dual behaviour resonator filter. Using two standard liquid crystal samples (K15 and BL037 [88-91]), frequency shifts of a few percent for lower microwave frequencies (below X-band) were achieved.

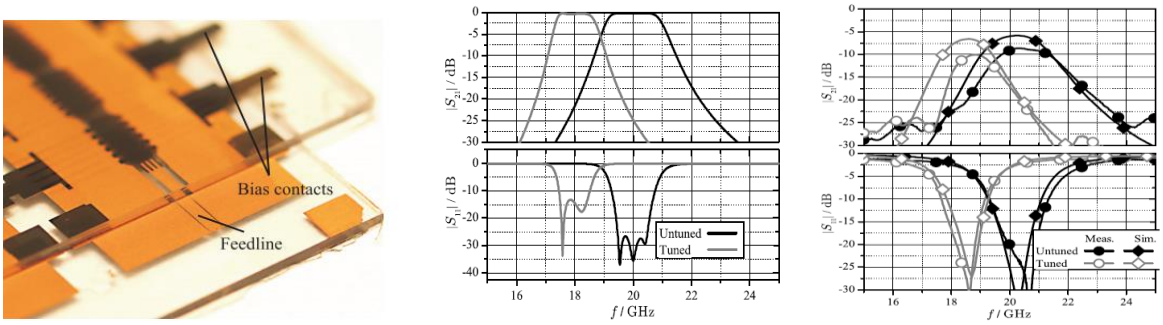

(a) (b) (c)

Figure 2.7. Tunable band-pass filter. (a) Top view of the fabricated tunable filter with operating frequency of 20 GHz, (b) simulation results, with all elements assumed as lossless and (c) measurements results together with a full-wave simulation. The device is fabricated using a glass-liquid crystal-glass sandwiched structure with a total thickness of 600 μm and lateral dimensions of 9× 4 mm, [15].

In a different example, a liquid crystal tunable band-pass filter was presented [15] (Fig. 2.7). The proposed three-pole filter operating at a centre frequency of around 20 GHz demonstrated approximately 2 GHz of frequency shifting corresponding to a tuning range of around 10.25%.

A comparable tunable coupled microstrip line filter has been developed with an operational frequency of 33 GHz [2]. The E7 liquid crystal sample employed in this structure demonstrated tunability of up to 2 GHz (Fig. 2.8).

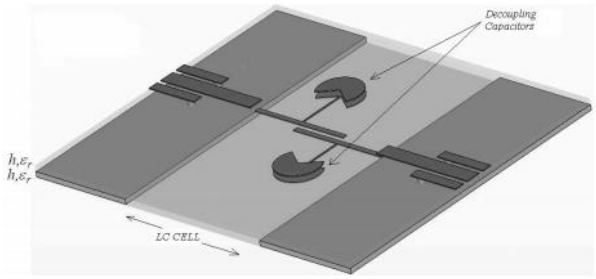

Figure 2.8. Parallel-coupled line tunable resonators. A tunable 33 GHz parallel-coupled microstrip filter based on nematic liquid crystals, with tunability range of 2 GHz. The insertion loss in this filter was around 4.5 dB, which is mainly due to the microstrip line to CPW transitions used for measurement of the filter by a probe-station [2].

2.3.2 Phase shifters and delay lines

Apart from resonators and filters, liquid crystals have been demonstrated in the design of phase shifters and delay lines. An early example of phase shifters is reported in [92], where a voltage-controlled 20^0 phase shift was achieved with a K15 sample at a centre frequency of 10.5 GHz. Furthermore in [93], a planar integrated tunable phase shifter has been presented. By filling the channels with liquid crystal and applying a bias voltage, a differential phase shift of 53° was achieved around a centre frequency of 18 GHz.

In a different example, reducing the liquid crystal cell thickness was discussed for improving the tuning/switching speed [10]. In this work instead of the common 500 µm thickness of liquid crystal only 5 µm was used. This results in lower amount of liquid crystal molecules, lower time for molecule orientation and hence faster switching speed between the parallel and perpendicular state. In this tunable phase shifter a 60^0/dB of phase shift was achieved with tuning speed of 340 ms (Fig. 2.9).

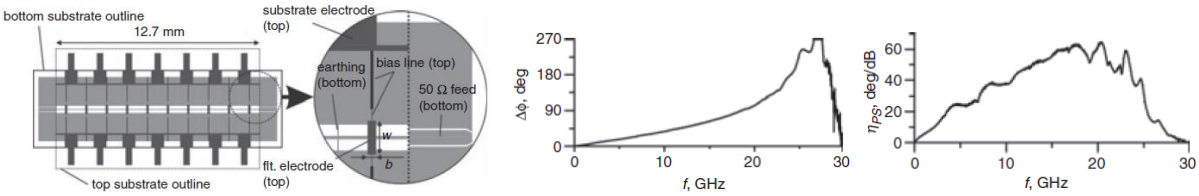

(a) (b) (c)

Figure 2.9. Tunable phase shifter. (a) Top view of the realized phase shifter filled with liquid crystal, (b) differential phase shift and (c) phase shift effectiveness, confirming 60°/dB phase shift at 20 GHz in the fabricated measurement [10].

A microwave variable delay line using a membrane impregnated with liquid crystal has also been fabricated [94]. Experimental results indicated a 270° phase shift for the variable delay lines with a tuning response time of around 33 ms. In a more recent case, a 2-D electronically-steered phased array with a variable delay line was presented [12]. The 17.5 GHz phased array demonstrated a maximum differential phase shift of 300° (Fig. 2.10).

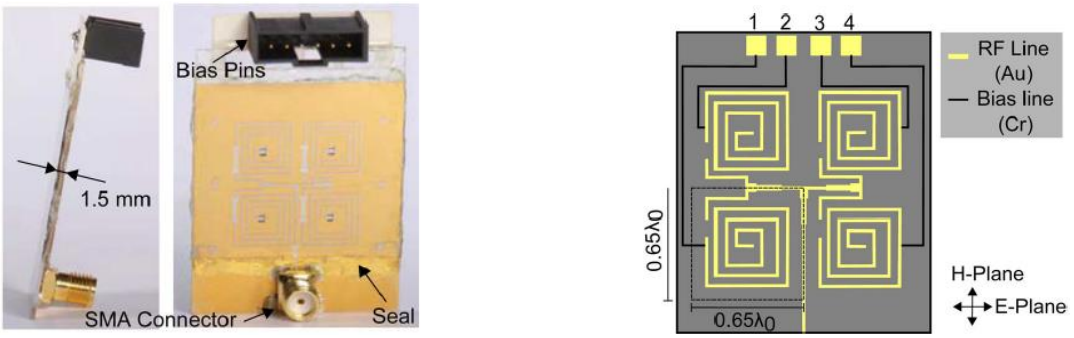

(a) (b)

Figure 2.10. 2-D electronically steered phased-array antenna. (a) side and back view photographs of the fabricated prototype 2 × 2 antenna array and (b) antenna layout with the components (RF feeding network, variable delay lines, biasing network, four biasing pads) mounted on the back dielectric layer [12].

2.3.3 Antennas

Electrically tuned liquid crystal antennas have been widely discussed in recent years. The key to these designs is to form a sandwich shape structure, with a metal patch on top and a ground plane on the bottom of the structure and liquid crystal in between in a central cell. The patterned patch and ground planes are used both for

radiation and as electrodes in the biasing circuit. Liquid crystal antennas can be divided into three main categories: 1- *frequency tunable antennas*, 2- *beam steering antennas and reflectarrays* and 3- *polarization agile antennas*. In the following, each of these categories are discussed separately.

2.3.3.1 Frequency tunable antennas

One of the initially reported tunable antennas had liquid crystal placed inside its intermediate foam substrate, underneath the patch [95]. Upon application of a varying external bias voltage to this structure, a frequency shift of 140 MHz was obtained from 4.74 and 4.6 GHz, which corresponds to 2.95% tuning range.

A comparable rectangular patch demonstrated 5.5% tunability with respect to the lower frequency [96], in a similar frequency range (~ 4.5 GHz). For these two antennas, standard commercial K15 and BL037 liquid crystal samples were used. Similarly a sandwich structure antenna operating at a frequency of 5 GHz was presented in [7]. This antenna was designed using three layers of Taconic glass-reinforced PTFE substrate placed on top of each other, with E7 liquid crystal in its central layer. The simulation of this arrangement predicted a tuning range of 8%, whereas measurement demonstrated a tuning range of 4% (Fig. 2.11).

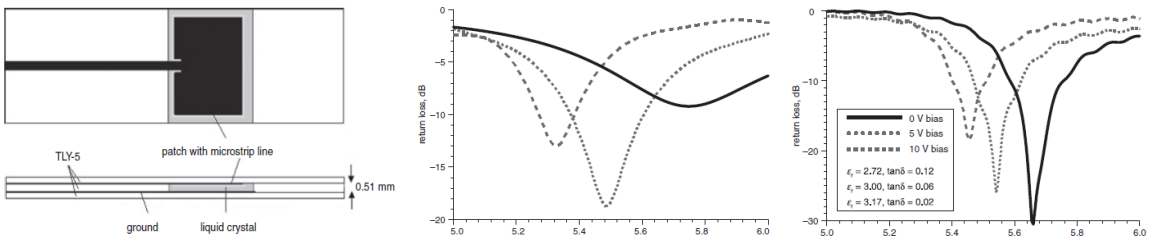

Figure 2.11. Tunable microstrip patch antenna. (a) Liquid crystal based microstrip patch antenna geometry, with three layers of Taconic TLY-5 substrate each 0.51 mm thick, 20 × 15 mm patch, (b) simulated results and (c) fabricated measurements [7].

Liquid crystal has in addition been demonstrated in combination with newly developed flexible materials. An example of a tunable multilayer patch antenna on flexible liquid crystal polymer (LCP) substrates is reported in [14] (Fig. 2.12). This work shows that through using high-performance novel liquid crystal mixtures, a continuous frequency tuning range of 10% at Ka band (~ 35 GHz) was achieved through application of an external bias voltage.

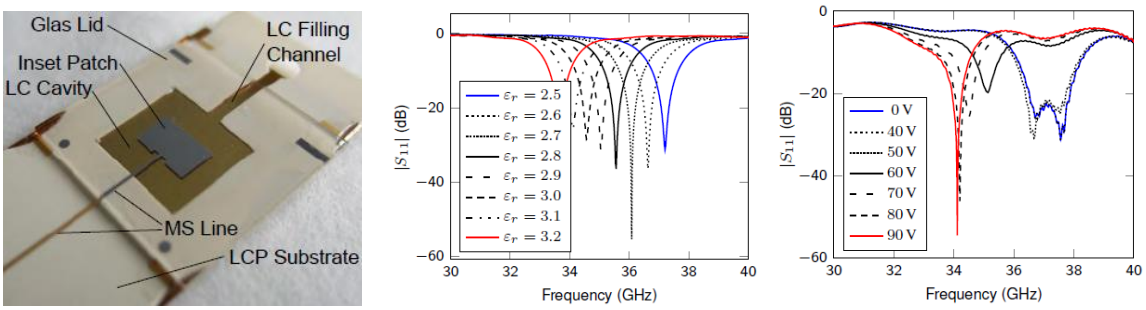

Figure 2.12. Tunable patch antenna. Prototype designed frequency tunable patch antenna operating at Q-band is presented. Through using liquid crystal between the microstrip layers, 10% of continuous frequency tuning is achieved [14].

2.3.3.2 Beam steering antennas and reflectarrays

The use of liquid crystal has been reported for the development of leaky-wave antennas able to steer their main beam direction at a fixed frequency. In [16] a leaky-wave antenna based on composite right/left-handed waveguide was described, with beam steering at 7.6 GHz (Fig. 2.13). Through application of either a static electric or magnetic field to the liquid crystal molecules, a beam tilt of around ±10° was achieved.

Figure 2.13. Leaky-wave tunable antenna. Fabricated liquid crystal tunable leaky wave antenna based on a composite right/left-handed waveguide structure, with beam steering capability. The maximum measured obtained beam tilt is ±10° degree around broadside [16].

Apart from phased arrays, reconfigurable reflectarrays could benefit greatly from the application of liquid crystals in their tuning mechanism. One of the first reflectarrays with liquid crystal tuning is reported in [97, 98]. In this design, a 35 GHz liquid crystal tunable reflectarray was presented and verified. Measurements demonstrated 300° of phase tunability of a unit cell, through applying bias voltages up to 40 V. A comparable example was reported in [89]. In this work numerical and measured results demonstrated 180° of tunable phase shift at X-band using K15 liquid crystal.

In the similar frequency range, a reflectarray antenna was presented using a BL006 sample [99], [100]. The electronic tuning of the effective permittivity of the liquid crystal in this study [100], demonstrated reconfiguration of monopulse sum and difference patterns. A similar concept was also used in [8] (Fig. 2.14), [97], and [101], where liquid crystal was used at X-band, Q-band and W-band to achieve tunability in a reflectarray.

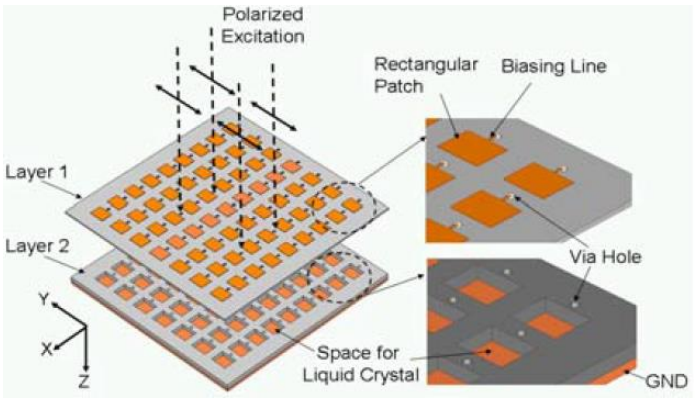

Figure 2.14. Geometry of periodic cell. Reflectarray elements in the range of 9-11 GHz is designed using commercial available liquid crystal, enabling phase shift at X-band frequency [8].

Liquid crystals have been demonstrated as well for reflectarrays at higher microwave frequencies, even above X-band. Due to the decreasing liquid crystal loss tangent δ with increasing frequencies, more attention has been directed in recent years towards designing millimetre-wave reflectarray cells. A recent reflectarray designed for operational frequencies of 77 GHz suggests the possibility of 280° element phase tunability through application of an external bias voltage [101].

Moreover in [102] a tuning phase range of 360° was achieved for a reflectarray operating in a frequency range of 30 to 40 GHz.

In a recent study a millimetre-wave reflectarray (F-band), which consists of 52 × 54 identical cells, has been designed to operate in the frequency range from 96 to 104 GHz [103]. A liquid crystal mixture was used to demonstrate the potential of the proposed reflectarray for beam scanning in F-band. This suggests that future wideband tunable antennas in the frequency range above 60 GHz are possible. In similar concepts proposed in [104], phase changes of 165° and 130° were achieved for reflectarrays operating at a centre frequency of 102 and 130 GHz respectively.

2.3.3.3 Polarization agile antennas

Polarization agile antennas using liquid crystal mixtures were reported in [1, 105] (Fig. 2.15). This 2D beam steering phase array antenna consisted of a 2 by 2 dual-fed microstrip patch array and two separate feeding networks. Through reconfiguration of the feeding networks, dual linear and dual circular polarizations were achieved. Continuous tuning of the antenna polarization at a frequency of 13.75 GHz was illustrated for both simulation and prototype measurements.

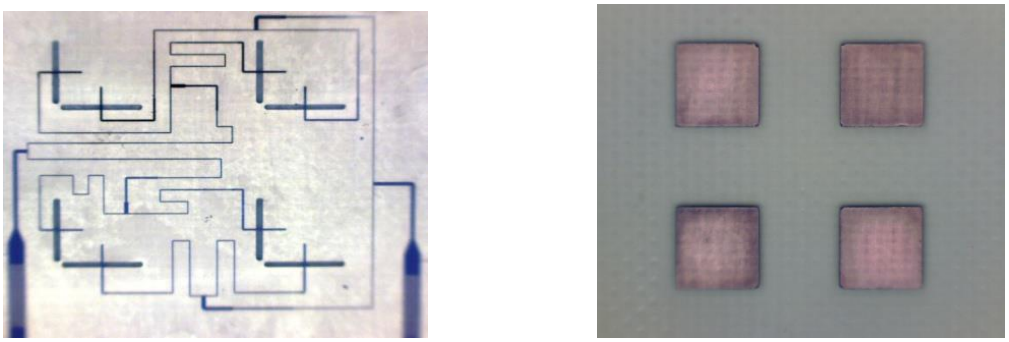

(a) (b)

Figure 2.15. Polarization agile antenna. (a) and (b) Image of the fabricated polarization agile antenna filled with liquid crystal mixture [1].

2.3.4 Frequency-selective surfaces and metamaterials

Other areas which have as well demonstrated high potential for tuning with liquid crystal materials are frequency-selective surfaces and planar metamaterials. In these structures, the liquid crystal is generally sandwiched between two identical parallel substrates, consisting of printed patch patterns. Through application of an external bias voltage, a shift in the resonant frequency can be achieved. An FSS with operational frequency at D-band (110-170 GHz) has been presented in [106]. The BL037 liquid crystal mixture in this device was sandwiched between two arrays of slot elements, illustrating 3% tunability. In another experimentally validated example, a magnetically tunable negative permeability metamaterial consisting of an array of broadside coupled split ring resonators infiltrated with liquid crystals has been proposed. Here a resonant frequency shift of 0.3 GHz was obtained at X-band [107].

In other reported examples, perpendicular and parallel alignment of nematic liquid crystal cells have been demonstrated for developing metamaterial structures with the index of refraction tunable from negative, through zero, to positive values [108-110]. Although some of the reported FSS and metamaterial structures operate at higher frequencies (e.g. terahertz), the development of new liquid crystal mixtures suggests future potential applications at microwave and millimetre-wave frequencies.

2.4 Conclusion and summary

In this chapter the background and the history behind the discovery of cholesterol benzoate, the first discovered liquid crystal were explained, followed by consideration of its fundamental properties. This section also has reviewed the temperature effect on the liquid crystal molecules and investigated its solid/crystalline to liquid/isotropic phase change. Moreover the physical properties

of the main phase of the liquid crystal, known as the nematic phase owing to its thread-like molecules, have been explained and investigated in more depth.

Various well-known terms and definitions which are used throughout this thesis have been defined and explained, such as: director, dielectric anisotropy, permittivity tensor and tunability. In addition this chapter summarizes available literature on various devices using liquid crystals and operating at microwave frequencies, such as resonators, filters, phase shifters, delay lines, antennas, frequency-selective surfaces and metamaterials.

This chapter has provided background information on liquid crystals in their nematic phase and highlighted their promising properties for designing and implementing high performance microwave devices mostly owing to their low bias-voltage requirement, continuous tuning and possible integration with printed technologies. These features along with other advantages of liquid crystals such as flexibility and transparency will be used in the following chapters to design a frequency-tunable microwave device with liquid crystal acting as tunable dielectric substrate in a central layer.

Chapter 3

Tunable Liquid Crystal S-band Resonator

DURING the past decade, various tunable liquid crystal devices have been designed and investigated operating at high microwave or millimetre wave frequencies (above C-band), but less attention has been given to the lower GHz frequency range, where most current microwave devices operate. In this chapter a review of current tunable microwave devices operating at L, S and C-band are carried out, followed by a discussion of a novel tunable liquid crystal S-band resonator design. In this work, the resonator is designed using analytical electromagnetic theory, and investigated and proven through full-wave electromagnetic simulations using commercial software tools. The final optimized model is then fabricated using standard methods. The compared results from both the full-wave electromagnetic simulation and the prototype measurements demonstrate close agreement and thus validate the concept.

3.1 Introduction

A number of tunable devices have been designed using nematic liquid crystal, with most of the available literature focused on high microwave and millimetre wave frequencies, due to the lower insertion loss of liquid crystals at these frequencies. However since most commonly industrial, scientific and medical (ISM) communications devices such as wireless sensor networks, and wireless LANs operate at 2.5-5.8 GHz, much more attention is required for designing lower frequency (C-band ≤) liquid crystal tunable microwave devices [111].

A number of low microwave frequency (1-8 GHz) liquid crystal devices have been reported in the past. One of the first examples is by Martin et al. [95] in 2003, where a 5 GHz patch antenna has been designed based on theoretical dependence of the resonant frequency on the substrate properties for the conventional TM_{100} cavity mode. Using liquid crystal as the dielectric material, 2.56% and 2.95% of tunability was obtained for measurement and simulation respectively. This antenna was later optimized and the tunability was improved to 5.5%, using two other different liquid crystal samples [96].

Other examples have been reported for a circular patch antenna [112], illustrating a simulation tunability of 5.4%, but no fabrication or measurements were reported. In [7] a microstrip patch antenna operating in the 5 GHz range and tuned by liquid crystal was described. The simulated frequency tuning in this case was around 8%, while the measurements showed a tuning of only 4%. Liu in 2009 [113], demonstrated the first patch antenna tunable with liquid crystal with an operating frequency of 2 GHz. Through applying external bias voltage, 8% and 3.8% frequency variation were achieved for simulation and measurement respectively. A summary of the above discussed results is shown in Table 3.1.

The object of this chapter is to initially explore the nematic phase of liquid crystal, identify its potential applications at microwave frequencies, followed by designing and modelling a tunable resonator with operational frequency of around S-band (3.5

GHz), using theoretical calculation and full-wave electromagnetic simulation. Finally to prove the concept, this resonator is fabricated and the measured results are compared with the simulation.

Table 3.1. Tunable liquid crystal microwave (≤ C-band) devices. This table provides a summary of the current designed microwave elements in the literature with an operational frequency of 1 to 8 GHz (L-band to C-band).

Operating frequency (GHz)	Tuning (τ)		Liquid crystal sample	Ref
	Simulation	Measurement		
5	2.56%	2.95%	K15	[95]
5	NA	2.95%	K15	[96]
5	NA	5.5%	BL037	[96]
2	5.4%	NA	NA	[112]
5	8%	4%	E7	[7]
2	8%	3.8%	E7	[113]

3.2 Theoretical calculation

3.2.1 Primary design

Initially various microwave antenna structure were considered for this design, however from the obtainable options, microstrip patches were selected as the ideal alternative, owing to their [114]:

- Light weight and low volume
- Thin profile planar configuration
- Low fabrication cost and as a result suitability for mass production
- Linear and circular polarization possibility with simple feeding
- Dual-frequency and dual-polarization
- Easy integration with microwave integrated circuits

as well as their extensive microwave applications, especially for military and space applications and the rapidly growing demand for hand held wireless devices.

A microstrip patch consists of a resonant patch on one side of the dielectric and a ground plane on the other side. Two transmission lines connected on both sides of the microstrip patch form a stepped impedance filter, Fig. 3.1.

The patch is generally made of conducting material such as copper or gold and can take any shape, but is generally designed in the form of a square, rectangle, circle, circular ring, triangle, dipole, or ellipse. Apart from the advantages, some of the drawbacks of microstrip patches are their narrow bandwidth and low power handling capacity (~100 W).

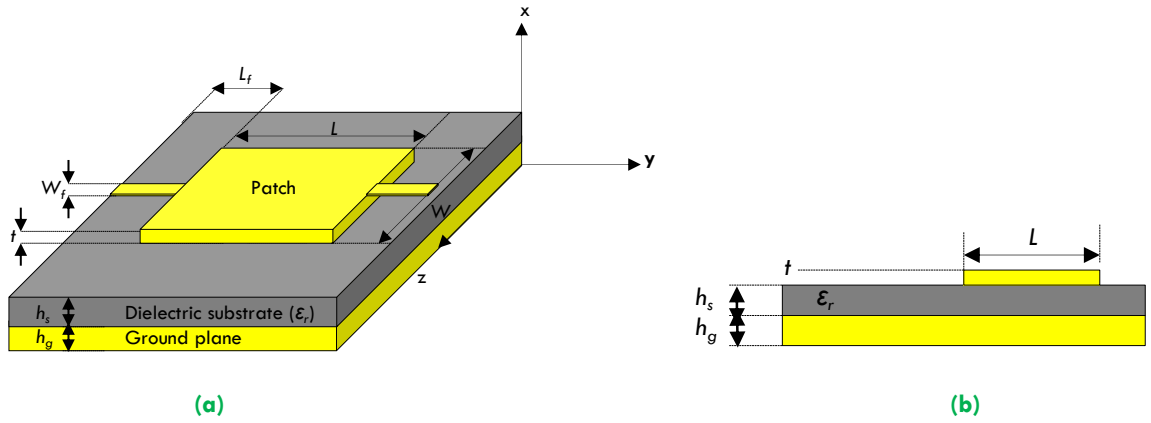

Figure 3.1. Structure of a stepped impedance filter. (a) top view - consists of a resonant patch connected to two feeding lines on the top, a dielectric substrate (ε_r) with height h_s in the centre and a metal ground plane with height h_g on the bottom, (b) side view.

3.2.2 Resonant patch and feeding

Given that the main objective was to design a resonant patch, with operational frequency of around S-band (2-4 GHz), the first step required defining the patch dimensions, selecting the appropriate material and accurate thickness. For the microstrip patch to resonate, the dimension L (universally taken to signify the longer dimension) is required to be a half-wavelength. According to microstrip patch formulas [115], for a thin patch with dense material, the first resonance can be calculated by

$$f_r = \frac{C_o}{2L\sqrt{\varepsilon_r}}. \qquad (3.1)$$

where ε_r corresponds to the relative permittivity of the substrate and $c_o \approx 3\times10^8$ m/s. For designing microstrip resonant patches at microwave frequencies, a typical range of $2.2 \leq \varepsilon_r \leq 12$ is generally used for the substrate [114]. For this design, given that the relative permittivity of liquid crystals is typically between 2.2 and 3.5, a substrate with relative permittivity of $\varepsilon_r = 2.2$ was chosen.

The next part of the theoretical design involves identifying available feeding techniques and calculating the dimension of the feed lines for given an impedance of 50 Ω. There are several feeding configurations that can be used, but the four most popular techniques are: coaxial probe, aperture coupling, proximity coupling and microstrip line [114]. For this design given that liquid crystal was placed in the central layer a microstrip line feeding technique was applied. Microstrip feed lines are conducting strips which are easy to model, match and fabricate. According to [116], the dimensions of a microstrip feed line was estimated to be around 28 by 1.3 mm^2 ($L_f \times W_f$). Given that for this design, calculation and measurement of both the reflection and transmission were required, a duplicated feed line was placed on the right-hand side of the patch (Fig. 3.1 (a)).

3.3 Simulation: optimization and parametric analysis

3.3.1 Multi-layer structure

Before describing the simulation of the final structure, this section describes each of the main layers of the resonator independently, with each layer having its own physical dimension and material characteristics (Fig. 3.2).

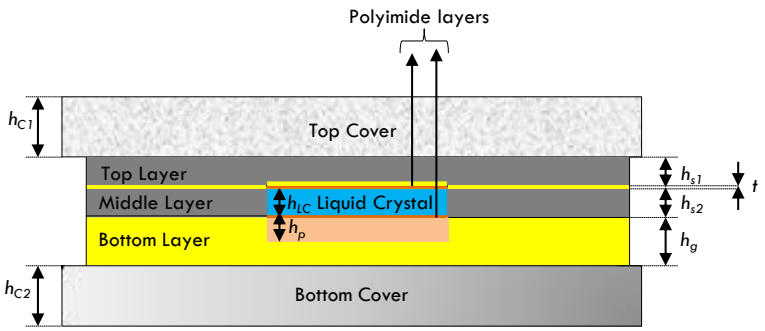

Figure 3.2. Multi-layer resonator cross section. Tunable S-band liquid crystal resonator is illustrated with top, middle and bottom layer.

The top layer was simulated using an RT/Duroid 5880 substrate (ε_{s1} = 2.2 and tan δ_{s1} = 0.0009) and a perfect electric conductor (PEC) for the patch and the feed lines. This layer consisted of a 28 × 28 mm ($L \times W$) resonant copper patch and two microstrips feed lines. The substrate had an overall dimension of 84 × 50 mm and a thickness (h_{s1}) of 0.50 mm.

The second layer was defined as the middle layer. This layer also had a physical dimension of 84 × 50 × 0.50 mm and was also simulated as RT/Duroid 5880 (ε_{s2} = 2.2 and tan δ_{s2} = 0.0009). In order to introduce the liquid crystal, a 28 by 28 mm square hole with height of 0.5 mm ($h_{s2} = h_{LC}$) was cut through the middle layer, creating a cavity for the liquid.

The final layer was called the bottom layer, with a dimension of 84 × 50 mm² and a height of h_g = 3 mm. Since in the fabrication process for the alignment of the liquid crystal molecule, a thin layer of polyimide coating is required (discussed in Sec. 2.2.1), a 28 by 28 mm square with a depth of 0.5 mm is cut out from the copper plate, forming a hollow space. This cavity is then filled with a square block of TMM3 dielectric substrate (ε_p = 3.27 and tan δ_p = 0.002), with a dimension of 28 × 28 mm², height of h_p = 0.5 mm and copper coating on the bottom side. The choice of TMM3 was based on its high surface resistivity (> 9 × 10^9) and thermal coefficient (+37), which was necessary for polyimide baking process (see Sec. 4.3.1.2).

Apart from the discussed layers, the final designed structure was then placed within sealed covers to avoid any liquid leakage during the measurement process. For this purpose, two separate covers were used in the full-wave electromagnetic simulation. A Teflon top cover, with relative permittivity of 2.0 and loss tangent tan δ_{c1} of 0.0002 and a Plexiglass bottom cover with relative permittivity of 3.6. In this simulation the top and the bottom layer had dimensions of 95 × 80 mm and a thickness of h_{c1} = 6 mm and h_{c2} = 6 mm respectively.

The next stage involved using the above estimated values to design the 3D full-wave electromagnetic simulation model. For this purpose Computer Simulation Technology (CST) Microwave Studio [117] was used as a simulation tool, due its thin sheet technique and sub-gridding scheme, resulting in a high simulation efficiency. Given that this software benefits from a transient solver, it provides higher and accurate numerical calculation compared with other electromagnetic full-wave simulation software. Before finalizing the design and simulating the final structure, parametric analysis and accurate electromagnetic modelling of the liquid crystal resonator are discussed.

3.3.2 Isotropic and anisotropic analysis

Given that liquid crystals are anisotropic materials, a comparison was carried out between simulating the liquid crystal as isotropic or anisotropic material.

For isotropic material, both the perpendicular and parallel states in the full-wave electromagnetic simulation are modelled with a scalar value, namely $\varepsilon_{\perp}$ = 2.72 and $\varepsilon_{\parallel}$ = 2.90 respectively, corresponding to the perpendicular and parallel states of the K15 liquid crystal sample (Table. 2.1).

However for the anisotropic material simulation the permittivity tensor values are defined according to Eq. 2.1 and Eq. 2.6 (discussed in Chap. 2). Subsequently for the same liquid crystal values as above, the anisotropic relative permittivity tensors are defined by

$$\overleftrightarrow{\varepsilon_{\perp}} = \begin{pmatrix} 2.90 & 0 & 0 \\ 0 & 2.72 & 0 \\ 0 & 0 & 2.72 \end{pmatrix} \tag{3.2}$$

and

$$\overleftrightarrow{\varepsilon_{\parallel}} = \begin{pmatrix} 2.72 & 0 & 0 \\ 0 & 2.72 & 0 \\ 0 & 0 & 2.90 \end{pmatrix} \tag{3.3}$$

corresponding to the perpendicular and parallel states of the K15 liquid crystal sample. Ultimately in order to compare the simulation result of both isotropic and anisotropic material characteristics, a comparison is made using the designed S-band resonator over a frequency range of 2.0-4.5 GHz (Fig. 3.3).

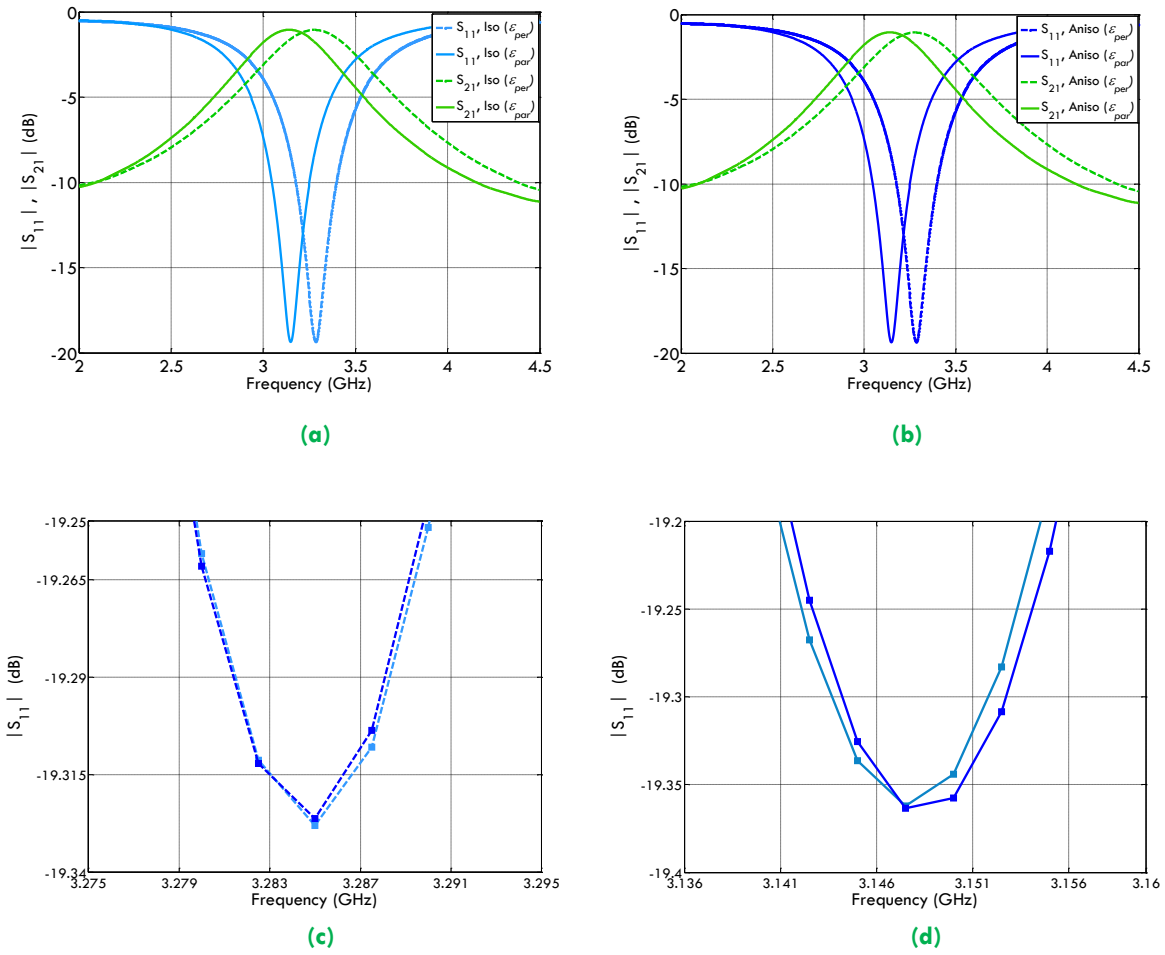

Figure 3.3. Isotropic and anisotropic liquid crystal. (a) Simulated as isotropic material, (b) simulated as anisotropic material, (c) perpendicular state for both isotropic (light blue) and anisotropic (dark blue) states and (d) parallel state for both isotropic (light blue) and anisotropic (dark blue) states.

In the isotropic case the resonant frequency is shifted from 3.2853 to 3.1476 GHz and in the anisotropic case the frequency is shifted from 3.2852 to 3.1478 GHz. This almost indistinguishable result indicates that although liquid crystals are anisotropic materials, however in a full-wave electromagnetic simulation (e.g. CST) with good approximation, liquid crystals can be simply be simulated as isotropic material with a single effective permittivity for the two extreme states along the z-axis. This will not only simplify the simulation but will also reduce the computational cost.

3.3.3 Fringing field distribution

In order to investigate the effects caused by fringing fields on the sides, an extra length (ΔL) is added to both sides of the patch along its x-axis, (shown in Fig. 3.4).

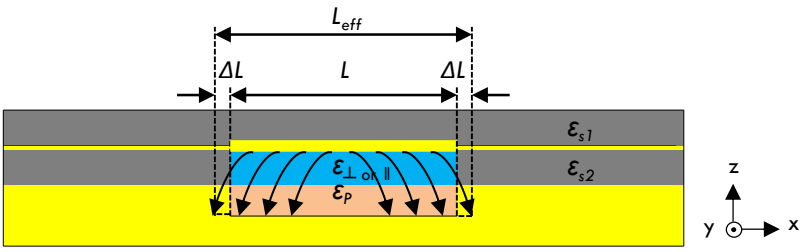

Figure 3.4. Cross-section of the resonator. ΔL distance added on both sides of the patch to cover approximately the entire E-field.

According to [114], this distance can be expressed as a function of the effective relative permittivity ε_{eff} and the width-to-height ratio, defined as

$$\Delta L = 0.412h \times \frac{(\varepsilon_{eff} + 0.3)}{(\varepsilon_{eff} - 0.258)} \times \frac{(\frac{W}{h}) + 0.264}{(\frac{W}{h}) + 0.8} \tag{3.4}$$

with ε_{eff} expressed by

$$\varepsilon_{eff} = \frac{\varepsilon_r + 1}{2} + \frac{\varepsilon_r - 1}{2} \left[1 + \frac{12h}{W}\right]^{-1/2}. \tag{3.5}$$

Therefore the ε_{eff} of the patch equals to 2.84, with ΔL of around 0.49 mm and L_{eff} equal to 28.98 mm. The simulation effects of these values are discussed throughout section 3.4.

3.4 Full-wave electromagnetic simulation

In order to simulate and validate the final structure, Table 3.2 was derived from the available literature indicating various practical samples of liquid crystals and their corresponding properties.

Table 3.2. Properties of liquid crystal samples. Relative permittivity and loss tangent δ values for nematic liquid crystal at lower microwave frequency (L to C-band) and room temperature of 20 °C.

Liquid Crystal samples	Perpendicular		Parallel		$\Delta\varepsilon$	f_c	Ref.
	$\varepsilon_\perp$	tan $\delta_\perp$	$\varepsilon_\parallel$	tan $\delta_\parallel$			
K15 (5CB)	2.72	0.03	2.90	0.03	0.18	1-5 GHz	[90], [96]
BL037	2.35	0.06	2.61	0.06	0.26	1 GHz	[90]
E7	2.72	0.12	3.17	0.02	0.45	5-6 GHz	[7]

3.4.1 Nematic liquid crystal simulation

3.4.1.1 E-series and BL-series

Two of the initial series of nematic liquid crystals produced by Merck for microwave and millimetre-wave applications were the E-series (E44, E48, E7) and the BL-series (BL003, BL006, BL037) [118]. In order to test and validate the designed tunable S-band resonator, the latest samples of E-series, E7 and the BL-series, BL037 (Table 3.2) were used for this simulation. Resonant frequency shifting for both samples was investigated, using the time domain solver and hexahedral meshing.

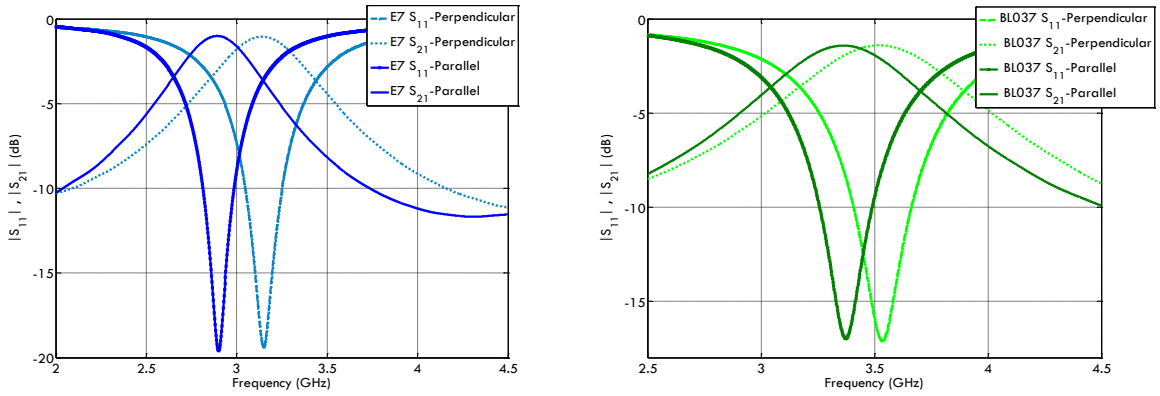

(a) (b)

Figure 3.5. S-parameters for E7 and BL037. The simulation result demonstrates central frequency shift of: (a) around 5.6% for E7 (E-series) and (b) around 5.34% for BL037 (BL-series).

The full-wave electromagnetic simulation results demonstrate a frequency variation from 3.15 to 2.90 GHz (τR = 7.95%) for E7. In this example the bandwidths (at -10 dB) are around 200 MHz with 1.05 dB insertion loss for the perpendicular case and 1.0 dB for parallel state. In the BL037 mixture, the centre frequency shifts from 3.53 to 3.37 GHz, corresponding to a tuning range (τR) of 4.63% and bandwidths of around 250 MHz at -10 dB. The insertion loss however in this example is around 1.40 dB, owing to higher liquid crystal loss tangent (Fig. 3.5). Furthermore, the simulation was as well tested with extended length of 0.49 mm on each side for fringing field's coverage, but given that the tuning was only improved by less than 0.01%, the minor effect caused by the fringing field was not encountered.

3.4.1.2 Standard K15

5CB (4-pentyl-4'-cyanobiphenyl) also commonly known as K15 ($C_{18}H_{19}N$-molecular formula) are quasi-standard nematic liquid crystals, which have well known microwave properties at the targeted operational frequencies. Fig. 3.6 illustrates the colourful pattern of K15 (5CB) liquid crystal molecules under polarized light.

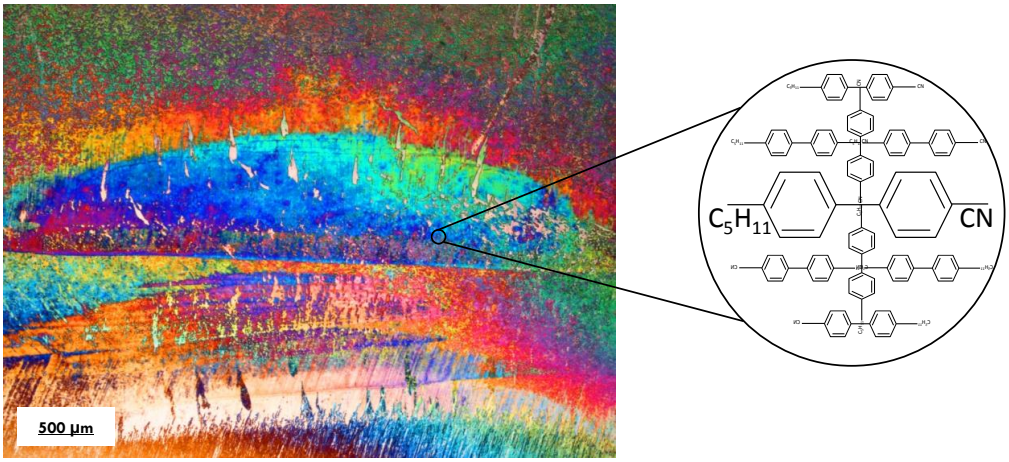

Figure 3.6. K15 pattern. Optical microscope image of K15 nematic liquid crystal under polarized light. This type of liquid has a density of 1.008 g/cm3 (at 25 °C), a boiling point of 140-150 °C and a molecular weight of around 249.35 g/mol.

K15 nematic liquid crystals are generally used as a benchmark for evaluating tunability in liquid crystal microwave devices, due to their wide commercial availability, lower cost compared with other liquid types and acceptable $\Delta\varepsilon$ [119]. As a result, to assess the designed resonator, the K15 relative permittivity values from Table 3.2 were used in the simulation. The completed tunable S-band resonator (see Fig 3.2) CST model and its corresponding field distribution are demonstrated in Fig. 3.7 and Fig. 3.8 respectively.

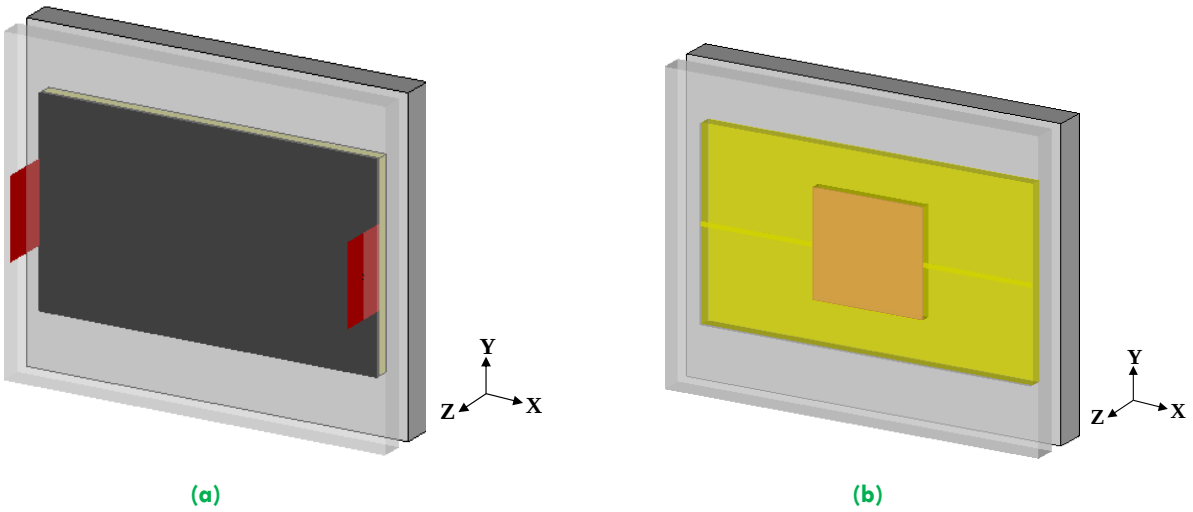

Figure 3.7. Tunable liquid crystal resonator. Prospective view of the designed resonator in CST consisting of with top and bottom covers, (a) top flipped Duroid 5880 substrate with two ports, (b) bottom ground layer and the polyimide layer (RT/Duroid TMM3) substrate in the central.

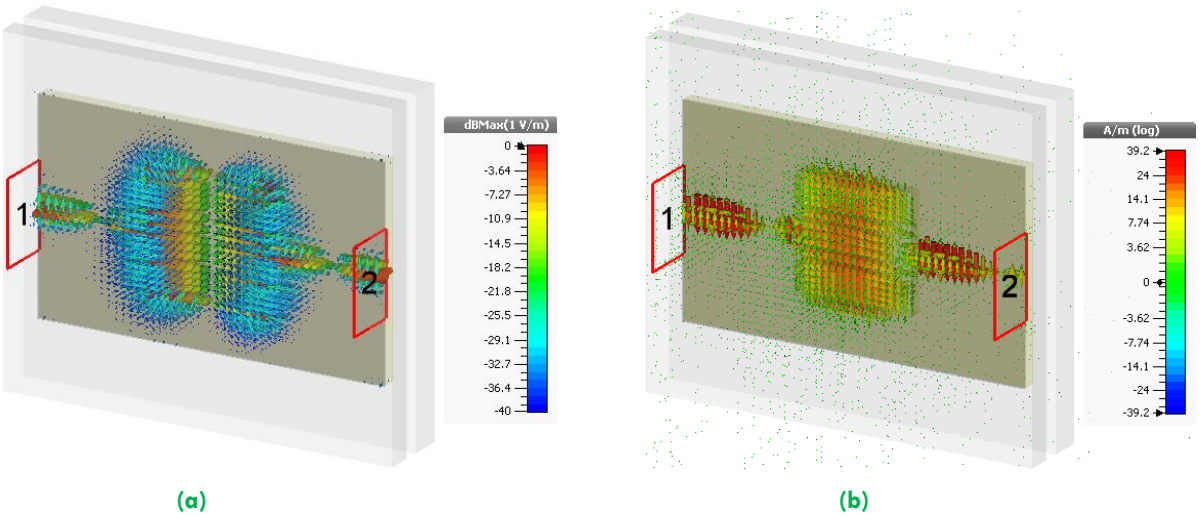

Figure 3.8. E and H instantaneous field distribution. (a) E-field, (b) H-field distribution of the simulated resonator, filled with K15 nematic liquid crystal mixture.

Through varying the relative permittivity of the K15 from $\varepsilon_{\perp}$ = 2.72 (perpendicular state) to $\varepsilon_{\parallel}$ = 2.90 (parallel state) (see Table. 3.2), the resonant frequency changes from 3.28 GHz to 3.14 GHz providing a tuning range (τR) of around 4.4% and a tunability (τ) of 4.45% with respect to the lower frequency. In this simulation the bandwidth for S_{11} < -10 dB is 250 MHz for the unbiased state and 225 MHz for the biased state. The S_{11} parameters at resonance for both cases are around -21 dB and the maximum S_{21} parameters are better than -1 dB (Fig. 3.9).

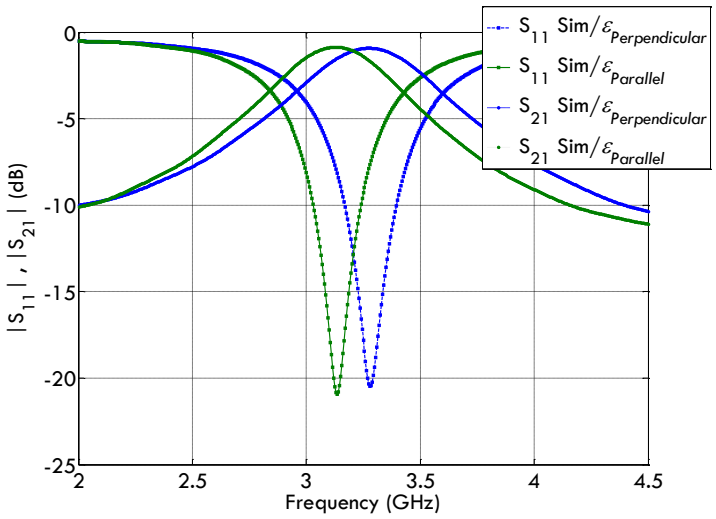

Figure 3.9. Simulation-using K15 nematic liquid crystal. The results indicate that by applying relative permittivity value the centre frequency of the resonator shifts from 3.28 GHz to around 3.14 GHz.

3.5 Prototype and measurement

3.5.1 Fabrication methodology

To validate the simulation results, a prototype of the tunable S-band resonator filled with liquid crystal was fabricated and tested. This multi-layer structure involved milling the substrates, etching, polyimide coating and rubbing, liquid filling and measuring. This fabrication was achieved through collaboration with the Defence Science and Technology Organization (DSTO). The initial step involved selecting the appropriate substrate for the top layer. From the available microwave materials, high frequency Duroid 5880 laminate from Rogers was chosen, due to its low relative permittivity ε_{s1} = 2.20, low loss tangent tan δ_{s1} = 0.0012, wide commercial availability, low moisture absorption and excellent chemical resistance.

In order to design the top square patch and the corresponding feed lines, an etching process was considered (see Fig. 3.10). In this process, multiple masks from the top patch shape were patterned and printed on a glass films. Using UV light exposure these patterns were printed on one side of the Rogers substrate. The layers were then placed in an tray filled with Ammonium Persulphate $(NH_4)_2S_2O_8$ combined with water. Through carefully agitating the tray, the copper of the un-exposed areas were oxidized, and the patterns were developed.

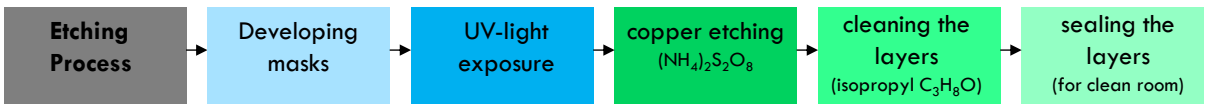

Figure 3.10. Etching process. The time allocated for this process is approximately 10 min. The layers require UV light exposure of around 30-60 sec and chemical etching of around 5-7 min. The time required for chemical etching can be reduced through brushing the copper surfaces in prior with Isopropyl Alcohol (CH3)2CHOH (IPA).

The middle layer was also manufactured using RT/Duroid 5880 (ε_{s2} = 2.20, tan δ_{s2} = 0.0012, h_{s2} = 0.508 mm). Since in this layer, a square cavity was required in the centre of the substrate, a computer-controlled milling machine was used to form a 28 by 28 mm cavity with 0.5 mm thickness in the centre of the substrate. Even though the milling caused rounded corners, the effect was believed to be minimal.

The final bottom layer consisted of a metal ground plane with a filled cavity for accommodating a substrate coated with polyimide films. This metal layer was simply designed using copper and the cut out cavity was filled with TMM3 thermoset microwave substrate (ε_p = 3.27, tan δ_p = 0.0020, h_p = 0.508 mm) from Rogers, which has high chemical process resistance, high thermal coefficient (+37 ppm/K) and high insulation resistance (>2000 GΩ). This TMM3 substrate was coated with the required polyimide layer as explained next.

The next step involved coating the top copper patch and the TMM3 bottom layer with a thin layer of polyimide, in order to initially align the liquid crystal molecules. In this work the layers were first spin coated with an approximate 4-6 μm thickness of Pi2611 (HD Microsystems) polyimide and then placed in a heat oven for 60 min at 300 °C, for the curing to take place. The curing temperature can vary between 180-300 °C depending on the type of the polyimide. The temperature should change gradually to prevent an undesired effect on the electromagnetic characteristics of some standards RF substrates at 300 °C.

Finally these thin polyimide films are mechanically rubbed. The rubbing process is often done using a velvet cloth by applying a soft force whilst rubbing in a given direction over the substrate surface. The result of this rubbing is a microscopic grooving of the polyimide surface, which leads to a pre-alignment of the liquid crystal molecules (Fig. 3.11 and Fig. 3.12).

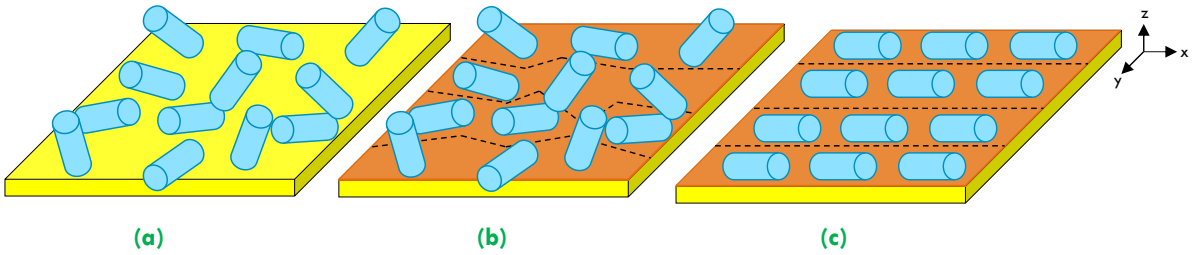

Figure 3.11. Alignment of the liquid crystal molecules. (a) Random orientation of the liquid crystal molecules without polyimide coating, (b) random orientation with polyimide film coating and (c) aligned liquid crystal molecules after polyimide coating and rubbing.

Finally after insertion of the liquid crystal K15 (standard), all layers were mounted to form a sandwich cell structure. The complete resonator was then placed in a Teflon/PTFE (ε_{C1}= 2.1) top cover and a Plexiglas/PMMA (ε_{C2} = 3.4) bottom cover and screwed around the edges to seal the cavity and avoid any liquid leakage (see Fig. 3.12 and Table 3.3).

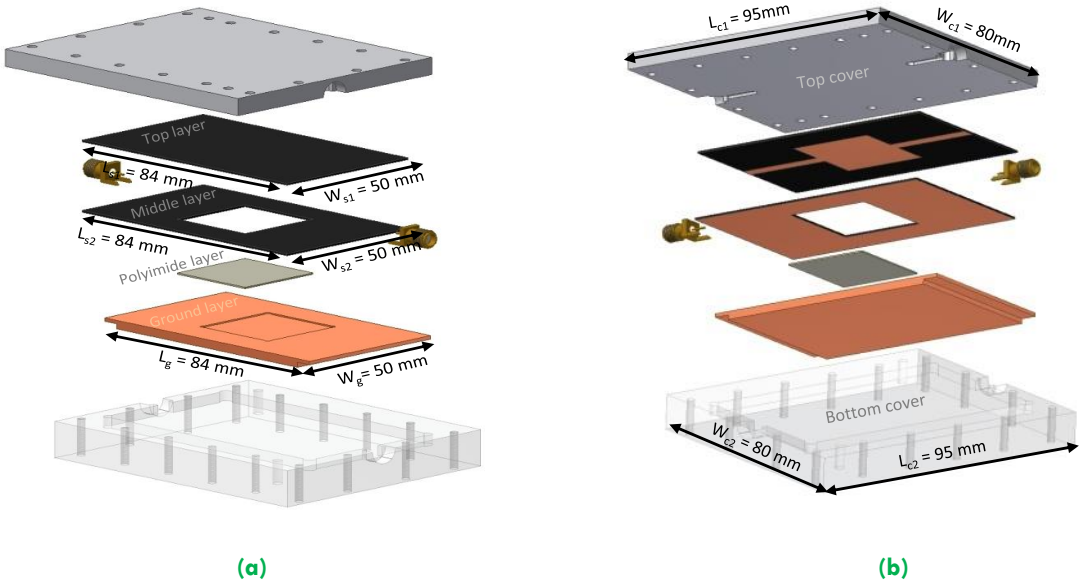

Figure 3.12. Complete S-band tunable resonator. (a) Top view and (b) bottom view of the multiple resonator, illustrating each individual layer along with the top and bottom shielding.

Table 3.3. Dimensions of the fabricated prototype. The table below provides all dimensions along with their permittivity and loss tangent values.

	Material	Length	Width	Thickness	Permittivity	Loss tan δ
Top layer	Substrate (duroid 5880)	L_{s1} = 84 mm	W_{s1} = 50 mm	h_{s1} = 0.508 mm	ε_{s1} = 2.20	tan δ_{s1} = 0.0009
	Patch (copper)	L_{cu_p} = 28 mm	W_{cu_p} = 28 mm	h_{cu_p} = 17 μm	NA	NA
	Feeding lines (copper)	L_{cu_f} = 28 mm	W_{cu_f} = 1.3 mm	h_{cu_f} = 17 μm	NA	NA
Middle layer	Substrate (duroid 5880)	L_{s2} = 84 mm	W_{s2} = 50 mm	h_{s2} = 0.508 mm	ε_{s2} = 2.20	tan δ_{s2} = 0.0009
Bottom layer	Ground layer (copper)	L_g = 84 mm	W_g = 50 mm	h_g = 3 mm	NA	NA
	Polyimide layer (TMM3)	L_p = 28 mm	W_p = 28 mm	h_p = 0.50 mm	ε_p = 3.27	tan δ_p = 0.002
Top cover	Material (Teflon/PTFE)	L_{c1} = 95 mm	W_{c1} = 80 mm	h_{c1} = 6 mm	ε_{c1} = 2.0	tan δ_{c1} = 0.0015
Bottom cover	Material (Plexiglas/PMMA)	L_{c2} = 95 mm	W_{c2} = 80 mm	h_{c2} = 8 mm	ε_{c2}= 3.60	tan δ_{c2} = 0.001

3.5.2 Setup and measurements

To measure the structure, two Mini-Circuits wideband bias-tees (ZFBT-4R2G) with a maximum frequency of around 4.2 GHz were connected to both sides of the structure, through SMA (vertical jack-stainless, gold) connectors. By connecting the bias-tee pins to the DC power source and the network analyser to the input and output connectors, (N5230A PNA series-Agilent Technologies) measurements of both the input reflection coefficient (S_{11}) and forward transmission (S_{21}) were carried out, Fig. 3.13. To avoid interference and unwanted RF/microwave noise signals, the prototype test measurements were taken in the anechoic chamber.

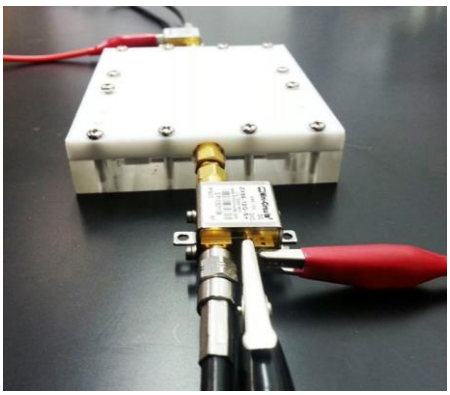

Figure 3.13. Packaged resonator. Tunable S-band resonator, filled with K15 liquid crystal and connected to bias-tees.

To measure the fabricated structure and to quantify the effect of the polyimide films, a comparison is made between a device with polyimide films and the same device without polyimide films. The measured results for biased and unbiased cases are then compared with the full-wave electromagnetic simulation results.

In the first measurement the bottom (TMM3) and top layer (Duroid 5880) were spin-coated with thin layers of polyimide film and then cured for approximately an hour at 300 °C. The surfaces were then mechanically softly rubbed using a velvet cloth Fig. 3.14. The layers are then formed in a sandwich cell structure to enclose the liquid in its cavity, with Duroid and metal on top and bottom (Fig. 3.12).

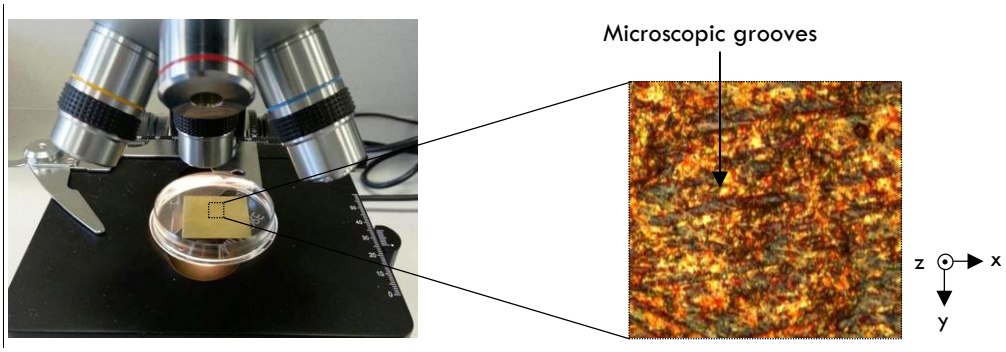

Figure 3.14. Spin-coated polyimide surface. Optical microscopic image of the TMM3 layer spin coated with 3-4 µm thickness of polyimide (Pi2611) and rubbed mechanically along the x-axis.

Through applying a bias voltage of $V_b = 0\,\mathrm{V}$ and increasing it to the maximum value of $V_b = 30\,\mathrm{V}$, the liquid crystal molecules change their orientation from perpendicular to parallel, causing a shift in the resonant frequency, Fig. 3.15. As discussed previously, this switching speed of the applied voltage is not the limiting factor but rather it is the response time of the liquid crystal material.

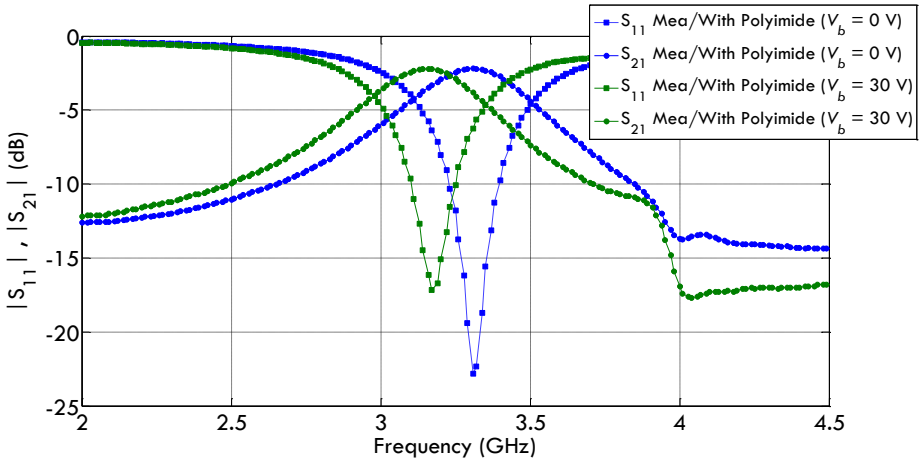

Figure 3.15. Measurement-presence of polyimide films. Through applying external bias voltage to the shift in the resonant frequency is achieved.

In this case by adding polyimide film to the top and bottom of the cell, i.e. to the surfaces which are in contact with the K15, a frequency tuning range (τR) of 4.01% from 3.30 GHz to 3.17 GHz is achieved, showing a satisfactory correspondence with the simulation results. The bandwidth in the first case, with no voltage applied is about 175 MHz and is decreased to 150 MHz when an electric field above V_{th}, i.e. V_b = 30 V is applied. The drop in the S_{21} curves around 4 GHz in both cases are explained by the maximum range of the bias-tee used (4.2 GHz).

However in the second measurement the bottom and the top layers are placed in the resonator element without any polyimide coating around the liquid crystal cavity. The results presented in [66] indicate that by applying a similar bias voltage (V_b = 0 to 30 V), an approximate frequency tuning range (τR) of around 2.14% is achieved. In this case, the minimum input reflection coefficients (S_{11}) for both cases are around -23 dB and transmission coefficients (S_{21}) are -2.2 dB for both measurements. The main losses in this experiment are mainly due to K15 sample. These results indicate approximately close to half of the maximum simulated tuning range can be obtained with random alignment of liquid crystal molecules in an unbiased state when the polyimide coating is eliminated. However additional testing with other liquid crystal materials is necessary to show this conclusion applies more broadly.

3.6 Conclusion and summary

This chapter describes a novel tunable liquid crystal resonator design with an operating frequency of around 3.5 GHz (S-band). The work involved a literature review, theoretical calculations for a liquid crystal multi-layer structure and fabrication of two different tunable resonators using the standard K15 (5CB) liquid crystal sample.

In this work, a tuning range of 4% is achieved when polyimide layers rubbed with a velvet cloth are used and 2.1% is achieved when the boundary layers of the liquid crystal cavity are free of polyimide coating. Although polyimide layers are common for aligning liquid crystal molecules in the unbiased state, this research study has quantified the tuning range in absence of these polyimide layers, demonstrating around half of the tuning range with polyimide, corresponding also to the predicted tuning range. In order to improve the overall tuning range and reduce the insertion loss an improved model of this resonator is investigated in the next chapter through both simulation and prototype fabrication.

Chapter 4

High Performance Tunable Resonator Using Liquid Crystal Mixture

IN this chapter a high performance tunable resonator is presented. The designed device operates at S-band (2-4 GHz) and exhibits more than 8% of experimentally demonstrated frequency tuning. The chapter provides the full-wave electromagnetic model of the resonator, followed by its step by step fabrication procedure. In order to validate the designed prototype a comparison between the simulation and the measurement is presented and the results are discussed.

4.1 Introduction

A tunable resonator operating at S-band is presented in this work which makes use of a new high performance liquid crystal mixture designed specifically for microwave applications. Experimental results demonstrate a frequency tuning range of 8.2% and low insertion loss at S-band microwave frequency. This resonator at this relatively low frequency opens new possibilities for future applications of liquid crystal at an even lower microwave frequency, e.g. for body-centric communications which require tunability at a low microwave frequency and shape flexibility.

4.2 Tuning enhancement

4.2.1 Material variation: full-wave simulation

The tuning range and the corresponding loss tangent in the previously designed resonator depended on: 1. the device's operational frequency, 2. electrical characteristics of the substrate and 3. dielectric anisotropy of the liquid crystal. In this research, given that our aim was to investigate liquid crystal for tuning lower microwave frequency devices, due to common communications bands operating below 5.80 GHz, the centre frequency remained unchanged. Furthermore the top and middle layer of the resonator was also designed using the RT/Duroid 5880 substrates with a relative permittivity of 2.20, comparable with liquid effective relative permittivity (~ 2.2-3.5), resulting in a potentially high microwave tuning range.

However one important change which could greatly improve tuning range, is filling the central layer of a liquid crystal microwave device with a higher dielectric anisotropy liquid crystal mixture. From the available literature (see Table 2.1), BL006 and E7 produced by Merck appear to have higher dielectric anisotropy $\Delta\varepsilon \approx 0.43\text{-}0.5$ compared with other liquid crystal samples around a centre frequency of 5 to 8.5

GHz. However through investigating and researching other available options, the author became aware of a new liquid crystal mixture called "GT3-23001", developed specifically for microwave applications by Merck.

This liquid had high dielectric anisotropy ($\Delta\varepsilon$ = 0.8) at microwave frequencies, high clearing point (173 °C), wide operating temperature range (-20 to 100 °C) and very low dielectric loss tangent. This liquid crystal mixture was produced aiming at manufacturing tunable phase shifters, phased array antennas, resonators, reflectarrays antennas, adapting matching circuits and adaptive filters. Table 4.1 illustrates the physical properties of this mixture provided, as by the manufacturer.

Table 4.1. GT3-23001 liquid crystal. The electrical characteristics of the new mixture at 20 °C.

liquid crystal mixture	$\varepsilon_{\perp}$	$\varepsilon_{\parallel}$	$\Delta\varepsilon$	tan $\delta_{\perp}$	tan $\delta_{\parallel}$
GT3-23001	2.50	3.30	0.8	0.0143	0.0038

In order to validate this novel mixture in the designed S-band resonator, at first the tuning range was validated through full-wave electromagnetic simulation, using the CST time domain solver and hexahedral meshing.

As demonstrated (Fig. 4.1), the simulation predicts a frequency shift from 2.93 to around 2.69 GHz, corresponding to a frequency tuning range (τR) of 8.54% and tunability (τ) of 8.92% with respect to the lower frequency and 8.19% with respect to the higher frequency. The simulated reflection coefficients in this case are -22.5 dB for a cavity permittivity of $\varepsilon_{\perp}$ (corresponding to V_b = 0 V) and -23.7 dB for $\varepsilon_{\parallel}$ (at saturation voltage), with an insertion loss of approximately 0.80 dB and 0.69 dB respectively. After finalizing the full-wave simulation, the next step was validating these results through manufacturing the resonator.

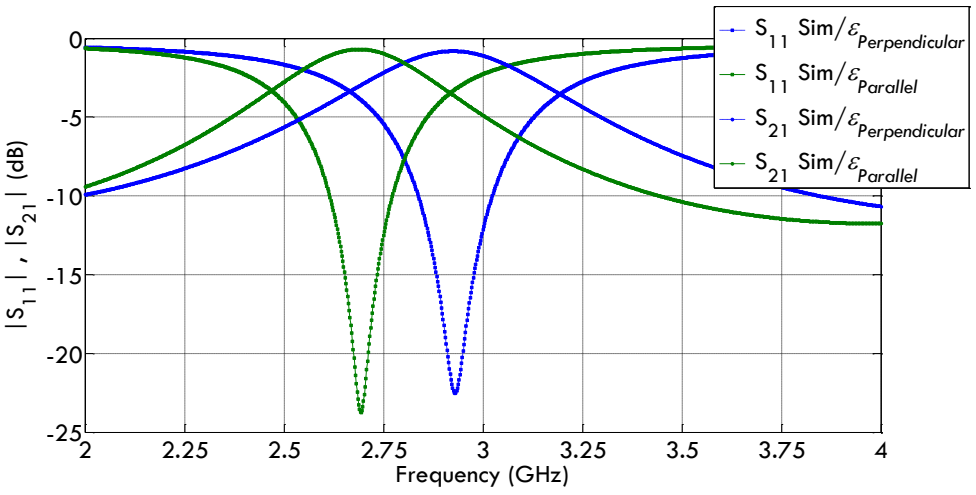

(a)

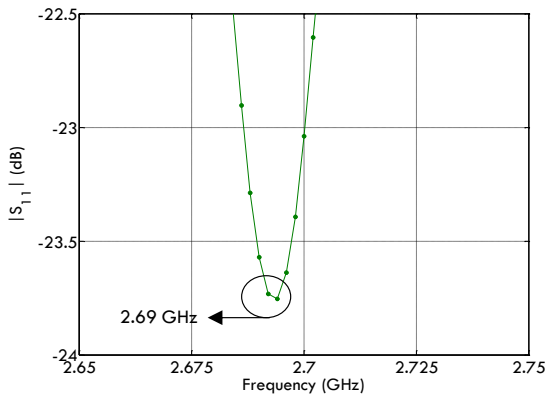

(b)

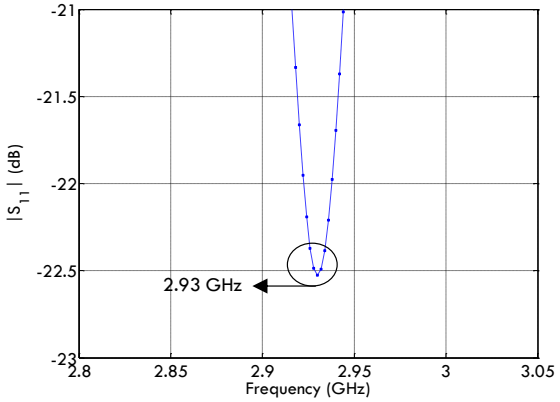

(c)

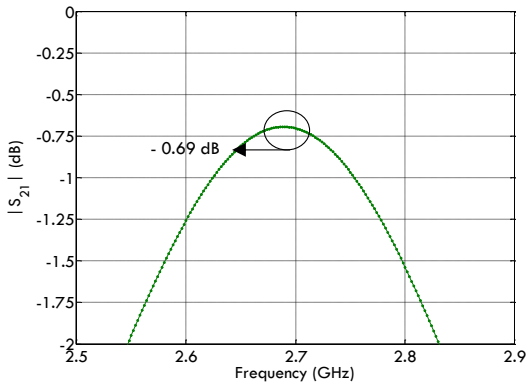

(d)

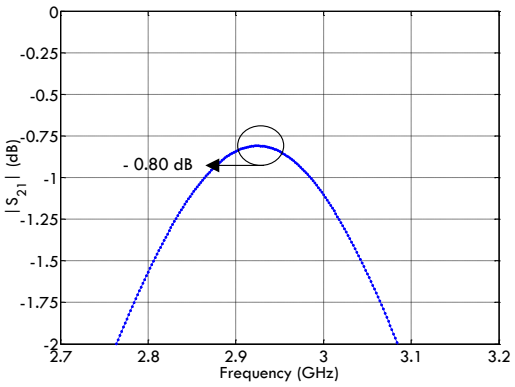

(e)

Figure 4.1. Simulation using GT3-23001 liquid crystal mixture. (a) illustrates the frequency shifting of the resonator from 2.93 to 2.69 GHz, (b) frequency when $\varepsilon_{eff} = \varepsilon_{\perp}$, (c) frequency when $\varepsilon_{eff} = \varepsilon_{\parallel}$, (d) total loss tangent when $\varepsilon_{eff} = \varepsilon_{\perp}$ and (e) total loss tangent for when $\varepsilon_{eff} = \varepsilon_{\parallel}$.

4.3 Prototype and measurement

4.3.1 Fabrication procedure

For the sake of consistency, the resonator dimension and the geometry of the structure were similar to the previously discussed design (Sec. 3.2 and 3.3). In that case however, the fabrication of this multi-layer tunable resonator was achieved through collaboration with the Institute for Microwave Engineering and Photonics, Technische Universität Darmstadt (TUD) in Germany, which provided precise and reproducible patterning and developing of the polyimide film coating. The manufacturing procedure is discussed in detail below.

4.3.1.1 Etching and patterning

To construct the resonator patch structure, feeding lines and the bottom polyimide layer, a chemical etching process was used. In this process initially the patterns were printed on transparent films, placed on top of the substrates and were then exposed for around 30 to 60 seconds (each layer). The exposed layers were then placed in a tray filled with ammonium persulphate $(NH_4)_2S_2O_8$ combined with running water. Through slowly shaking the tray, the unexposed copper areas in the substrates dissolved in the ammonium persulphate and the pattern appeared. Eventually these layers were brushed and cleaned using isopropyl alcohol $(CH_3)_2CHOH$ (IPA).

4.3.1.2 Polyimide film development

The next stage required developing the polyimide film (PI) on the top and bottom of the liquid crystal cell. This process consists of four sequential steps, which are generally referred to as: *coating*, *spinning*, *curing* and *rubbing*, Fig. 4.2.

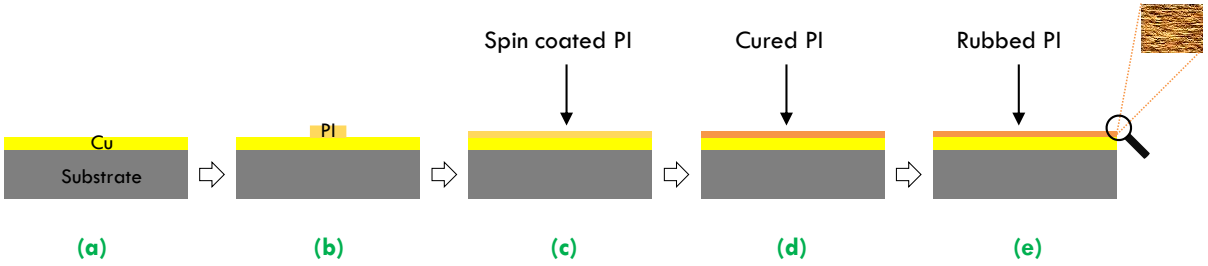

Figure 4.2. Polyimide coating process. After copper coating/patterning (a), a small amount of polyimide (PI) is applied (b), which is then distributed evenly spin coating (c). The substrate is then cured by baking (d) and ultimately the polyimide layer is given fine grooves with a preferential direction by rubbing (e).

For this work, the polyimide mixture was prepared using 300 millilitres of 2,2,2-Trichloroethanol ($C_2H_3CL_3O$) organic ethanol (1.55 g/mL), combined with 0.45 grams of Nylon 6/polycaprolactam-$(C_6H_{11}NO)_n$ (1.084 g/mL). The *coated* top (copper patch) and bottom layers (polyimide layer-TMM3) were individually placed in a *spinning* machine for about 15 second at a speed of 3000 rpm, resulting in a polyimide thickness of around 0.3-0.4 µm, Fig 4.3. In this process the feeding lines were coated with polyimide mixture for ease of processing.

Figure 4.3. Spinning machine. By adjusting the speed to 3000 rpm and running it for 15 sec, the polyimide mixture on the surface was equally spread to about 0.3-0.4 µm thickness.

The next step required polyimide *curing,* which results in evaporation of the ethanol compound. In this process, the layers are preheated on the heat sink to about 90 ^{o}C for 10 minutes, which prevents substrate damage. After preheating, the layers are then placed in the main oven for the key curing process to take place, which requires approximately three hours, Fig 4.4.

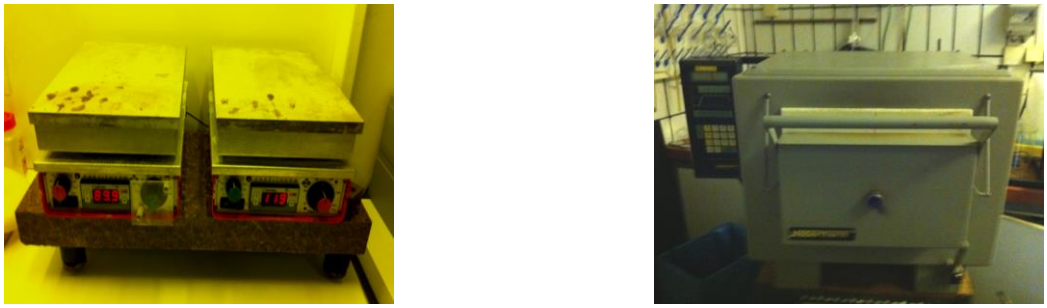

(a) (b)

Figure 4.4. Polyimide curing. (a) Heat sink used for preheating the layers, (b) main digital oven used for polyimide curing through step by step heating.

To avoid an unpredictable effect on the electromagnetic characteristics of the substrate, the main heating in this process proceeds through step by step. In the initial phase, the layers are heated from room temperature 20 °C to around 90 °C. This temperature (90 °C) is achieved after approximately 30 minutes and remains unchanged for about an hour. In the next phase the temperature is again raised to 180 °C for the final curing to take place. This step requires 30 minutes for the temperature to rise and one hour for the curing process to complete. After completion, the layers are kept at room temperature for the cooling to take place, Fig. 4.5.

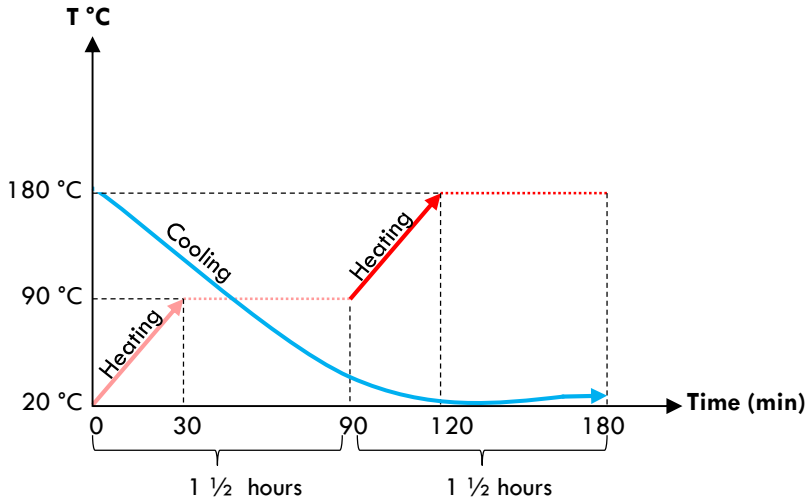

Figure 4.5. Polyimide curing development. The plot illustrates the total time required for the two step polyimide curing, using the main digital heat oven.

The final step required mechanical *rubbing*. In this process the rubbing was achieved using a large velvet covered roller, similar to the one used in the liquid crystal display (LCD) industry, but in a smaller scale designed at TUD, Fig. 4.6.

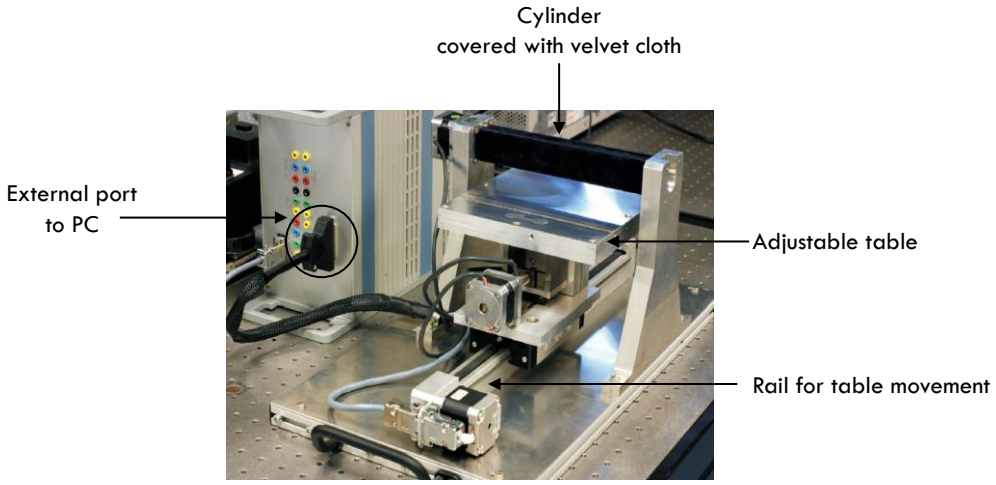

Figure 4.6. Rubbing machine. Photograph of the rubbing machine, programmed in MATLAB through its computer interface.

In this step the velvet covered roller rotates while the table underneath is slowly moved below the roller. The pressure with which the roller presses on the substrate is adjustable by moving the table vertically such that for a given substrate thickness the same pressure is always obtained.

In this work the adjustable table was set to height of 0.5 mm and the rubbing was achieved over three repeated passes of the cylinder. The results of this rubbing are microscopic grooving on the polyimide film which leads to a pre-alignment of the liquid crystal molecules. In order to illustrate these grooves, the rubbed layers were placed under a high resolution scanning electron microscope and the images are shown in Fig. 4.7.

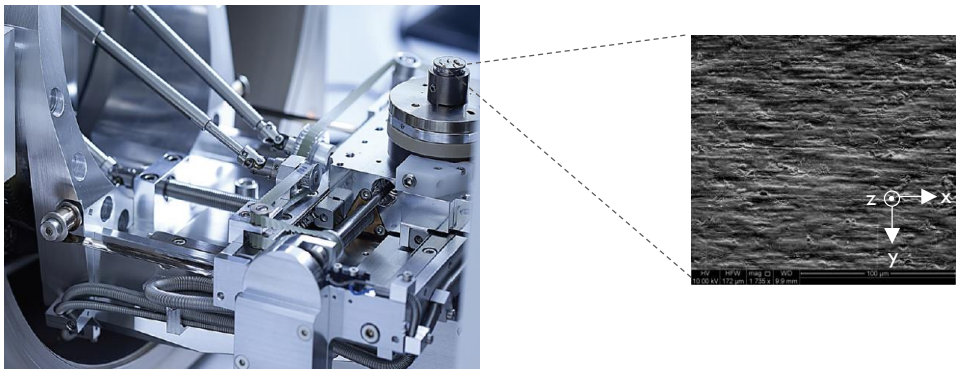

Figure 4.7. Microscopic grooves. The SEM image above illustrates of the mechanically rubbed thin layer of polyimide film (0.3-0.4 μm). The image is taken by a Quanta-450 from a distance of 10 mm with high magnification of 1735 x.

4.3.2 Measurements

The resonator cell is then filled with the new high performance liquid crystal GT3-23001 with dielectric parameters reported in Table 4.1. After insertion of the liquid crystal, all layers were mounted to form a sandwich cell structure. The complete resonator element was then placed in PTFE/Teflon top and PMMA/Plexiglas bottom covers to seal the cavity and avoid any liquid leakage, Fig. 4.8.

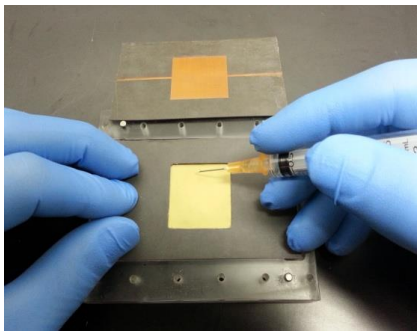

Figure 4.8. Liquid filling process. Image of the final fabricated S-band resonator, during liquid crystal (GT3-23001) filling process.

To measure the resonator response, a bias voltage varying from V_b = 0 V to V_b = 30 V was applied to the liquid crystal cell through wideband coaxial bias-tees (ZX85-12G-S+) from Mini-Circuits with frequency range of 0.2 MHz to 12 GHz. Through using network analyser (N5230A PNA series-Agilent Technologies) the scattering

parameters were measured. The results indicated that for V_b > 5 V, the resonant frequency of the structure moves from around 2.93 GHz in the unbiased state to approximately 2.70 GHz, when saturation bias voltage is applied (V_b = 30 V). This result demonstrates an approximate tuning range (τR) of 8.2% for this prototype measurement, and tuning (τ) 8.5% with respect to lower frequency, which closely match the CST simulations, Fig. 4.9.

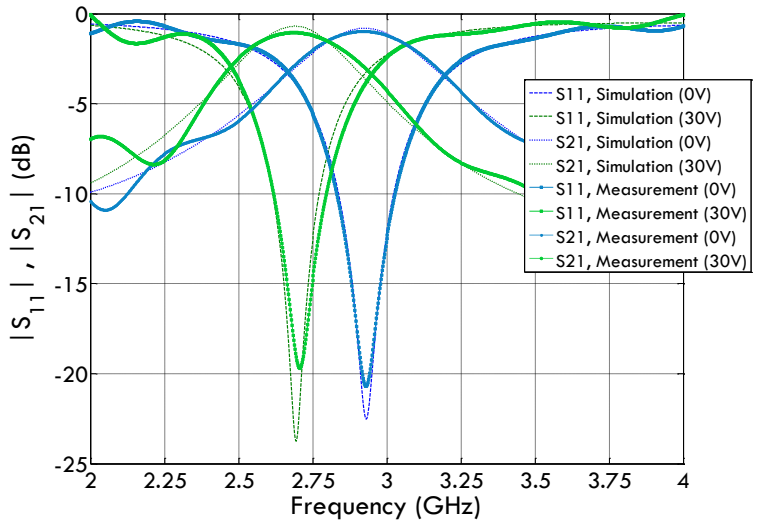

Figure 4.9. Simulation and measurement comparison. The simulation and measurements for the resonator filled with GT3-23001 liquid crystal sample illustrate around 8.5% to 8.2% of frequency tuning, which are in good agreement.

The reflection coefficients (S_{11}) in this case are -20.7 dB at 0 V and -19.7 dB at saturation (30 V). An insertion loss of 0.97 dB can be observed in Fig. 4.10 for the unbiased state and 1.0 dB for the biased state. The continuous tuning range of the liquid crystal GT3-23001 can also be compared to similar measurements performed in the same test fixture with the commonly-used liquid crystal K15 as reported in Chapter 3.

The comparison demonstrates a doubling of the frequency tuning range, from 4% with standard K15 liquid crystal to around 8.2% when the GT3-23001 is used. The results also demonstrate a decrease in the total insertion loss from 2.2 dB in the previous design (K15 sample) to 1.0 dB for this new high-performance liquid crystal.

Table 4.2 compares the results achieved from this work with previously presented work in the literature.

Table 4.2. Comparison of frequency tunability. Simulation and measurement comparison from the proposed with previously discussed literature.

Source	Operation freq. (GHz)	Sim.	Meas.
Presented work [120]	2-4	8.5%	8.2%
Previous work (Chap. 3) [66]	2-4	4.4%	4.0%
Martin et al. [95]	4-6	2.6%	3.0%
Martin et al. [96]	4-5	NA	5.4%
Liu et al. [7]	5-6	8.15%	4.15%

The above result for the resonator presented in this work, indicates around twice the improvement in the frequency tuning range compared with the previous work reported in chapter 3 [66] and close to three times higher tuning, compared with the work reported in [95], with a similar microwave frequency range. Moreover the presented work demonstrates equivalent improvement from the results achieved by full-wave electromagnetic simulation and through prototype measurements. This resonator at this relatively low frequency opens new possibilities for future applications of liquid crystals at an even lower microwave frequency, e.g. for body-centric communications which require tunability at a low microwave frequency and shape flexibility.

4.4 Conclusion and summary

In this chapter, an improved model of the novel tunable liquid crystal resonator is presented and investigated though both simulation and prototype measurement, with operational frequency of around 3 GHz. The designed S-band resonator uses the novel high performance GT3-23001 as a tunable dielectric in its central layer.

Through applying external bias voltage to the top and bottom layer of the liquid crystal cell a frequency tuning of around 8.5% is predicted using a full-wave

electromagnetic simulation. A prototype of the resonator was manufactured and tested to validate these results.

The measured scattering parameters for both reflection and transmission indicated 8.2% of frequency tuning in the 2 to 4 GHz range. To the best of our knowledge, the novel resonator with 8.2% frequency tuning is the best designed liquid crystal tunable resonator, with operational frequency of S-band, achieved to date.

Chapter 5

Stepped-Impedance Resonator Modelling

IN this chapter the possibility of using a simple lumped-element circuit simulation for rapid calculation of the performance of liquid crystal devices at microwave frequencies is presented. Based on stepped-impedance resonator theory, the previously proposed resonator was modelled as a half-wavelength resonator patch above a multi-layer substrate, with liquid crystal as its central layer. Through using different liquid crystal samples and three different approaches: lumped-element circuit simulation, full-wave electromagnetic simulations and prototype measurements, the results are compared and validated.

5.1 Introduction

Various multi-layered liquid crystal tunable devices have been presented in the literature, where the operational frequency, tuning and the loss tangent have been mainly discussed based on the full-wave electromagnetic simulation model. Even though simulation software (e.g. CST) provides an accurate full-wave simulation model, these require in many cases an unacceptably extensive computational time. This is the case even for relatively simple simulations for example in the framework of multi-parameter optimization. In this work, a lumped-element circuit model for simulation of a multi-layered liquid crystal structure is presented, which demonstrates the possibility of using a simple model for rapid calculation of the performance of liquid crystal devices at microwave frequencies.

5.2 Stepped-impedance resonator modelling

Stepped-impedance resonators (SIR), have been widely discussed in the literature for designing multi-layer structures, due to their simple planar structure, controllable resonant frequency and well established design methods [121]. In [122], an example of a multi-layered lumped element circuit model using SIR for an ultra wideband bandpass filter based on a liquid crystal polymer (LCP) substrate has been presented. The SIR in this work was treated as a cascade of high and low impedance transmission lines, with high impedance lines acting as series inductors, while the low impedance lines act as shunt capacitors.

Similarly, a circuit model of a novel compact bandpass filter with single or multiple notch-bands was illustrated in [123]. The lumped element circuit model was compared with the electromagnetic simulation model and the experimental measurements. The results indicated good agreement between all three observations. In this work the dielectric loss for all layers was neglected with good approximation. In a different case, a compact planar composite low-pass filter, fabricated on LCP organic substrate operating in C and V-band has been demonstrated [124]. The

lumped-element schematic of the filter has been implemented using a combination of a SIRs and folded SIRs. The results illustrate a good match between the lumped, simulation and the measurement results. In a more recent example a lumped-element equivalent circuit model for a microwave bandpass filter, based on a multi-layer ring resonator (MRR) has been presented [125]. An equivalent circuit for this design was introduced for both MRR structures and cascaded block filters. The mathematical model derived from the lumped circuit shows a close match to the filter frequency response. In all cases, a physically correct circuit model allows rapid calculation of approximate performance measures, and provides physical interpretation of design parameters. In this work we use the same theory and principle of the SIR but we design it in order to make it frequency tunable.

5.2.1 Multi-layered SIR design

The previously proposed multi-layer tunable resonator can be defined as a band-pass filter, given that it consists of a stepped-impedance resonator operating at a frequency of around 3.0 GHz. The stepped-impedance resonator can be divided into three main sections, with only two different characteristic impedances: Z_{TL} for the feeding transmission lines, which allow the measurement of reflection and transmission coefficients, and Z_p as the patch impedance (Fig. 5.1).

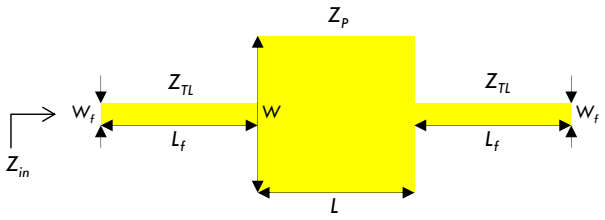

Figure 5.1. Geometry of the SIR. The transmission lines on both sides are modelled by Z_{TL} and the patch is modelled by impedance Z_p. Dimensions are: W_f = 1.3 mm, W = 28 mm, L_f = L = 28 mm.

To design the lumped-element circuit model for the above SIR band-pass filter, initially the multilayer structure was divided into three main layers (as discussed in chapter 3, but repeated here for convenience). The *top layer*, is a half-wavelength (λ/2) resonator square copper patch underneath a Duroid 5880 substrate; the *middle*

layer, consists of two individual layers, a cavity for the liquid crystal samples plus a substrate (TMM3) for providing a surface for polyimide coating; and the *bottom layer*, is a copper plate, forming a ground plane (Fig. 5.2).

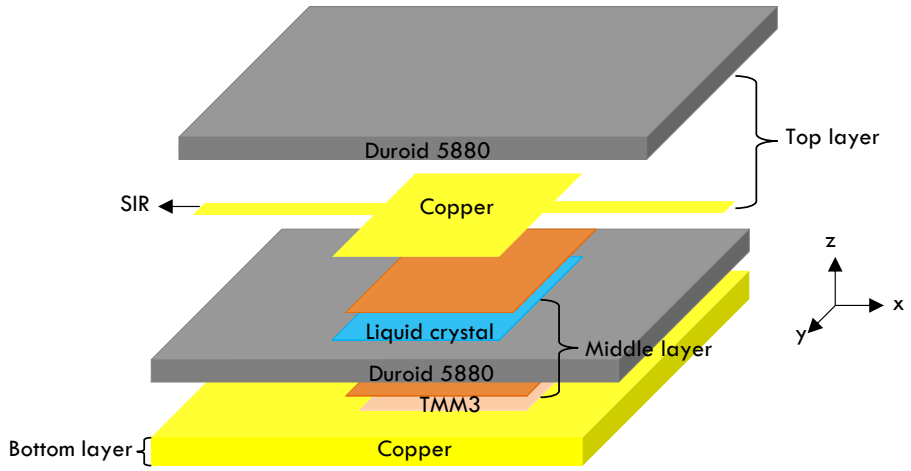

Figure 5.2. Structure cross section. Demonstrates each individual layer, central patch and the feeding lines, acting as a stepped impedance resonator band-pass filter.

5.3 Lumped-element model

5.3.1 Electrical schematic

The transmission lines on both side of the patch can be simply modelled as a series inductance (L_{TL}) and shunt capacitance (C_{TL}) (Fig. 5.3).

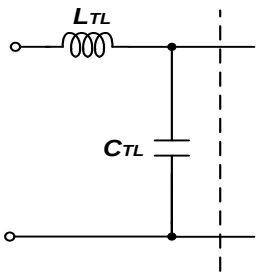

Figure 5.3. Transmission line circuit schematic. Modelled as a series inductance and shunt capacitance.

Because both microstrip impedance conditions are satisfied ($0.1 < \frac{W_f}{h_{s2}} < 3.0$ and $1 < \varepsilon_{r1} < 15$), the total value of series inductance (L_{TL}) and shunt capacitance (C_{TL}) can be calculated using the microstrip impedance formula [126], [127], defined by

$$C_{TL} = \frac{0.67\,(\varepsilon_{r1}+1.41)}{\ln\left(\frac{5.98\,h_{S2}}{0.8w_f+t}\right)} \tag{5.1}$$

and

$$L_{TL} = C_{TL}\,Z_{TL}{}^{2} \tag{5.2}$$

where Z_{TL} is calculated through

$$Z_{TL} = \frac{87}{\sqrt{\varepsilon_{r1}+1.41}} \ln\left(\frac{5.98\,h_{s2}}{0.8w_f+t}\right). \tag{5.3}$$

In this equation h_{s2}, t and w_f (in mm) are the transmission lines height, thickness and track width respectively and ε_{r1} corresponds to relative dielectric constant.

Furthermore, the next stage requires equivalent circuit modelling for the single patch. Since the substrate under the patch in this resonator is a multi-layer structure (consisting of liquid crystal and TMM3 substrate) a basic SIR single lumped element model cannot be applied. For this reason the patch is divided into a number of small segments and a convergence analysis is performed to validate the approach using Advanced Design System (ADS) [128] simulation software. The ADS simulation results indicate a division of four segments for the patch (each $\lambda/8$ wavelength) is sufficient for the rapid estimation of the tunable SIR performance (Sec. 5.3.2).

Finally each division is then replaced with a series inductance (L) and shunt capacitances (C and C_{sub} in series) to produce multilayer low impedance transmission lines, Fig. 5.4, which model the central resonator patch shown in Fig. 5.2.

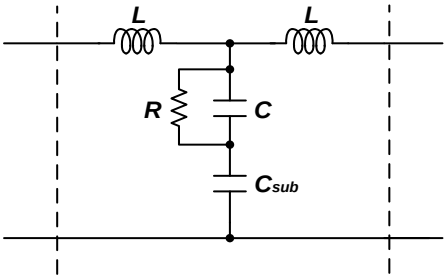

Figure 5.4. Central patch and the middle layer circuit schematic. Modelled as a series inductance, shunt capacitance and parallel resistance.

The substrate of the central patch however consists of two layers, modelled by shunt capacitance C (liquid crystal) and C_{sub} (TMM3 substrate) in series and can be estimated by the static parallel plate capacitor equation, expressed as

$$C = \varepsilon_0 \varepsilon \, {}^{A}/_{d} \tag{5.4}$$

and

$$C_{sub} = \varepsilon_0 \varepsilon_{sub} \, {}^{A}/_{d} \tag{5.5}$$

where for the liquid crystal cell, C and ε can take the values for the two liquid crystal extreme states, defined as perpendicular ($C_\perp$ with $\varepsilon_\perp$) and parallel ($C_\parallel$ with $\varepsilon_\parallel$) states, C_{sub} and ε_{sub} correspond to the TMM3 substrate and A and d present patch area and dielectric thickness respectively. The patch inductance (L) however can be determined according to the straight-line inductor approximation [126], [127]

$$L(nH) = 2 \times 10^{-4} l \left[ln \left(\frac{L}{W+t} \right) + 1.193 + 0.2235 \left(\frac{W+t}{L} \right) \right] K_g. \tag{5.6}$$

In this equation W, t and L (in μm) are the patch width, thickness and length respectively and correlation factor K_g is approximated as the following closed-form expression [127]

$$K_g = 0.57 - 0.145 \ln {}^{W}/_{h} \tag{5.7}$$

for $W/h > 0.05$ and h is the substrate thickness. The total insertion loss of the band-pass filter consists of contributions from ohmic, dielectric, liquid crystal losses and radiation losses. Due to the use of low loss dielectrics ($\tan\delta < 0.002$), and copper metallization, the dielectric, ohmic and radiation losses can be neglected. Therefore to a good approximation, the total insertion loss of the filter is the liquid crystal loss. This loss can be modelled by a parallel resistor; the resistance value R can be estimated as

$$R = 1/2\pi f C \tan\delta \tag{5.8}$$

where f is the resonant frequency, C is the liquid crystal capacitance and $\tan\delta$ is the liquid crystal loss tangent in perpendicular ($\tan\delta_{\perp}$) and parallel ($\tan\delta_{\parallel}$) states (Fig. 5.4). Given that the liquid crystal loss tangent at 3.0 GHz is not provided by the manufacturer, loss tangent values at 1 GHz and 19 GHz have been used for calculating R, using Table 4.1. By applying microstrip impedance formulas, using values presented in Table 5.2 and 5.3 and equations (5.1) to (5.8), the resulting component values results for K15 (5CB) and GT3-23001 liquid crystal samples are presented in Table 5.1.

Table 5.1. Lumped-element circuit estimated values. Calculated values for the equivalent circuit schematic, using two liquid crystal samples, K15 (standard) and the GT3-23001 (high performance).

SIR	Lumped values	K15 (5CB)	GT3-23001
Transmission lines Z_{TL}	L_{TL}	5.78 nH	5.78 nH
	C_{TL}	2.52 pF	2.52 pF
Patch Z_P	$L = L_3$	0.78 nH	0.78 nH
	$C_{\perp} = C_{3,\perp}$	9.43 pF	8.67 pF
	$C_{//} = C_{3,//}$	10.0 pF	11.38 pF
	$R_{\perp} = R_{3,\perp}$	984 Ω	2.27 kΩ
	$R_{//} = R_{3,//}$	928 Ω	6.40 kΩ
	C_{sub}	11.34 pF	11.34 pF

5.3.2 Simulation and convergence analysis

To investigate the lumped-element model, the equivalent circuit is simulated in ADS simulation software using the above values (Table 5.1). As mentioned previously, since the substrate under the patch is a multi-layer structure, a basic SIR single lumped element cannot be applied. For this reason, the central patch of length half of a wavelength (λ/2) is divided into $\left(\frac{\lambda}{2}\right)(2 \times (k-1))$ (for k = 1, 2, 3, …) segments and a convergence analysis is performed (Fig. 5.5).

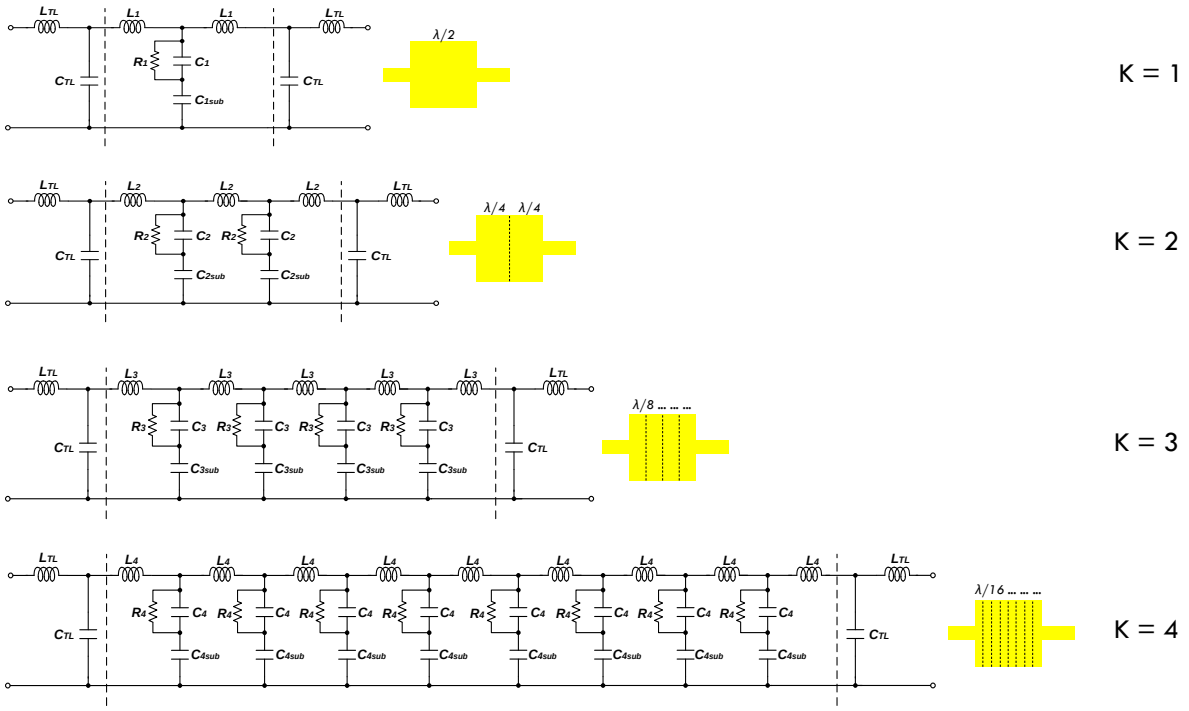

Figure 5.5. SIR patch divisions. Shows the single patch (λ/2), division by half (λ/4), quarter (λ/8), eight (λ/16) and its equivalent lumped-element circuit model.

The calculated values for the lumped-element circuit model of both K15 (5CB) from Sigma-Aldrich and GT3-23001 from Merck KGaA liquid crystal samples are presented in Table 5.2 and 5.3, respectively.

Table 5.2. Lumped-element circuit values–K15 (5CB). The RLC values for K15 liquid crystal sample from λ/2 to λ/16.

SIR	Lumped values		λ /2	λ /4	λ /8	λ /16
Transmission lines (Z_{TL})	L_{TL}		5.78 nH	5.78 nH	5.78 nH	5.78 nH
	C_{TL}		2.52 pF	2.52 pF	2.52 pF	2.52 pF
Patch (Z_P)	L		L_1 = 1.95 nH	L_2 = 1.30 nH	L_3 = 0.78 nH	L_4 = 0.44 nH
	C	$C_{\perp}$	$C_{1,\perp}$ = 37.74 pF	$C_{2,\perp}$ = 18.87 pF	$C_{3,\perp}$ = 9.43 pF	$C_{4,\perp}$ = 4.71pF
		$C_{/\!/}$	$C_{1,/\!/}$ = 40.20 pF	$C_{2,/\!/}$ = 20.10 pF	$C_{3,/\!/}$ = 10.0 pF	$C_{4,/\!/}$ = 5.0 pF
	R	$R_{\perp}$	$R_{1,\perp}$ = 246 Ω	$R_{2,\perp}$ = 492 Ω	$R_{3,\perp}$ = 984 Ω	$R_{4,\perp}$ = 1.97 kΩ
		$R_{/\!/}$	$R_{1,/\!/}$ = 232 Ω	$R_{2,/\!/}$ = 464 Ω	$R_{3,/\!/}$ = 928 Ω	$R_{4,/\!/}$ = 1.86 kΩ
	C_{sub}		C_{1sub} = 45.37 pF	C_{2sub} = 22.67 pF	C_{3sub} = 11.34 pF	C_{4sub} = 5.67 pF

Table 5.3. Lumped-element circuit values–GT3-23001. The RLC values for GT3-23001 liquid crystal sample from λ/2 to λ/16.

SIR	Lumped values		λ /2	λ /4	λ /8	λ /16
Transmission lines (Z_{TL})	L_{TL}		5.78 nH	5.78 nH	5.78 nH	5.78 nH
	C_{TL}		2.52 pF	2.52 pF	2.52 pF	2.52 pF
Patch (Z_P)	L		L_1 = 1.95 nH	L_2 = 1.30 nH	L_3 = 0.78 nH	L_4 = 0.44 nH
	C	$C_{\perp}$	$C_{1,\perp}$ = 34.69 pF	$C_{2,\perp}$ = 17.35 pF	$C_{3,\perp}$ = 8.67 pF	$C_{4,\perp}$ = 4.34 pF
		$C_{/\!/}$	$C_{1,/\!/}$ = 45.79 pF	$C_{2,/\!/}$ = 22.90 pF	$C_{3,/\!/}$ = 11.38 pF	$C_{4,/\!/}$ = 5.72 pF
	R	$R_{\perp}$	$R_{1,\perp}$ = 567 Ω	$R_{2,\perp}$ = 1.13 kΩ	$R_{3,\perp}$ = 2.27 kΩ	$R_{4,\perp}$ = 4.54 kΩ
		$R_{/\!/}$	$R_{1,/\!/}$ = 1.60 kΩ	$R_{2,/\!/}$ = 3.20 kΩ	$R_{3,/\!/}$ = 6.40 kΩ	$R_{4,/\!/}$ = 12.80 kΩ
	C_{sub}		C_{1sub} = 45.37 pF	C_{2sub} = 22.67 pF	C_{3sub} = 11.34 pF	C_{4sub} = 5.67 pF

The performance of the circuit with the above estimated values can be simulated in ADS software, and the resulting S-parameters are presented in (Fig. 5.6). For simplicity, only the perpendicular states of the both samples are presented in the plots. The performance of the frequency tuning is discussed further in Sec. 5.4.

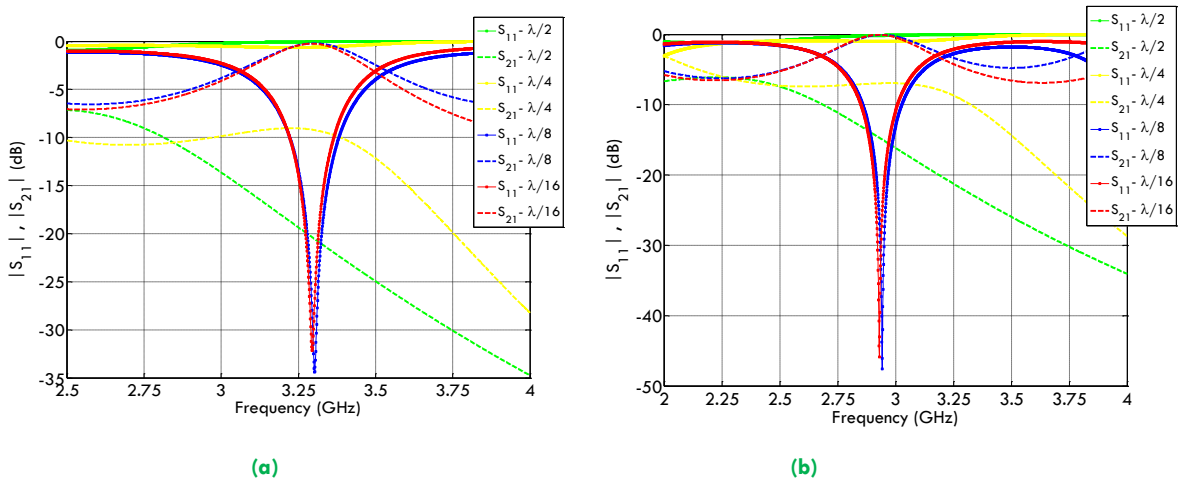

Figure 5.6. Lumped-element model simulation. A satisfactory convergence is achieved when the patch is divided in four segments, with λ/8 wavelength for each division, (a) K15 (5CB) and (b) GT3-23001.

Convergence analysis for the RLC circuit illustrates that when k=3 (λ/8 for each wavelength) the lumped-element circuit resonates at around 3.30 GHz for the K15 liquid crystal sample, and around 2.94 GHz for GT3-23001. However when the patch is divided into eight segments (λ/16) or even higher, the centre frequency remains roughly stable between 3.295–3.302 GHz and 2.942–2.930 GHz for K15 and GT3-23001 samples respectively. Since the λ/8 illustrates a good compromise between complexity and convergence of the results, this value was used as circuit model simulation (see Table 5.2 and 5.3).

5.4 Comparison and discussion

The lumped-element circuit model was also compared with the full-wave electromagnetic simulation. The SIR band-pass filter is simulated in CST Microwave Studio using the frequency-domain solver over a frequency range of 2.0–4.0 GHz. Given that liquid crystals are anisotropic materials, the corresponding layer under the patch was simulated using permittivity values in the extreme states (see Table 4.1), where $\varepsilon_{\perp}$ and $\varepsilon_{\parallel}$ corresponds to the relative permittivity for when V_b = 0 V and V_b >> 30 V respectively.

This approach neglects the fringing fields, which is an acceptable approximation for a thin substrate. The RLC circuit approach was also evaluated through prototype fabrication, using Rogers Duroid 5880 and TMM3 substrate and liquid crystal K15 (5CB) from Sigma-Aldrich and GT3-23001 from Merck KGaA (Sec. 4.3).

A comparison of the performance achieved from lumped-element circuit simulation, full-wave electromagnetic simulations and prototype measurements is shown in Fig. 5.7 and summarized in Table 5.4.

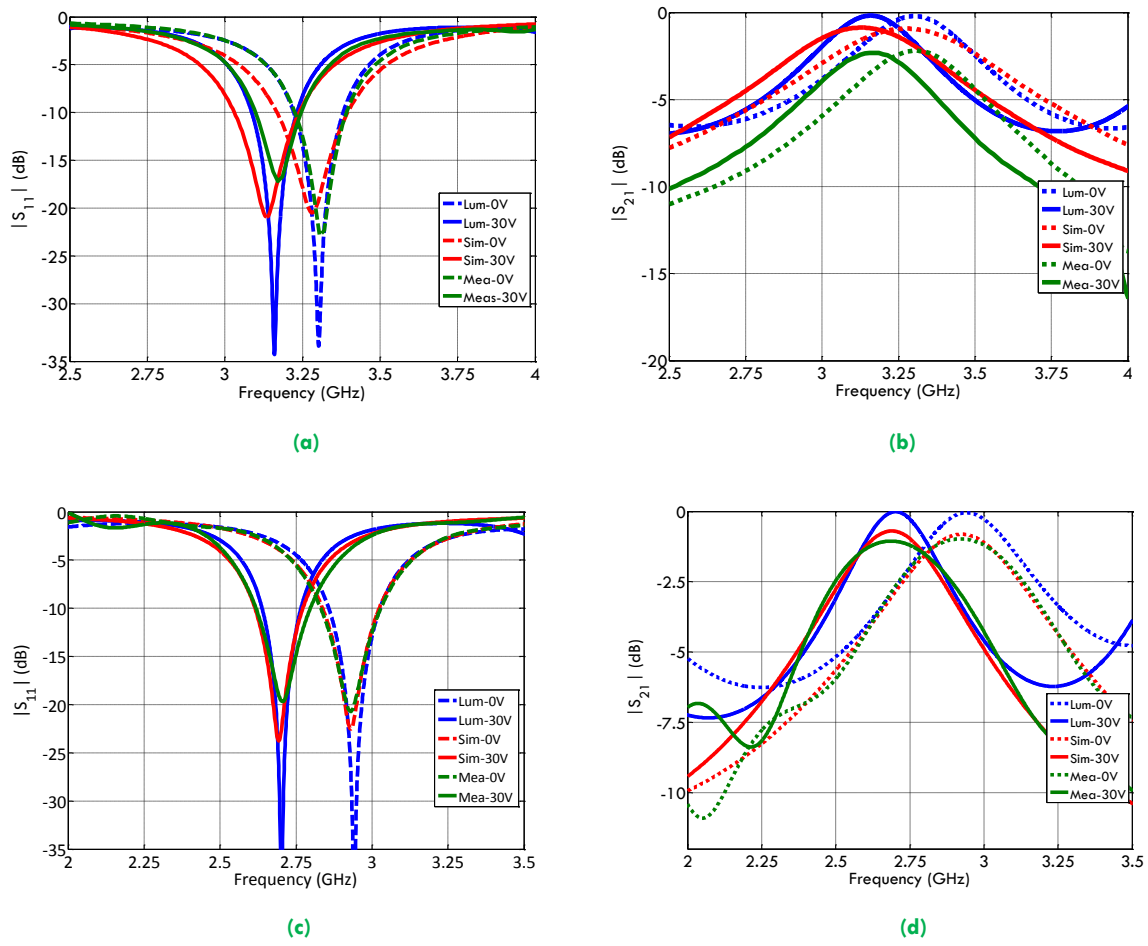

Figure 5.7. Comparison for lumped-element simulation, full-wave electromagnetic simulations and prototype measurements. (a) Reflection and (b) transmission coefficients for K15, (c) reflection and (d) transmission coefficients for GT3-23001.

Table 5.4. Results comparison. Lumped-element simulation, full-wave electromagnetic simulations and measurements for K15 and GT3-23001.

Samples	Models	$f_{\perp}$ (GHz)	$Loss_{\perp}$ (dB)	$f_{\parallel}$ (GHz)	$Loss_{\parallel}$ (dB)	TR%
K15 (5CB)	Lumped	3.30	0.20	3.16	0.18	4.1
	Simulation	3.28	1.0	3.14	1.0	4.4
	Measurement	3.30	2.2	3.17	2.2	4
GT3-23001	Lumped	2.94	0.04	2.70	0.01	8.4
	Simulation	2.93	0.8	2.69	0.7	8.5
	Measurement	2.93	1	2.70	1	8.2

The results achieved using lumped-element circuit simulation predicts an approximate frequency tuning range of 4.1% for K15, with reflection coefficients $|S_{11}|$ of around -30 dB, closely matching the tuning range of 4.4% computed in CST simulation and 4% achieved in prototype measurement. The agreement can also be confirmed with the GT3-23001, where 8.4% tuning is predicted with the lumped-element circuit simulation with a minimum reflection coefficients $|S_{11}|$ of around -35 dB, compared to 8.5% and 8.2% attained for simulation and prototype measurement respectively.

For both liquid crystal samples lower loss can be observed in the numerical models compared to the prototype measurement (discussed in Chapter 4). This is explained by underestimated losses in the lumped model and by unaccounted losses (e.g. connectors) in the measured data. To isolate the losses arising from the liquid crystal, the structure was measured with an unfilled cavity (ε_r = 1) instead of using liquid crystal. Comparing the measurements with and without liquid crystal provides an approximate magnitude of the liquid crystal losses to be around 0.4 ± 0.1 for K15 and 0.2 ± 0.1 dB for GT3-23001. These results are of course dependent on the device topology, material used and operating frequency.

The matching can be further improved in future by applying additional R (loss) to the circuit model, but the presented results illustrate the actual difference between these three approaches. Likewise the connector losses can as well be removed through de-embedding them in the measurement.

5.5 Conclusion and summary

In this chapter the lumped-element modelling of the previous S-band multi-layered tunable stepped-impedance resonator band-pass filter has been presented. The Good agreement between the results from this model, simulations and prototype measurements demonstrates the option of using the lumped element circuit model for rapid simulation of liquid crystal microwave devices. This equivalent circuit approach can provide faster simulation and lower computational cost in the optimization phase of more sophisticated designs.

Chapter 6

Tunable Liquid Crystal FSS Using Electric-*LC* Resonators

GROWING requirements in wireless communications have resulted in demand for tunable microwave devices in various applications, from body-centric communication antennas to filters and satellite communications. The electric-*LC* (*LC* circuit) resonator has been discussed as a building block for metamaterial absorbers, reflectors as well as modulators and polarizers. In this chapter a review of current electric-*LC* resonator usage is carried out, followed by a discussion of a modified electric-*LC* resonator, which illustrates fluid sensing ability and tunability using liquid crystal mixtures. It then demonstrates a tunable FSS at microwave frequency (C-band) using liquid crystal mixtures.

6.1 Introduction

This chapter provides an overview of electric-*LC* resonators (ELC) (electric-field-coupled inductor-capacitor) and their potential applications towards designing and developing metamaterial absorbers, reflectors, modulators and polarizers. Furthermore the chapter considers a modified design of the ELC resonator which incorporates a microfluidic channel in its central gap. This approach enables fluid sensing as demonstrated in both simulations and manufactured prototype measurements.

In regard to tunability, the ELC resonator is further modified as in [129] to include thin conductor strip bias lines at the top and bottom of the cell, continuously connecting every unit cell. Through using properties of liquid crystals in their nematic phase, frequency tunability at microwave frequency (C-band) is achieved. Simulated and measured results clearly demonstrate the potential design for novel tunable frequency selective surface using liquid crystal mixtures.

6.2 ELC resonators at microwave region

Electric-*LC* resonators, generally known as ELC resonators are resonant circuits, consisting of an inductor *L* and a capacitor *C*. When connected together, they perform as an electrical resonator, causing oscillation at the circuit's resonant frequency. ELC resonators consist of various structures and shapes that are implemented according to the choice of the application. These elements can be used for microwave, millimetre-wave and even terahertz applications (Fig. 6.1) [6].

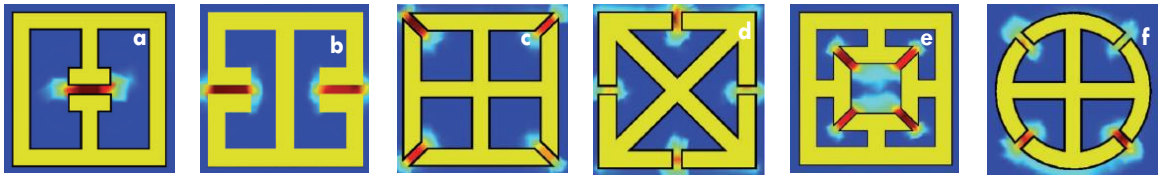

Figure 6.1. Different cell shape of ELC resonators. Illustrating different ELC cell shapes with its corresponding electric field [6].

The shape, size and dimension of the ELC cells vary depending on the frequency range and application. ELC resonators have been discussed in the literature for designing a range of microwave devices, from metamaterial absorbers and reflectors to modulators and polarizers. An example of these resonators as microwave frequency absorbers is reported in [130]. In this work the structure is composed of non-resonant and resonant structures, which can trap and absorb electromagnetic waves coming from all directions. The proposed design indicates an absorption rate of 99%. A comparable structure is proposed in [131], which also uses ELC resonators as a planar metamaterial absorber at microwave frequencies. The simulation and the fabricated prototype on the FR4 substrate demonstrate complete absorption (more than 99%) at around 10.35 GHz.

Apart from absorbers, ELC resonators have also been used as reflectors. An example is demonstrated in [132], where through electromagnetic resonant coupling with diodes, a controllable electromagnetic wave reflector/absorber for different polarizations is achieved. The on and off switching of the diodes in this work, enables the switching between total reflection and total absorption of an incident wave with given polarization, for frequencies in S-band. In a different structure, ELC resonators have been used for developing an electrically-controlled planar hybrid device, which enables radiation phase control. Alternatively this device could operate as a broadband modulator [133].

ELC resonators have as well been discussed at microwave frequencies for designing metamaterial polarizers. In [134], the idea of transmission polarizers realized by anisotropic metamaterials is illustrated. For this design one polarizer converts linear-polarized waves to circular-polarized waves, while the other converts linear-polarized waves from one polarization to its cross polarization. The simulation and experimental results validate the functionality of the proposed polarizers. A comparable design is proposed [135] for a polarization modulation scheme of electromagnetic waves through reflection of a tunable metamaterial reflector/absorber at a microwave frequency range of 2-4 GHz.

One recent example of a planar array of microwave ELC resonators with broadband tunability is presented in [129]. In this design, through applying DC bias voltage to the embedded varactors, a wide tuning range of around 32% (2.67 to 3.52 GHz) is achieved. A similar example of tunable ELC resonators operating at S-band is proposed in [136]. In this designed structure, tunability is attained through changing permittivity in a continuous flow in a channel that interacts with the metasurfaces. Numerical simulations and experimental results demonstrate application of microwave ELC resonators for chemical processing.

6.3 Liquid crystal tunable ELC resonator

Given that filling the complete structure with liquid crystal would be very expensive and necessary to achieve tuning, a channel was required in the centre between the capacitive gaps. Element "a" from the above figure (Fig. 6.1) was selected to be the most promising option for this design. In the preliminary stage of the design, the original ELC resonator cell was designed, optimized and simulated in CST using periodic boundary conditions (Floquet port). This cell was designed to be 10 × 10 mm (length (*L*) × width (*W*)). In order to achieve a frequency response in S-band, the central gap (*g*) was designed to be around 0.15 mm in width, corresponding to a resonant frequency of around S-band (3.36 GHz), Fig 6.2.

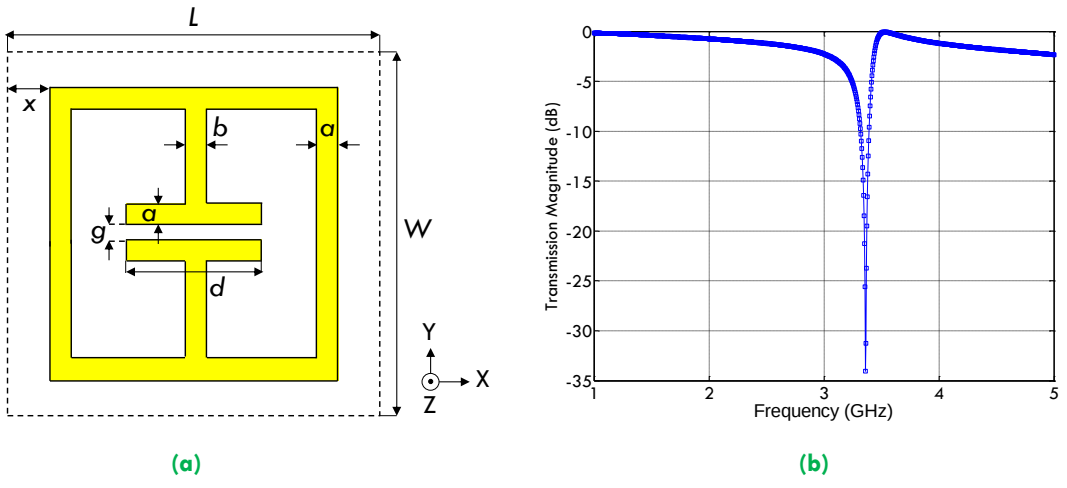

Figure 6.2. Original ELC resonator cell. (a) Original single resonator unit cell, with the boundaries indicated by dotted lines, (b) simulated frequency response of the cell at 3.36 GHz.

Other dimensions of the resonator as shown in Fig. 6.2 are as follows: a = 0.5 mm, b = 0.5 mm, d = 5 mm and x = 1 mm. This resonator was simulated on a Rogers Duroid 6002 substrate (ε_r = 2.94, $tan\ \delta$ = 0.0012, h_s = 3.05 mm), because of its low relative permittivity and low loss tangent. Some of the above dimensions (e.g. a, b and x) were based on the previously designed cell by our group. The objective of this project was to further modify the cell in order to make it tunable.

Moreover in the next step, to develop a microfluidic channel in the central capacitive gap, the gap was extended to both sides, causing division in the unit cell. This division not only provides a continuous channel in the structure, but also enables two divisions in the structure, which assists in the future DC biasing of the cell (see Fig. 6.6). The designed cell with a microfluidic channel and its corresponding full-wave simulation are presented in Fig. 6.3.

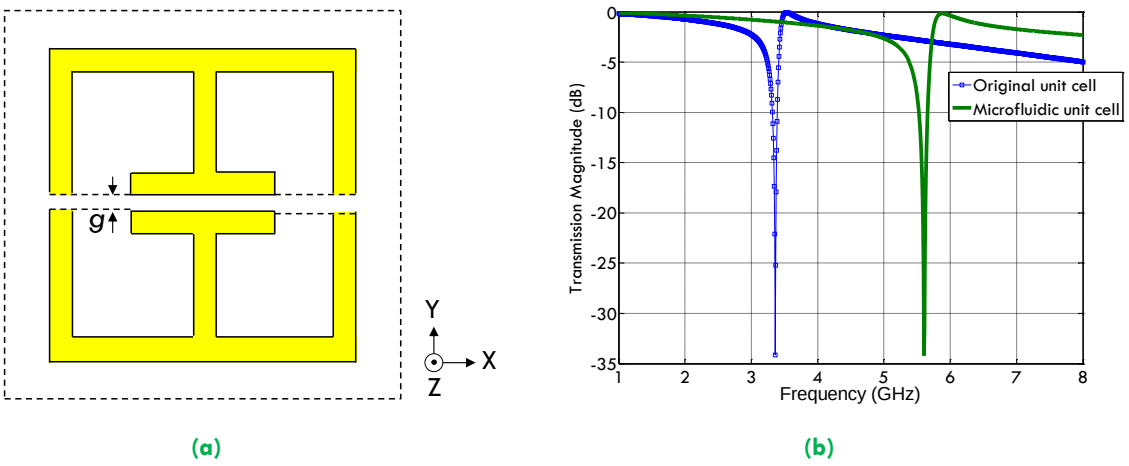

Figure 6.3. ELC resonator cell with microfluidic channel. (a) Single resonator unit cell, (b) comparison of simulated frequency response of the original and microfluidic cell.

Increasing the capacitive gaps on both sides from 0 to 0.15 mm shifts the central resonant frequency from 3.36 to 5.60 GHz (S-band to C-band). To test the tuning performance of ELC resonator, the channel was filled with liquid crystal mixture (GT3-23001) (see Table 4.1 for electrical properties). In the initial test simulations, in order to use a lower amount of liquid, only the central capacitive gap (0.15 mm) with depth of 0.2 mm in the substrate was filled with liquid crystal mixture, Fig. 6.4 (a).

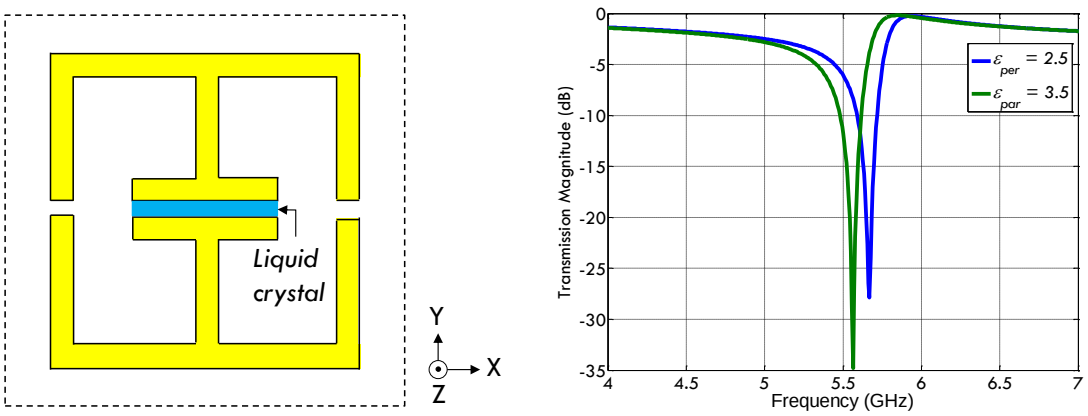

(a) (b)

Figure 6.4. Microfluidic channel filled with liquid crystal. (a) Single resonator unit cell filled with GT3-23001 mixture, (b) simulated tuning frequency response.

By changing the relative permittivity of the mixture and its corresponding loss tangent in the simulation, the frequency continuously shifts from 5.67 GHz for when $\varepsilon_{\perp}$ = 2.5 to 5.56 GHz for when $\varepsilon_{\parallel}$ = 3.5, corresponding to a tuning range (τR) and tuning (τ) of around 2% (110 MHz), Fig. 6.4. (b). In order to increase the tuning range of the resonator, the microfluidic channel was expanded through the whole cell.

Having all three capacitive gaps filled with liquid crystal (GT3-23001) not only increases the tuning range, but also simplifies the fabrication procedure, since inserting the liquid crystal just in the narrow channels is impractical. The liquid crystal mixture was moreover expanded to cover the two copper electrodes on either sides of the centre capacitive gap (s = 1.15 mm) (see Fig. 6.5 (a)) enabling higher tuning performance, Fig. 6.5 (b). Since outside the channel region (highlighted in blue) the electric fields are very low, with a good approximation, the optimal value of s was defined as 1.15 mm.

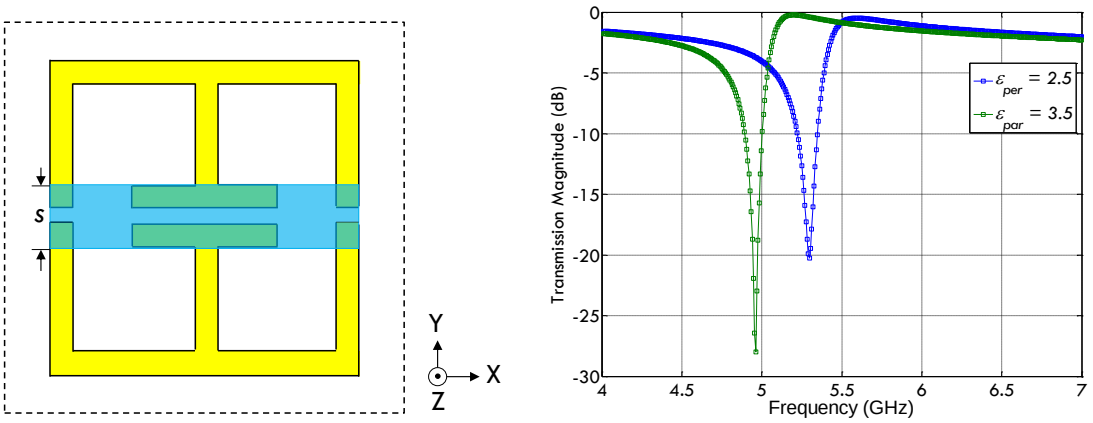

Figure 6.5. Microfluidic gaps filled with liquid crystal. (a) Single resonator unit cell channel, filled with GT3-23001 mixture, (b) simulated tuning frequency response.

Through extending the liquid crystal and similarly changing the relative permittivity in the full-wave electromagnetic simulation (with periodic boundary conditions), the resonant frequency of the ELC resonator varies from 5.29 GHz to 4.96 GHz, with reflection coefficients of around -20.2 dB and -28 dB respectively, demonstrating improvement in the tuning range by more than three times, from the previous tuning range (τR) of 2% to 6.44% (330 MHz). Since in practice we need to apply a bias voltage, additional thin conductor strip bias lines (x = 1mm by y = 0.3 mm) are added to both the top and bottom of the cell, continuously connecting every unit cell, Fig. 6.6 (a) [129].

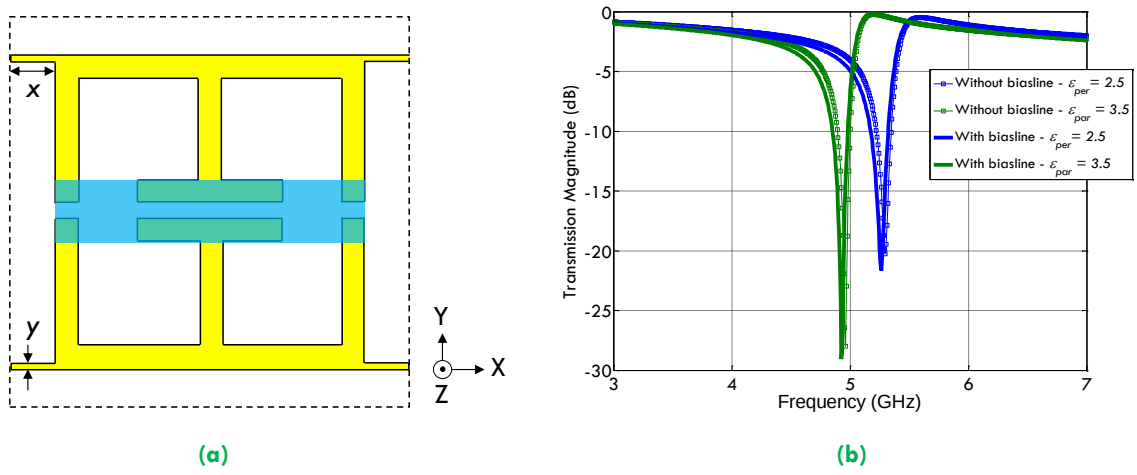

Figure 6.6. ELC resonator with bias lines. (a) Applied thin bias lines to resonator unit cell, (b) simulated tuning frequency response.

As illustrated in Fig. 6.6 (b), due to their perpendicular orientation with respect to the operation polarization, and the fact that these bias lines are extremely thin (only 0.3 mm) they have no significant effect on the resonant frequency. In this case when the ELC resonator is simulated in the liquid crystal perpendicular state, the resonant frequency is $f_{\perp}$ = 4.92 GHz, with reflection coefficients of around -21.6 dB and when simulated in the parallel state, the resonant frequency is $f_{\parallel}$ = 5.26 GHz with reflection coefficients of -29 dB, yielding an overall tuning range (τR) of around 6.5%.

Eventually as in [137], a thinner width (*b*) is used in the central capacitor, which through increasing the central inductance, shifts the resonant frequency to even lower frequency and contributes to miniaturization of the design. Fig. 6.7 and Table 6.1 both illustrate the dimensions of the final ELC resonator unit cell.

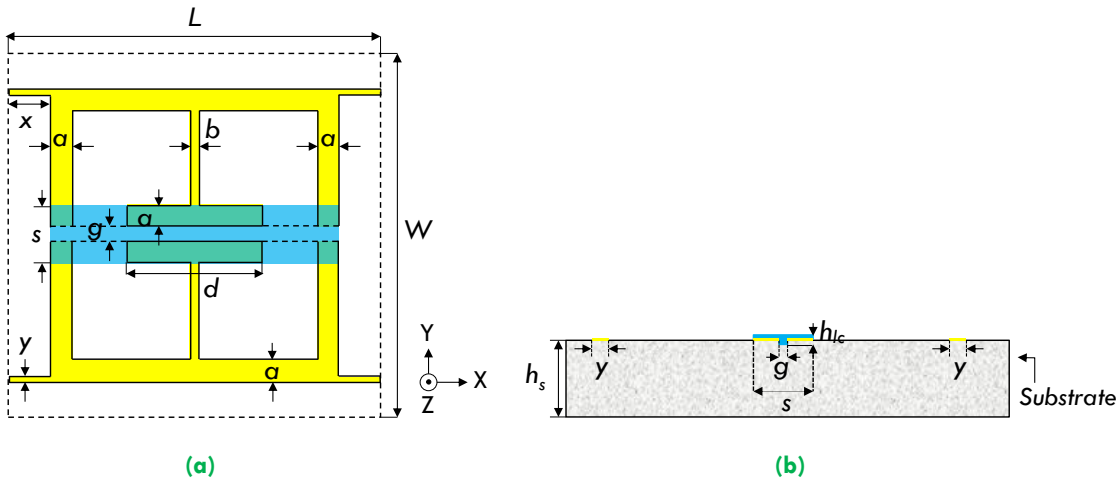

Figure 6.7. Modified ELC resonator unit cell. (a) Final modified resonator cell with liquid crystal in a micro-fluidic channel, (b) cross-section view of the single cell.

Table 6.1. Final ELC resonator unit cell. The table below provides all dimensions of the final designed cell.

L	*W*	*a*	*b*	*d*	*g*	*s*	*x*	*y*	h_s	h_{lc}
10 mm	10 mm	0.5 mm	0.2 mm	5 mm	0.2 mm	1.15 mm	1 mm	0.3 mm	3.05 mm	0.4 mm

6.4 Full-wave simulation

After finalizing the design of a generic ELC resonator unit cell, the next step was modelling and simulating the final structure in a practical configuration. Given that for fabrication, the liquid needs to be placed in a sealed environment to avoid any leakage, two different approaches are considered. The first approach is using fluid tube channels, where in this case the liquid samples are pumped in the tube which runs along the capacitive gaps, and in the second approach, liquid crystal is poured between the capacitive gaps and sealed using a cover lid. In following both approaches are discussed and simulated.

6.4.1 Fluid tube approach

In the first full-wave electromagnetic simulation, the ELC resonator was modelled with an array of microfluidic tubes running through its central channel, Fig. 6.8.

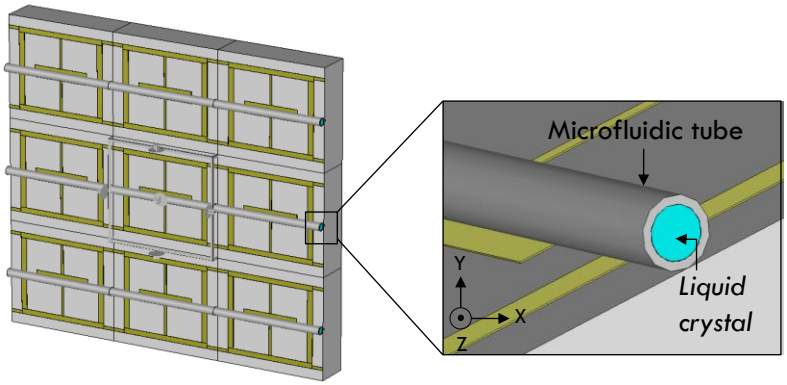

Figure 6.8. Microfluidic tube channel array. Array of ELC resonator combined with microfluidic tube channel in the centre, filled with liquid crystal mixture.

This channel was modelled with standard microfluidic Teflon (PTFE) tube (ε_r = 2.1, $tan\ \delta$ = 0.0002), with outer radius of r_{out} = 0.4 mm and inner radius of r_{in} = 0.3 mm (see Fig. 6.9 (a)) and was filled with liquid crystal mixture. Similar to the previous case, an infinite array of ELC resonators was simulated in CST over a frequency range of 4--6 GHz, using periodic boundary conditions. The results for the both perpendicular and parallel state are presented in Fig. 6.9 (b).

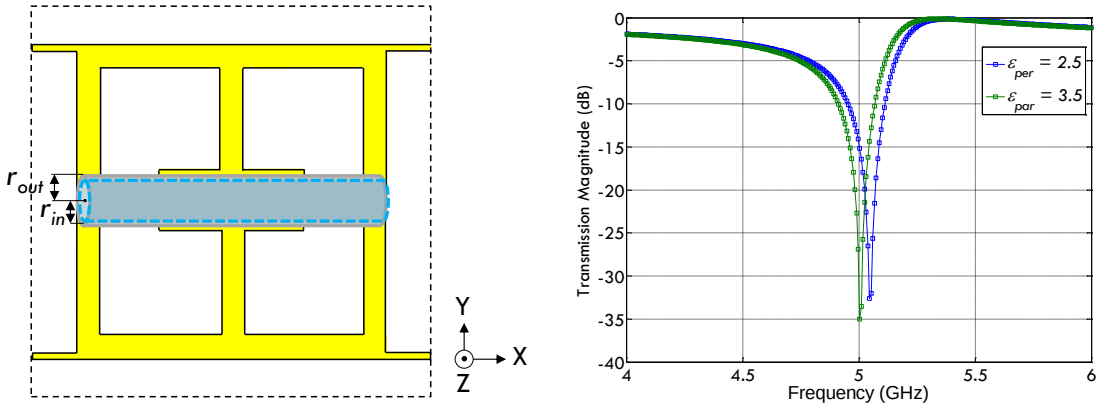

(a) (b)

Figure 6.9. Microfluidic tube channel. (a) Array of ELC resonator combined with microfluidic tube channel in the centre, filled with liquid crystal mixture, (b) simulated tuning frequency response.

From the figure, it can be observed that when the liquid crystal mixture (GT3-23001) is simulated in the perpendicular state (ε_r = 2.1, $tan\ \delta$ = 0.0143, i.e. V = 0 V), the resonant frequency of the ELC resonator array is 5.05 GHz. However by changing the liquid crystal molecular state to parallel (ε_r = 3.5, $tan\ \delta$ = 0.0038, i.e. $V >> V_{th}$) the centre frequency shifts to 5.0 GHz, illustrating a tuning range (τR) of ~1%. The results indicate that low tuning is observed owing to weak interaction between fields in the capacitors and the liquid. This clearly indicates that Teflon tube will not be an ideal method for validation at microwave frequency.

6.4.2 Top cover approach

Since in the above approach (microfluidic tube) very low tuning was observed, the liquid crystal was then placed directly inside the channel and on top of the capacitive gaps. A top cover smooths the liquid out and the high viscosity of the liquid crystal means there is minimal leakage, Fig. 6.10.

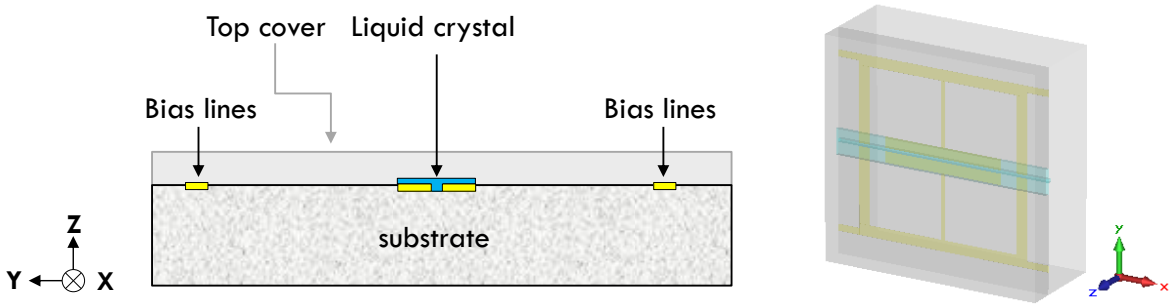

Figure 6.10. Sealed tunable ELC resonator unit cell. Cut and perspective view of the ELC resonator, which consists of a microfluidic channel filled with liquid crystal and sealed with a top lid.

For validation of the tuning performance, the final modified structure was simulated using GT3-23001 high performance liquid crystal mixture (see Table 4.1) and Pyrex glass (ε_r = 4.82, $tan\ \delta$ = 0.0054) for the top lid, due to its low loss and transparent appearance. The full-wave electromagnetic simulations indicate that by varying the effective relative permittivity of the liquid crystal mixture from $\varepsilon_{\perp}$= 2.5 to $\varepsilon_{||}$ = 3.3, the resonant frequency of the ELC resonator array shifts from 4.61 to 4.35 GHz (260 MHz). This is equivalent to a frequency shift of 6% relative to the lower frequency, as shown in Fig. 6.11.

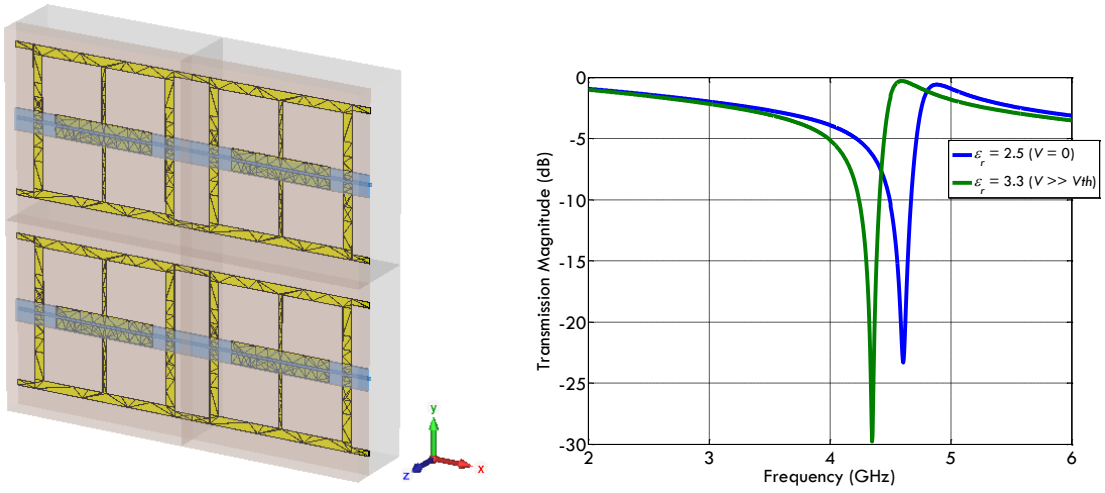

Figure 6.11. Modified tunable ELC resonator. (a) Mesh view of the tunable ELC resonator, (b) simulated tuning response.

6.4.3 Parametric study and analysis

The next stage of the simulation required identifying important parametric values which could have an effect in the final fabrication. In this ELC resonator, four geometrical parameters have significant impact on the final tuning performance and the resonant frequency. These are (Fig 6.7): capacitor length (d), capacitor width (b), substrate material (ε_r , $tan\ \delta$) and liquid crystal mixture anisotropic properties ($\varepsilon_\perp$, tan $\delta\perp$ and $\varepsilon_\parallel$, tan $\delta\parallel$), which are studied and discussed below.

An initial study was carried out on the central capacitor length (d). In this investigation, a parameter sweep was carried out from 1 mm to 6.5 mm, over a frequency range of 2 to 8 GHz with the CST accuracy parameter set to (hexahedral meshing) 10^{-12}. The results from Table 6.2 and Fig. 6.12 indicate that as the capacitor length decreases the resonant frequency shifts to a higher frequency. The frequency tuning (τ) for this tunable ELC resonator, has a minimum value of 5.34% and a maximum value of 6.19%. According to length d sensitivity analysis, given that the desired centre frequency was at 4.5 GHz (due to experimental setup), the capacitor length was chosen to be everywhere between 4.28 to 5.22 mm, with tuning of 5.82 to 5.64% (see Table 6.2).

Table 6.2. Capacitor length (mm). A parameter sweep was performed on the central capacitor length (1 – 6.5 mm) over a frequency range of 2 to 8 GHz for standard RT/duroid 6002 substrate.

Cap Length (mm)	f_h (GHz)	f_l (GHz)	Tuning%
6.5	3.944	3.744	5.34
6.18	3.996	3.792	5.37
5.86	4.024	3.812	5.56
5.54	4.22	3.996	5.60
5.22	4.264	4.036	5.64
4.92	4.368	4.132	5.71
4.60	4.454	4.208	5.84
4.28	4.504	4.256	5.82
3.96	4.612	4.356	5.87
3.64	4.736	4.464	6.09
3.34	4.808	4.532	6.09
3.02	5.008	4.72	6.10
2.71	5.104	4.808	6.15
2.39	5.256	4.952	6.13
2.07	5.468	5.152	6.13
1.76	5.62	5.292	6.19
1.44	5.856	5.524	6.01
1	6.288	5.948	5.71

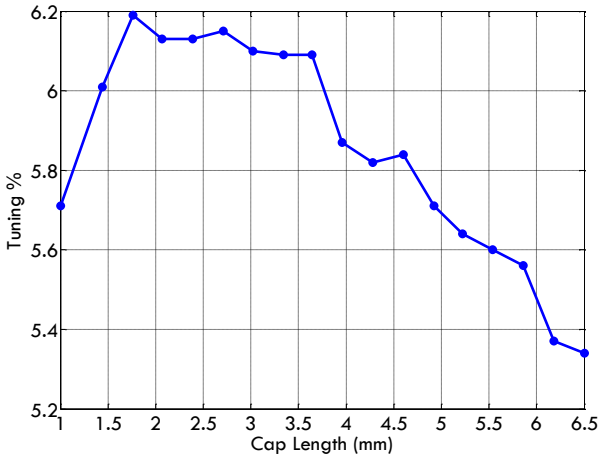

Figure 6.12. Capacitor length vs. tuning. The plot illustrates the tuning performance in percentage as capacitor length varies in mm.

Apart from the central capacitor length, another important factor considered was the central capacitive width (*b*). To study this value, a parametric analysis was carried out from 2 mm to 0.1 mm, again over a frequency range of 2 to 8 GHz. The study analysis indicates that as the capacitor width (*b*) decreases, the resonant frequency also decreases to a lower frequency, but the tuning (τ) of ELC resonator remains approximately constant between 5. 5% to 6% (see Table 6.3 and Fig. 6.13). As a result, in order to stabilize the centre frequency at around 4.5 GHz, the capacitor width was chosen to be between 0.31 to 0.1 mm, with constant tuning of 5.95% and transmission magnitude of ~–25 dB (see Table 6.3).

Table 6.3. Capacitor width (mm). A parameter sweep was performed on the central capacitor width (0.1–2 mm) over a frequency range of 2 to 8 GHz for standard RT/duroid 6002 substrate.

Cap Width (mm)	f_h (GHz)	f_l (GHz)	Tuning%	Trans Mag in dB
2	5.865	5.557	5.54	-20 to -15
1.78	5.746	5.438	5.66	-22 to -18
1.56	5.641	5.34	5.63	-22 to -18
1.36	5.536	5.235	5.74	-22 to -18
1.14	5.417	5.123	5.73	-25 to -20
0.94	5.27	4.983	5.75	-25 to -20
0.72	5.13	4.85	5.77	-30 to -20
0.52	4.962	4.682	5.98	-30 to -20
0.31	4.731	4.465	5.95	-30 to -20
0.1	4.486	4.234	5.95	-30 to -20

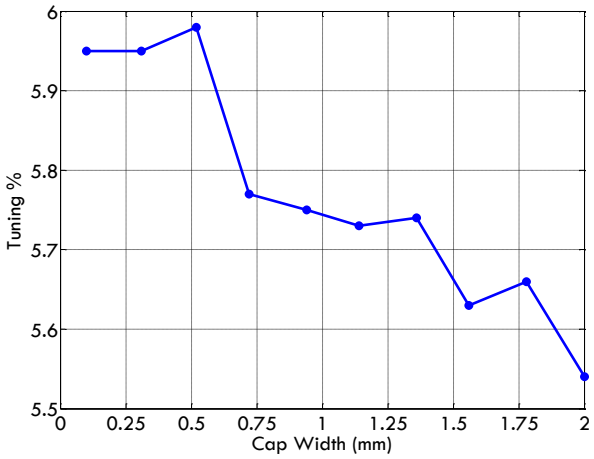

Figure 6.13. Capacitor width vs. tuning. The plot illustrates the tuning performance in percentage as capacitor width varies in mm.

Other important factors which greatly affect frequency deviation and as a result tuning variation is the substrate material (ε_r , $tan\ \delta$) and the liquid crystal mixture ($\varepsilon_\perp$, $tan\ \delta_\perp$ and $\varepsilon_\parallel$, $tan\ \delta_\parallel$). As discussed previously (Chap. 3 and Chap. 4), to achieve maximum tuning, the substrate permittivities are required to be similar to the liquid crystal permittivity.

For this simulation, two commonly available substrates from Rogers are used: 6002 and 5880 with relative permittivities of 2.94 and 2.20 respectively. In order to validate the tuning performance of this ELC resonator, three different liquid crystal mixtures (K15 (standard), BL037 and GT3-23001) are tested. In these simulations, apart from the substrate, the top cover was varied as well in order to validate the tuning performance. To be able to clearly see inside the structure during the liquid crystal filling process, three transparent materials were considered for the top cover: Pyrex (ε_r = 4.82 , $tan\ \delta$ = 0.0054) , polydimethylsiloxane (PDMS) (ε_r = 2.8, $tan\ \delta$ = 0.002) and polycarbonate (ε_r = 2.77 , $tan\ \delta$ = 0.0055). The choice of top covers was based mainly on material availability, price range, their chemical reaction and transparency.

Table 6.4. Tuning range performance for sealed ELC resonator. Various materials were tested for frequency tuning performance when the cover is placed (see Table 3.2 and 4.1 for liquid crystal electrical properties).

Substrate	Top cover	Relative permittivity (ε_r)	Loss tangent (tan δ)	Liquid crystal samples		
				GT3-23001	BL037	K15
RT/Duroid 6002 (h_s = 3.048)	Pyrex	4.82	0.0054	5.97% (at -30 dB)	2.01% (at ~ -17 dB)	1.31% (at ~ -20 dB)
	PDMS	2.8	0.002	5.91% (at -30 dB)	2.14% (at ~ -17 dB)	1.37% (at ~ -20 dB)
	Polycarbonate	2.77	0.0055	6.05% (at -30 dB)	2.14% (at ~ -17 dB)	1.36% (at ~ -20 dB)
RT/Duroid 5880 (h_s = 3.175)	Pyrex	4.82	0.0054	6.48% (at -30 dB)	1.08% (at ~ -17 dB)	0.81% (at ~ -20 dB)
	PDMS	2.8	0.002	4.51% (at -30 dB)	1.08% (at ~ -17 dB)	0.10% (at ~ -20 dB)
	Polycarbonate	2.77	0.0055	3.88% (at -30 dB)	3.01% (at ~ -17 dB)	2.74% (at ~ -20 dB)

Table 6.4 clearly illustrates that as the dielectric anisotropy of the liquid crystal increases from 0.18 for K15 to 0.80 for GT3-23001, the tuning increases from approximately 1.3% to 6% for 6002 substrate and from approximately 0.8% to 6.5% for 5880 substrate. This table indicates that using 6002 as the substrate, the frequency tuning (τ) remains approximately stable between 5.97–6.0% for GT3-23001, 2-2.14% for BL037 and 1.31-1.37% for K15 (5CB) depending on the high and low centre frequency.

In summary in order to design an optimum tunable ELC resonator with operating frequency of around S-band, which could be measured using in the available waveguide (discussed in Sec. 6.7), the structure was designed with capacitor length (d) of 5 mm, width (b) of 0.2 mm and gap (g) size of 0.2 mm. Furthermore to increase the tuning performance to around 6%, the structure was validated with GT3-23001 liquid crystal mixture.

6.5 Lumped-element model

The behaviour of a single ELC resonator cell, where the electromagnetic field is parallel to the ELC plane can be modelled by a lumped-element model. In normal operation, an oscillating electric field polarized perpendicularly to the gap induces a current flow in the two symmetric loops. Similar to an electric *LC* circuit, the structure becomes resonant when the electric energy in the capacitor is equal to the magnetic energy stored in the inductor.

Given that the current on both sides of the original ELC resonator are equal, the cell can be approximated by inductors and capacitors in the form of an *LC* resonant circuit. In this circuit the inductive loop can be modelled by inductor L_1 and the capacitive gap in the centre can be modelled by inductor L in series with capacitor C_g, Fig. 6.14.

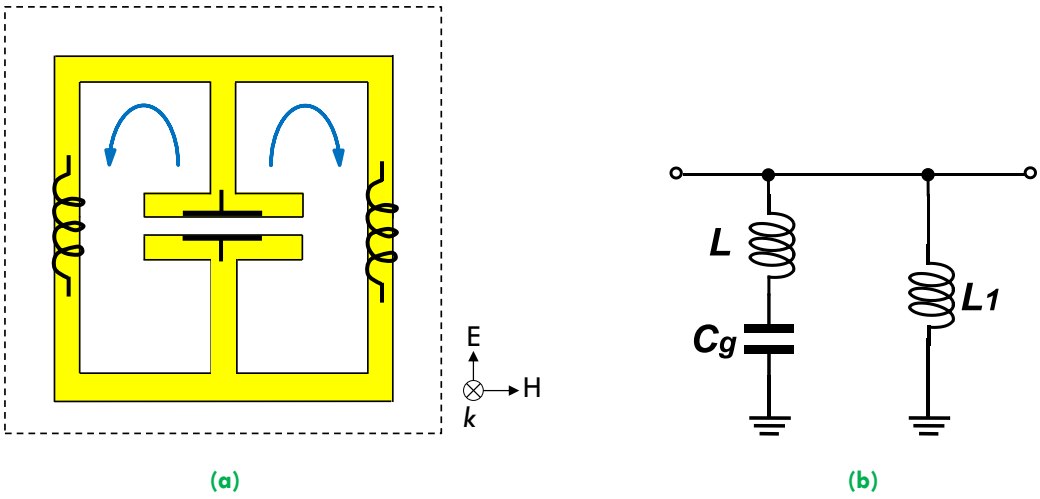

Figure 6.14. Original ELC resonator lumped-element model. (a) The ELC resonator is modelled by conductive loop and capacitive gap, (b) equivalent circuit.

However the lumped-element circuit model for the modified tunable ELC resonator is expressed differently. In this case the inductive loops can be modelled by an inductor L_1 in series with a capacitor C_1 and similar to the previous case, the capacitive gap can be modelled by an inductor L in series with a capacitor C_g, Fig. 6.15.

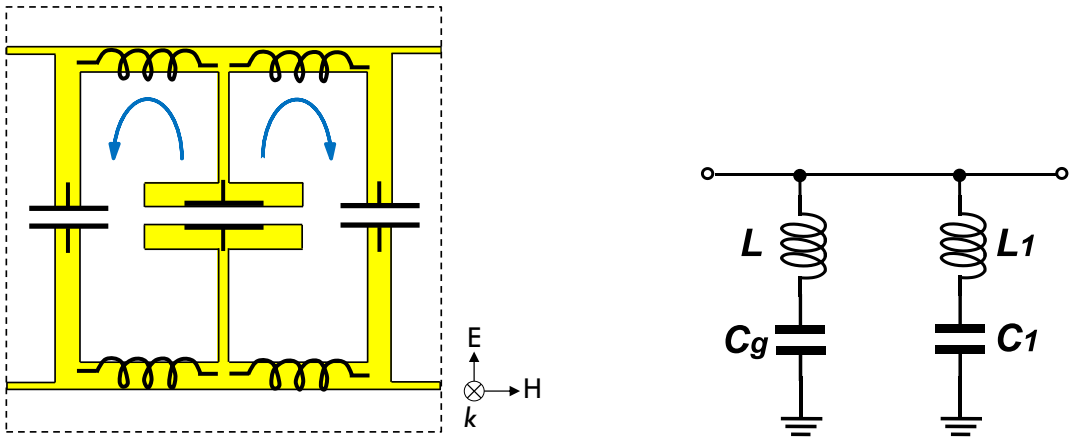

Figure 6.15. Modified tunable ELC resonator lumped-element model. (a) The ELC resonator modelled by conductive loop and capacitive gap, (b) equivalent circuit.

To further study the designed circuit, the proposed models for both the original and the modified cell have been simulated in the ADS simulation software over a frequency range of 1 to 8 GHz. The comparison between the full-wave simulation and the lumped-element model simulation for both original and modified cell are proposed in Fig. 6.16 based on extracted circuit parameters *C* and *L*.

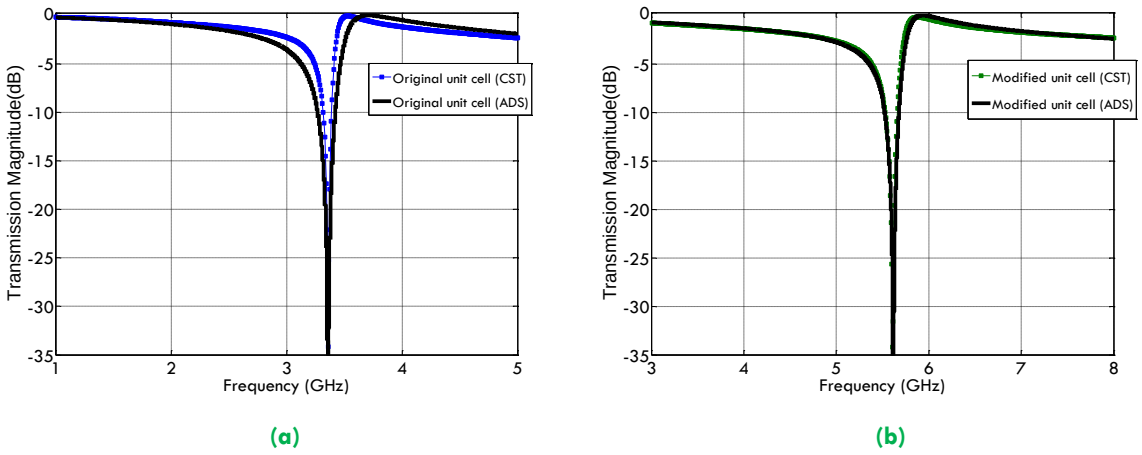

Figure 6.16. Lumped-element and full-wave model comparison. (a) Original uni cell, (b) modified uni cell.

Taking into account the substrate as RT/Duroid 6002, the following values were extracted: for the original cell, L= 68 nH, C_g= 0.033 pF and L_1= 20 nH, corresponding to a resonant frequency of 3.36 GHz and transmission magnitude of -35 dB (for both lumped-element and full-wave simulations) and for the modified cell, L= 68 nH, C_g=

0.0118 pF, L_1= 0.004 nH and C_1= 0.1 pF, corresponding to a resonant frequency of 5.60 GHz and transmission magnitude of around -35 dB for both simulations.

6.6 Prototype fabrication

The fabrication prototype of the ELC resonator was achieved through collaboration with Australian National Fabrication Facility (ANFF), Ian Wark Research Institute at University of South Australia and Macquarie University in Sydney. The fabrication of the ELC resonator can be divided into three individual stages: *1- developing ELC resonator array*, *2- creating thin channel* and *3- fabricating the top cover (lid)*. In the paragraphs below each of these three steps and their fabrication procedures are discussed individually.

6.6.1 Developing ELC resonator array

To develop the designed pattern on the substrate and develop the ELC array, three steps were considered sequentially: *masking*, *lithography/exposing* and ultimately *metal etching*. In the first step the pattern was redrawn using AutoCAD software [138] and printed as lithography masks, Fig. 6.17. This step is commonly known as *lithography masking* or simply *masking*.

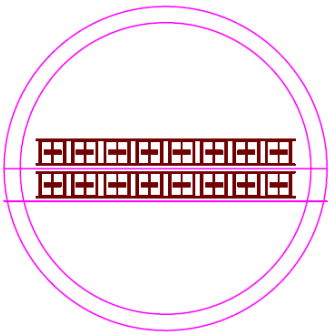

Figure 6.17. Masking pattern. The exported image illustrates the designed AutoCAD ELC 8 by 2 array used for lithography masking.

The second stage required exposing the patterns on the substrates. For this purpose the pre-cut RT/Duroid substrates were washed in a Soniclean machine using

purified water for around 5 minutes (Fig. 6.18 (a)). This cleaning helps to remove unwanted oil or chemicals from the copper surface. The cleaned substrates were then baked for 1 hour at 95 °C, Fig. 6.18 (b).

(a) (b)

Figure 6.18. Cleaning and baking. (a) Washing the substrates using purified waster, (b) baking the substrate in the oven at 95 °C in order to remove all water molecules from the surface.

The next step requires *lithography and exposing*. In this step, the substrates were placed in the lithography machine and were aligned with the mask and exposed to 300 mJ/cm^2 of UV light (Fig. 6.19). The coated substrates were then baked for 2 minutes at 65 °C and then at 95 °C for 6 minutes before being rested at room temperature (20 °C) for 10 minutes for cooling to take place. Finally to clean the photoresist and stop the developer, the layers were washed with developer (SU-08) and then isopropanol $(CH_3)_2CHOH$.

(a) (b)

Figure 6.19. Aligning and lithography. (a) Aligning the mask on the glass, (b) aligned substrate and mask under the lithography machine.

Ultimately the exposed substrate is placed inside a beaker filled with 30% of iron (III) chloride ($FeCl_3$) mixed with 70% of purified water (H_2O) for around 7 minutes to dissolve the copper.

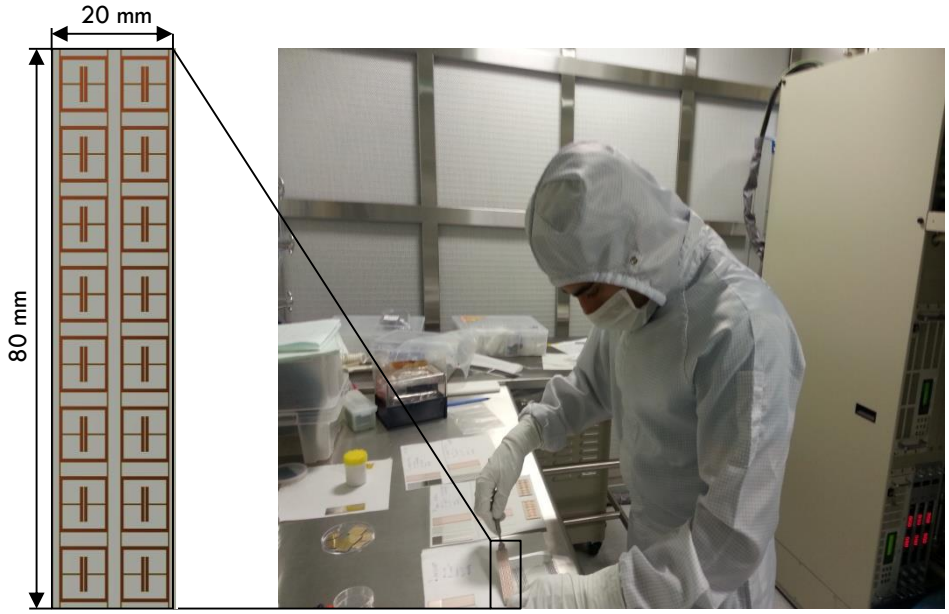

Figure 6.20. ELC resonator prototype. The final fabricated ELC resonators inside the clean room. This design has 8 by 2 arrays of cell with a thickness of h_s = 3 mm.

Fig. 6.20 shows the final tunable ELC resonator prototype. This structure exemplifies a frequency selective surface consisting of an 8 by 2 array of cells, made on Rogers Duroid 6002 substrate (ε_r = 2.94, tan δ = 0.0012, h_s = 3.05 mm), which its demonstrated in Section 6.8 for sensing and 6.9 as tunable FSS.

6.6.2 Creating the thin channel

After finalizing the design, the next stage required milling a thin and narrow channel inside the substrate between the capacitive gaps. This process was achieved through collaboration with Optofab, based at Macquarie University in Sydney.

Given that the channel in this case was only 0.15 x 0.2 mm, laser milling was used for this fabrication. For this process, a 4th Harmonic (266 nm) Nd:YAG laser machine was used, which consisted of Aerotech XYZ stages, spinning (trepanning) optics and

a 5x objective lens. The machine was set to a pulse frequency of 750 Hz and an average power of 30mW. In this process a trench is machined inside the Duroid using the laser, creating a 0.15 mm x 0.2 mm channel, with ± 5µm accuracy (microscope at 50x) inside the substrate for the liquid crystal mixture, Fig. 6.21.

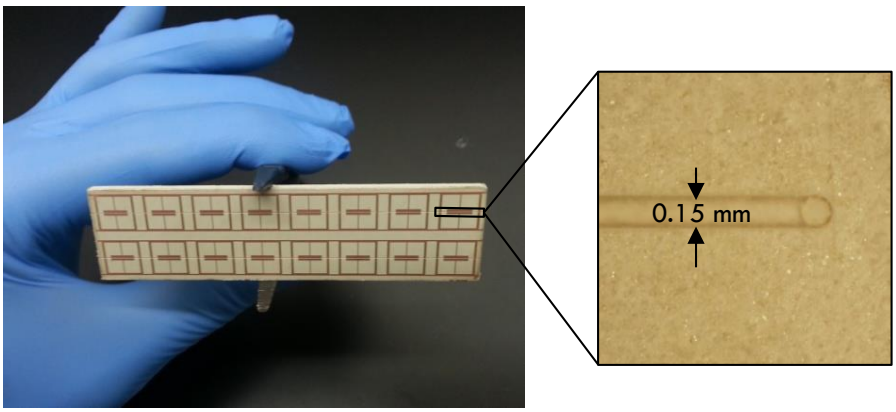

Figure 6.21. Milled channel. The final fabricated structure, consisting of a thin trench (0.15 mm by 0.2 mm), milled inside the Duroid substrate. Right image taken by scanning electron microscope.

6.6.3 Fabrication of top cover

The final stage requires fabrication of the top cover or lid. As discussed previously (see Table 6.4) two transparent materials were designated for this purpose: PDMS and Pyrex. In below the fabrication process of each material is discussed individually.

6.6.4 Developing PDMS cover

In order to develop the PDMS cover these steps were required: *pretreating*, *coating*, *soft baking*, *exposing*, *post expose baking*, *developing* and finally *removing*.

Before developing the PDMS, the designed channel patterns were drawn on AutoCAD and were printed as a *lithography masks*. These printed masks were then used for creating the channels inside the PDMS.

The first step required *preheating* the wafers (radius = 5 cm) in the electronic clean room. In this step, the wafers are heated to 200 °C for 5 minutes (Fig. 6.22. (a)). This pretreating helps to remove water from the wafer surface. After pretreat completion, the wafers are rested at room temperature (20 °C) for about 2 minutes for cooling to take place.

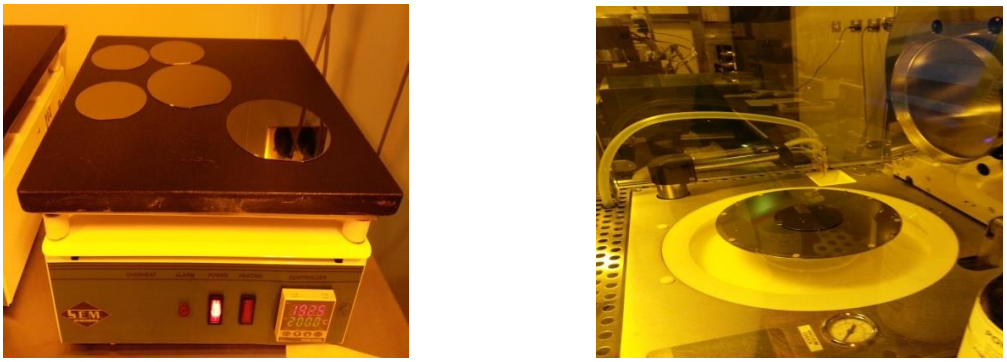

(a) (b)

Figure 6.22. Preheat and coating. (a) The wafers on heat at 200 °C, (b) wafers coated with SU-8 200 inside the spinner machine.

The next stage required *coating*. In this process the wafers are coated with SU-8 2000 (viscosity = 45000 cSt) which is a high contrast epoxy based photoresist designed for micromachining and microelectronic applications. The coated wafers are then placed in the spinner machine to smooth the photoresist and thin it to around 0.5 mm. The required time (s) and rotation (rpm) presented in Table 6.5 was developed by Australian National Fabrication Facility at University of South Australia. This process is achieved in 50 seconds, but varies depending on the photoresist thickness and viscosity, Fig. 6.22 (b) and Fig. 6.23.

Table 6.5. Control process of the photoresist. Time and rotation speed required for photoresist (SU-8 2100).

Step	Time (s)	Rotation (rpm)
Starts/lid closes	10	0
Speeds	10	500
Creating thickness	30	2500
Stops/lid opens	10	0

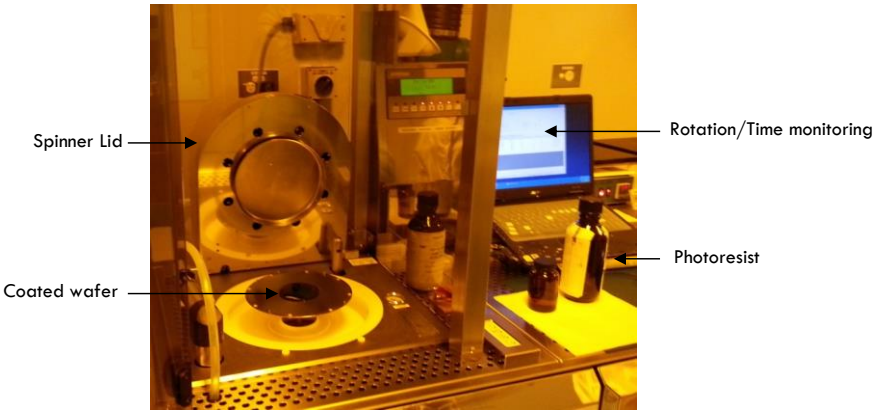

Figure 6.23. Coating process. The finalized coated photoresist wafer inside the spin machine.

In the next stage the coated wafers are placed in a heat oven for 15 minutes at 65 ^{o}C and then reheated again for 2 hours at 95 ^{o}C; this process is known as *soft baking*. The next stage required *exposing;* in this step the wafers were placed in the lithography machine and were aligned with the mask, Fig. 6.24. After exposing the pattern on the photoresist the next stage requires *post expose baking*. In this process the wafers are heated for 2 minutes at 65 ^{o}C and then reheated to 95 ^{o}C for 6 minutes. After baking, the wafers are washed with SU-08 developer and with isopropanol to stop the developer and then finally reheated for 25 minutes at 120 ^{o}C; to remove any unwanted water from the surface.

Figure 6.24. Lithography. Wafer under exposure, inside the lithography machine.

In the next stage the wafers are placed in plastic containers and are filled with 2 grams of Sylgard 184 silicon elastomer base plus its curing agents with the proportion of 10 g to 1g, Fig. 6.25 (a).

(a) (b)

Figure 6.25. PDMS top cover. (a) Sylgard 184 silicon elastomer being poured inside the plastic container on top of the designed wafer with channel, (b) final fabricated PDMS top cover with input/output pins.

The layers are then vacuumed for 15 minutes to remove all the air bubbles and then rested on a flat surface for around 15-20 minutes for the silicon elastomer to become smooth and then finally heated for 1 hour at 80 ^{o}C. In the last stage the developed PDMS is cut to the appropriate dimension and the syringe input/output pins are punched inside the channel, Fig 6.25 (b).

6.6.5 Pyrex cover

Given that Pyrex used for the top cover demonstrated high tuning in the simulation results, this material was purchased through Fry Optics (Australian based company) for prototype testing.

Pyrex materials are low-thermal-expansion glasses which are used mainly for kitchenware and laboratory glassware. Given that Pyrex glasses have low permittivity (ε_r= 4.82) and loss tangent ($tan\ \delta$ = 0.0054) they have been used for microwave applications. For this structure, these glasses were cut at a dimension of 20 × 80 mm and 20 × 100 mm, with a thickness (h_c) of 1.1 mm.

6.7 Measurement

6.7.1 Measurement setup

In this work the measurements was carried out using a parallel plate waveguide. Parallel plate waveguide are characterized by perfect conductor boundaries that are parallel to the z-axis. They consist of a plate spacing defined as d and plate width and length, defined by W_{wg} and L_{wg}. In this measurement, the waveguide plates had an equal width and length of 60 cm (W_{wg} = L_{wg}) and spacing (d) of 2 cm (Fig. 6.26). In order to measure the response frequency and transmission magnitude via this waveguide, two internal waveguide monopole antennas are connected to the two ports of the network analyser (N5230A PNA series) through coaxial cables. Given that the cut off frequency of the TM_n mode for this parallel plate waveguide is calculated by [139]

$$f_c = \frac{n}{2d\sqrt{\mu_\varepsilon}} \tag{6.1}$$

with $c = \frac{1}{\sqrt{\mu_\epsilon}} = 3 \times 10^8$ and d = 0.02 m, the cuff of frequency is therefore equal to 7.5 GHz. Since the designed FSS structure operates between 4 to 6 GHz (< 7.5 GHz), in this measurement only the transverse electromagnetic (TEM) mode is excited, with electric and magnetic fields both perpendicular (transverse) to direction of the propagation.

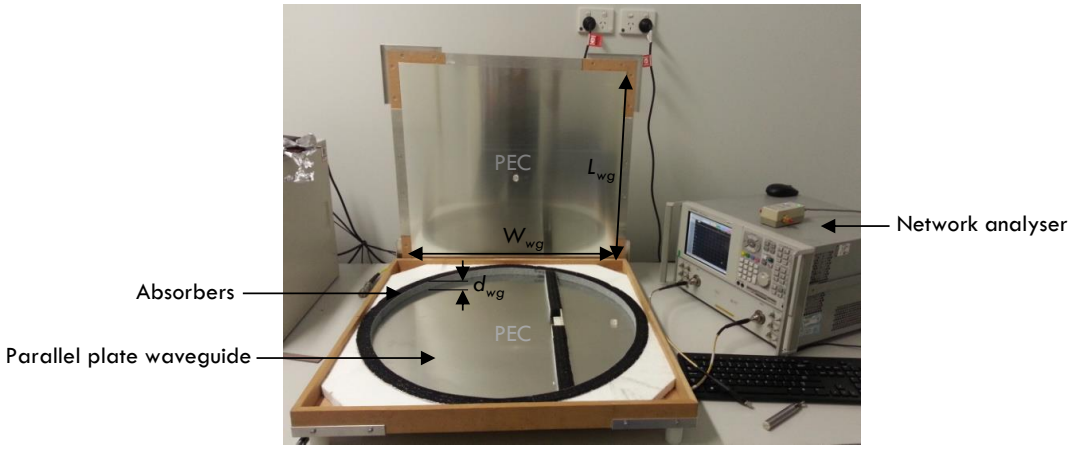

Figure 6.26. Parallel plate waveguide. The parallel plate waveguide used for ELC resonator measurement.

In the next section the ELC resonator is tested for two different applications: 1- *Oil/liquid sensor* and 2- *Tunable liquid crystal FSS*, which are discussed below.

6.8 Oil/liquid sensing

In this test the ELC resonator was used as a *sensor* for sensing oil and liquid samples. Two sets of oil samples were investigated and their equivalent relative permittivities were extracted. The ELC resonator was fabricated on Duroid 5880 as a 2 by 8 ELC array. However given that for oil/liquid sensing, no bias voltage was required, the bias lines were manually removed. To have a stable and even amount of oil/liquid sample, for each individual testing a sterile syringe was filled with 0.48 cc of sample and was poured on top of the structure, creating an 0.3 mm of thickness on an 2 by 8 ELC array (20 mm × 80 mm). The structure was then sealed using the Pyrex cover (ε_r = 4.82, $tan\ \delta$ = 0.0054). The final dimensions of each resonator cell were as follows: L = W = 10 mm, $h_{oil/liquid}$ = 0.3 mm, h_c = 1.1 mm and h_s = 3. 175 mm (see Fig. 6.27 and Fig. 6.28).

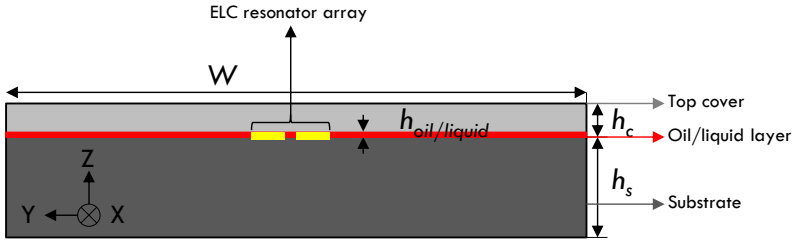

Figure 6.27. ELC resonator side view. ELC unit cell filled with oil/liquid sample.

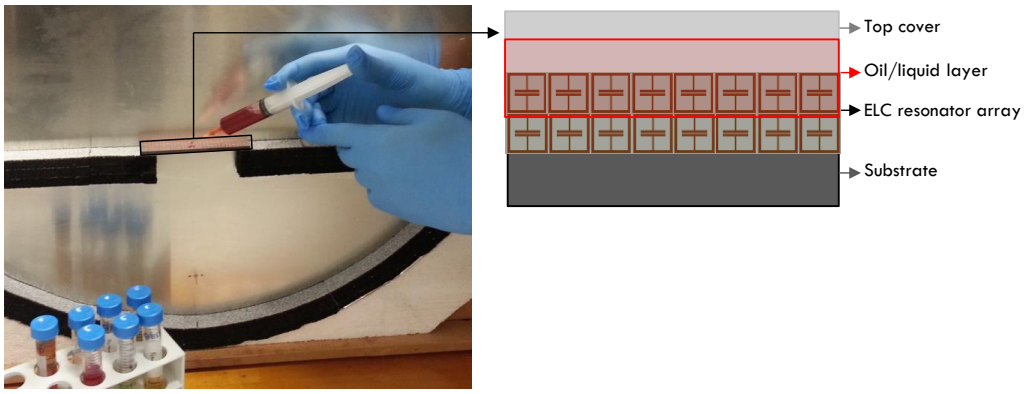

Figure 6.28. Filling process of the resonator. The ELC array during oil/liquid filling process.

The structure was initially tested without a top cover. In this case the ELC resonates at a frequency 6.28 GHz and has a transmission magnitude of -22 dB. However in the second case when the cover is closed, the resonant frequency shifts to a lower frequency of 5.52 GHz and has a transmission magnitude of -25 dB. Subsequently the structure was filled and tested with number of oil/liquid samples and was measured using the network analyser (N5230A PNA).

In this measurement, the normalized transmission magnitude, especially at higher frequency can be slightly higher than 0 dB. This effect is caused by the beam pattern alternation in the present of an ELC array, resulting in additional energy diffracted into the receiving monopole. Furthermore the waveguide was as well measured between 4–7 GHz with an empty cavity and the transmission magnitudes (dB) were recorded. In these experiments, all measured data were then subtracted from the measured data from an empty waveguide, resulting in a normalized transmission magnitude in dB, Fig. 6.29.

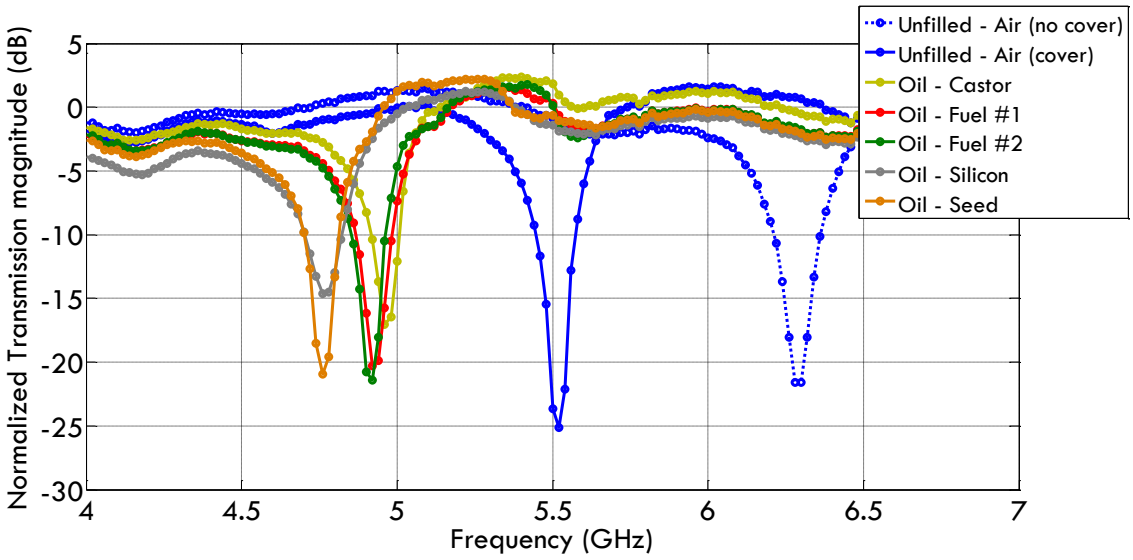

Figure 6.29. Oil sample measurements. Resonant frequency and transmission magnitude from the measurements.

The structure was simulated in CST (frequency range of 4 - 7 GHz) using periodic boundary conditions (Floquet port) (Fig. 6.30), the relative permittivities corresponding to the different oil samples were extracted from the software and these were compared with the available relative permittivities from the literature

[140]. Table 6.6 illustrates the complete results from both prototype measurements and extracted from full-wave simulation.

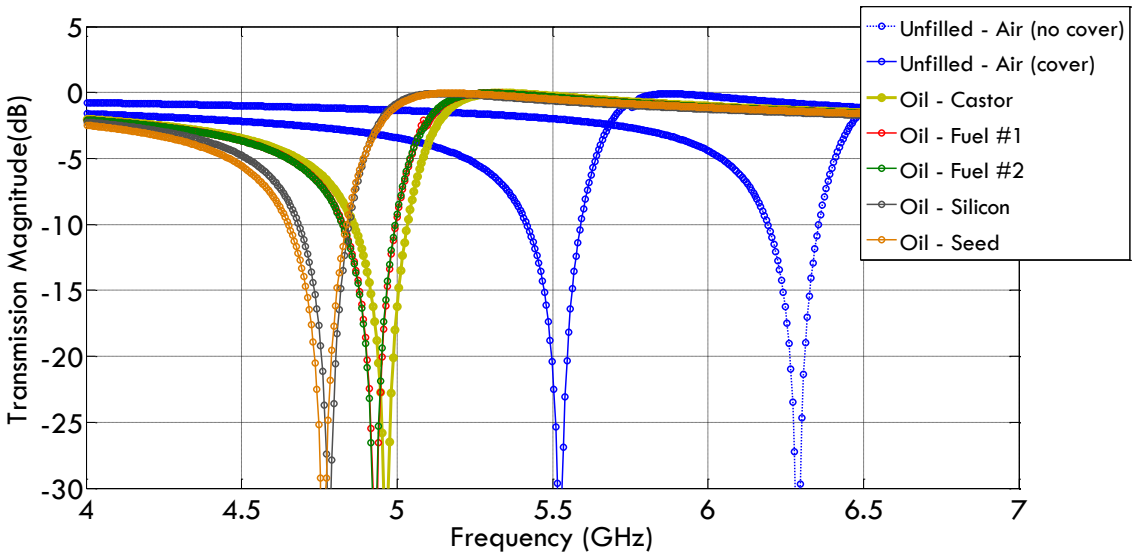

Figure 6.30. Oil sample extracted from the simulation. Resonant frequency and transmission magnitude from the simulation.

Table 6.6. Measured and extracted data. The resonant frequency, corresponding magnitude and the extracted relative permittivities of the oil samples.

Samples	Measured		Extracted			
	Fr (GHz)	Mag (dB)	Fr (GHz)	Mag (dB)	Extracted relative permittivity	Reference relative permittivity [140]
Unfilled - Air (no cover)	6.28	-25.5	6.29	-40.5	1.0	1.0
Unfilled - Air (cover)	5.52	-27	5.52	-35	1.0	1.0
Oil - Castor	4.96	-18	4.96	-39.5	2.58	2.60
Oil - Fuel #1	4.92	-22	4.92	-38	2.60	2.7
Oil - Fuel #2	4.93	-22.5	4.92	-38	2.60	2.7
Oil - Silicon	4.77	-15.5	4.78	-35	2.69	2.7
Oil - Seed	4.78	-22	4.79	-37	2.70	2.7

The comparison between extracted relative permittivity and referenced relative permittivity in Table 6.6, demonstrates sensing using the designed ELC resonator. The extracted relative permittivity from the simulation matches with the referenced relative permittivity of the oil presented in the literature.

Apart from samples tested above, petroleum products such as crude oils were tested for the purpose of ELC resonator sensing. Crude oil is unprocessed oil which is directly excavated from the ground and is commonly known as petroleum. Crude oils are a useful starting point for many different substances such as petrol, diesel fuel, jet fuel, kerosene as well as fertilizers and pesticides.

For this sensing validation, five different crude samples, from five different refineries from Santos (oil and gas company in Australia), were tested. Similarly to the previous testing, 0.48 cc of crude samples were injected on the top surface of the ELC resonator array made from RT/Duroid 5880 substrate (ε_s = 2.2 and tan δ_s = 0.0009), creating an 0.3 mm of crude oil on top of the 8 by 2 cell structure. Similar to the previous case the waveguide was measured with an empty cavity and the recorded transmission magnitudes (dB) were subtracted from the measured data. Fig. 6.31 illustrates the normalized results.

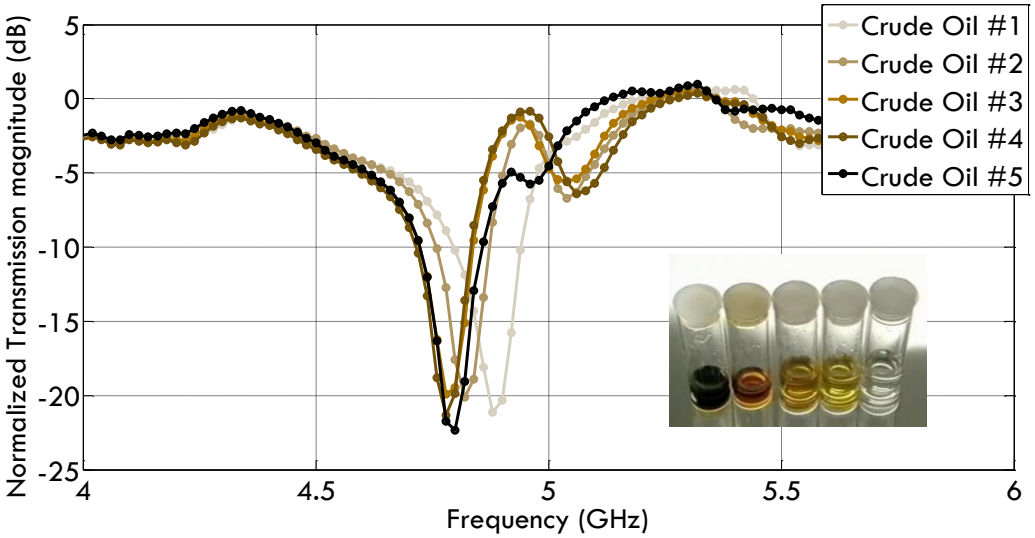

Figure 6.31. Crude oil sample measurements. Resonant frequency and transmission magnitude from the measurement.

The measured results from all crude samples indicate that the resonant frequency in all cases lies between 4.78 to 4.88 GHz, with transmission magnitude of around -20 to -25 dB. The slightly higher normalized transmission magnitudes (> 0 dB); around 5.25 GHz are explained by the beam pattern alternation in the present of the array, causing additional energy diffracted into the receiving monopole.

Furthermore the results were simulated in CST (Fig. 6.32) and the corresponding relative permittivities were extracted and compared with the literature, Table 6.7.

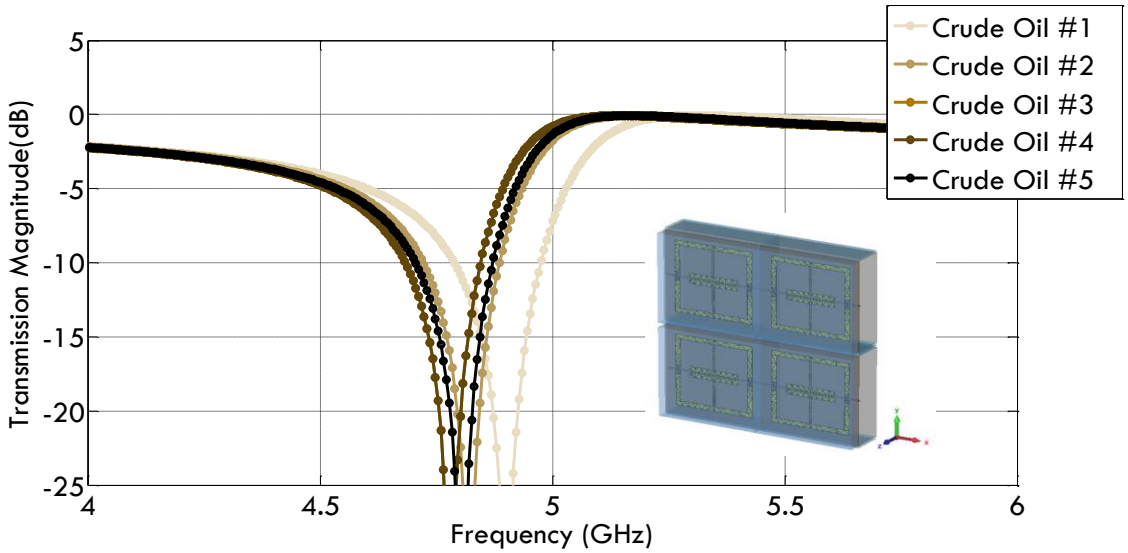

Figure 6.32. Crude oil sample simulated. Resonant frequency and transmission magnitude from the simulation.

Table 6.7. Measurement and extracted data. The resonant frequency, corresponding magnitude and the extracted relative permittivities from the crude oil samples.

Samples	Measured		Extracted		
	Fr (GHz)	Mag (dB)	Fr (GHz)	Mag (dB)	Extracted relative permittivity
Crude Oil #1	4.88	-20.5	4.88	-34.6	2.62
Crude Oil #2	4.82	-19.7	4.82	-35.9	2.67
Crude Oil #3	4.78	-19.5	4.78	-33.8	2.69
Crude Oil #4	4.78	-21	4.78	-33.8	2.69
Crude Oil #5	4.80	-22	4.80	-33.7	2.68
Average					**2.67**

The extracted results indicate that in all crude oil samples, the extracted relative permittivity is between 2.62–2.69 with an average value of around 2.67. The final averaged relative permittivity (ε_r = 2.67) is closely matched with the relative permittivity of crude oils previously reported by Xiuwen et al. [141] to be around 2.5 and by Schüller et al. [142] to be between 2.5-8. The minor variations in the crude oil resonant frequencies are due to the different mineral particles in the oil, resulting in a slight variation in their material characteristics and properties.

6.9 Novel liquid crystal FSS

6.9.1 Tunable liquid crystal FSS

In this experiment, the designed FSS structure was filled with liquid crystal mixture (GT3-23001) and sealed using a Pyrex top cover, to avoid any liquid leakage. The structure was ultimately placed in the parallel plate waveguide, connected to the power supply and measurements were recorded using the network analyser, Fig. 6.33.

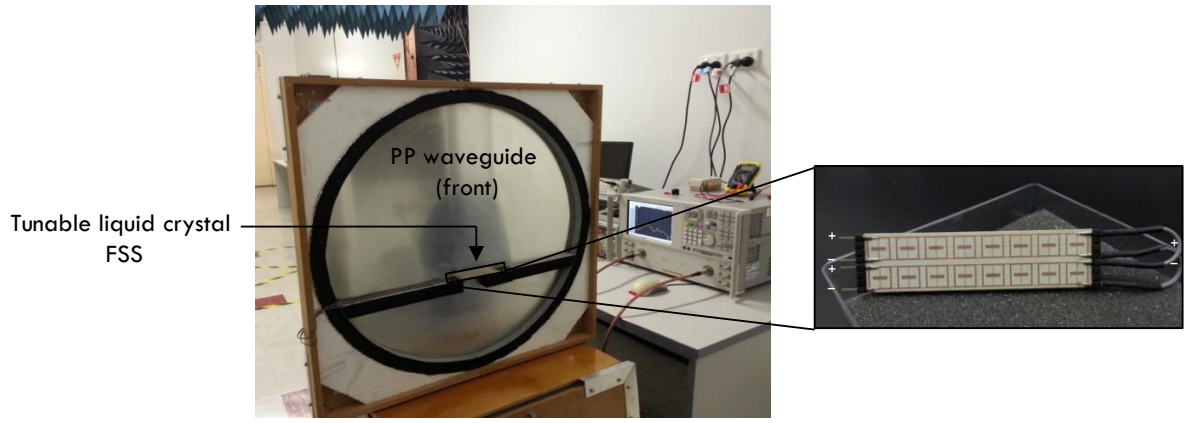

(a)

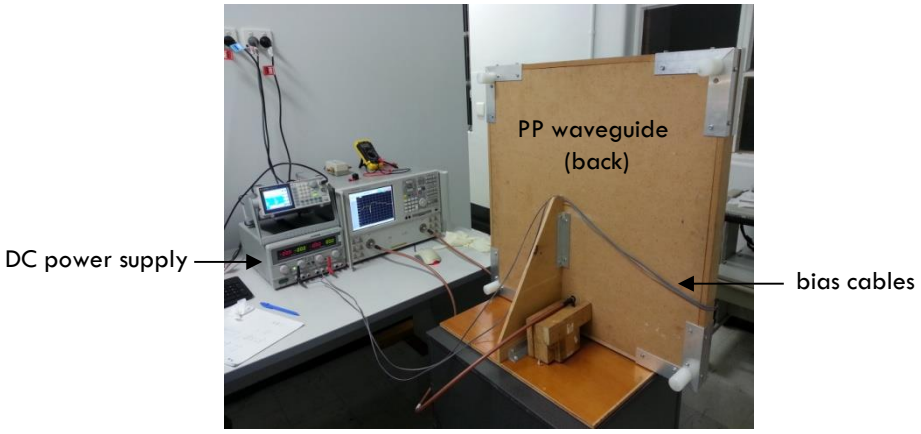

(b)

Figure 6.33. **Tunable liquid crystal FSS measurement setup.** (a) Front view, demonstrating the final FSS filled with GT3-23001 mixture and placed inside the waveguide (b) Back view, illustrating the closed waveguide during the measurement, with bias cables connected to both the FSS and the power supply.

For the initial testing the measurement was carried out on an 8 by 2 cell, filled with 0.3 mm thickness (h_{lc}) of liquid crystal, fabricated on a Duroid 5880 substrate without a microfluidic channel. In this experiment the bias voltage was gradually increased and the resonant frequency shift was recorded at significant points. The observed results indicate that by varying the bias voltage from 0 to 30 V, the resonant frequency continuously shifts from 4.30 GHz to 4.24 GHz, indicating a tuning of 1.4% with respect to the lower frequency, Table 6.8 and Fig. 6.34 (normalized).

Table 6.8. Recorded measurement data on 5880. Table below illustrates the applied bias voltage applied and its corresponding measured resonant frequency.

Sample	Recorded data		
	Fr (GHz)	Voltage (V)	Magnitude (dB)
GT3-23001	4.30	0	-17.5
	4.30	5	-21.5
	4.28	10	-28.5
	4.27	15	-22
	4.24	30	-24.5
	4.24	45	-22

The above results also indicate that by increasing the voltage to even as high as 45 V (well above the Frederiks threshold [80]) the FSS resonant frequency remains unchanged at 4.24 GHz. This stability is due to complete alignment of the liquid crystal molecules and reaching a parallel stage ($\varepsilon_{eff} = \varepsilon_{\parallel}$).

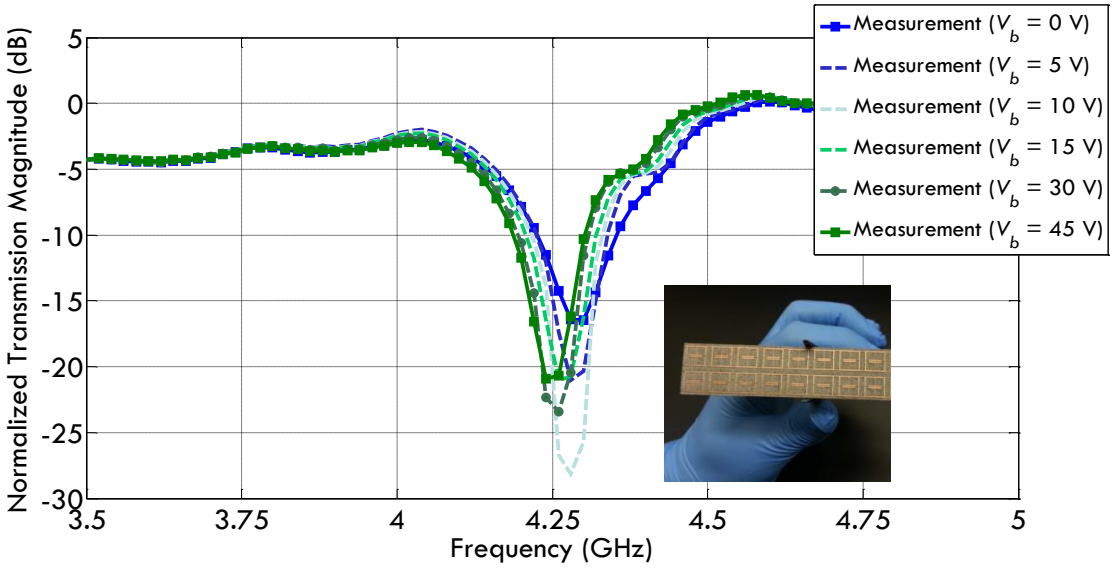

Figure 6.34. Tunable FSS measurement. The resonant frequency and corresponding transmission magnitude at different bias voltage.

In the second validation, the tunable FSS was fabricated on the 6002 high frequency laminate from Rogers. In this measurement, to increase the sensitivity and consequently the tuning performance, a microfluidic channel (0.15 x 0.2 mm) was created inside the substrate, between the capacitive gaps (see Fig. 6.21). In the initial stage, when no bias voltage is applied (V = 0 V), the FSS has a resonant frequency of around 4.44 GHz. However as the bias voltage starts to increase from 0 V to 15 V, the resonant frequency continuously shifts from 4.44 GHz to lower frequencies. Ultimately by increasing the voltage to a maximum of 30 V, the FSS reaches 4.30 GHz, illustrating a tuning of 3.15% with respect to lower frequency and remains unchanged as the voltage is further increased (45 V), Fig. 6.35 and Table 6.9. The tuning for the proposed design will further improve through applying polyimide coating to the top of the substrate and bottom of the top cover.

Table 6.9. Recorded measurement data on 6002. The measured resonant frequency at different bias voltages.

Sample	Measurement	
	Fr (GHz)	Voltage (V)
GT3-23001	4.44	0
	4.34	10
	4.33	15
	4.30	30
	4.30	45

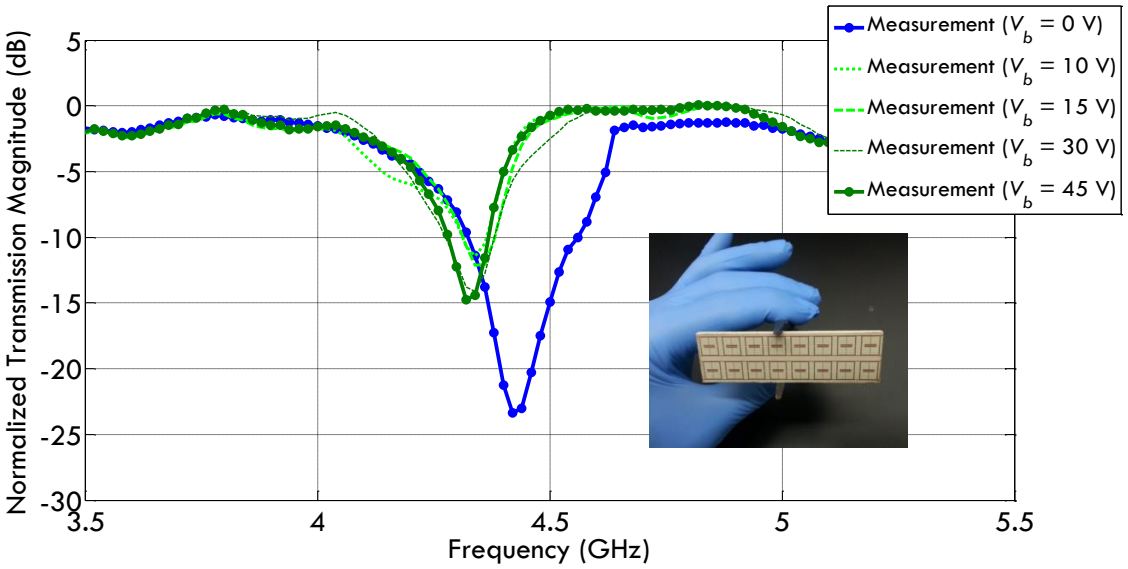

Figure 6.35. Tunable liquid crystal FSS measurement. The resonant frequency as a result of increasing the bias voltage from V_{th} (0 V) to maximum V_{max} (30 V).

The observed result from the network analyser indicates a switching time of a fraction of a second (< 1 sec) between unbiased (V_b = 0 V) and biased voltage state (V_b = 30 V). However the response time is larger for back switching (> 1 sec), owing to the free relaxation time (response time) of the liquid crystal molecules, which is proportional to the liquid crystal cell thickness.

6.9.2 Liquid crystal FSS switch

Apart from frequency tuning, the designed FSS in addition demonstrates switching at 4.44 GHz, between bias and unbiased states. Fig. 6.36 represents the difference of both curves for 0 V (unbiased-OFF) and 45 V (biased-ON) as a function of the frequency. It can be clearly observed that where the transmission magnitude is at the maximum (around 20.5 dB) at a resonant frequency of a 4.44 GHz, the proposed FSS can be used as a switch, between nearly complete transmission and 20.5 dB suppression of transmission, with a bandwidth of around 100 MHz (4.49 - 4.39) at

-15 dB.

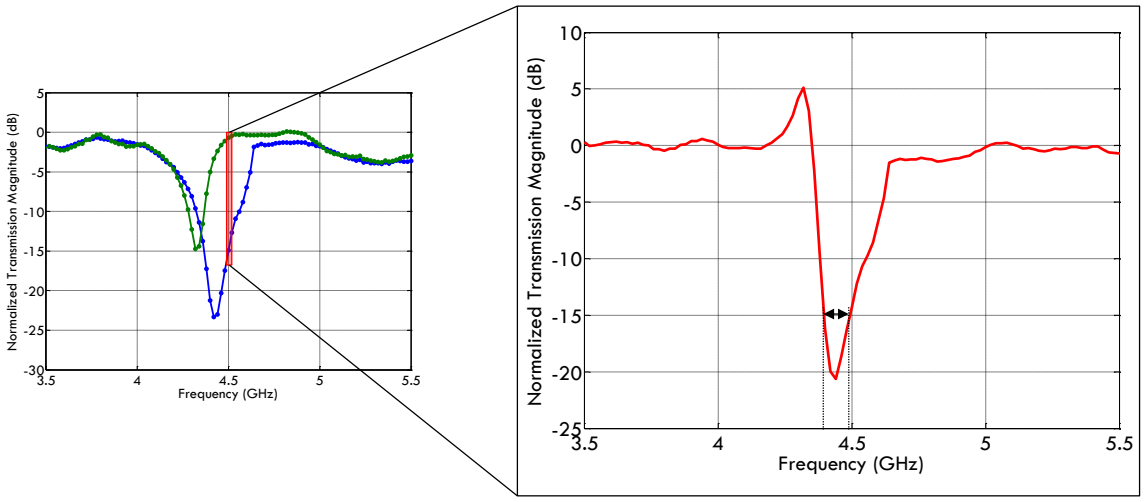

Figure 6.36. Liquid crystal FSS switching. Switching using the designed FSS at 4.44 GHz through applying bias voltage of around 45 V. The plot (right) indicates the difference between the two plots (left) at 4.44 GHz for unbiased (OFF) and biased (ON) states (highlighted in red square).

The switching could be further improved through applying polyimide coating to the top and bottom of surface to increase the tuning performance and which therefore in

the ideal case, the minimum of the unbiased curve (blue) would match with the 0 dB of the biased curve (green), rather than -1.4 dB difference.

6.9.3 Comparison and further analysis

For final verification, the manufactured dimensions of the structure were remeasured and were then implemented in the simulation software. The measurements were all identical to the reported data (see Table 6.1), except the substrate height h_s was measured to be 3.0 mm (3.05 mm in previous report) and the liquid thickness h_{lc} to be around 0.3 mm (0.4 mm in previous report), Table 6.10 (updated).

Table 6.10. Final fabricated FSS dimensions. Dimensions of the final fabricated structure.

L	*W*	*a*	*b*	*d*	*g*	*s*	*x*	*y*	h_s	h_{lc}
10 mm	10 mm	0.5 mm	0.2 mm	5 mm	0.2 mm	1.15 mm	1 mm	0.3 mm	3.0 mm	0.3 mm

Given that the top cover of the parallel plate waveguide had a 2.5 mm gap, this spacing was in addition added to the simulation as an air gap. In the initial state of simulation for when the molecules are in a perpendicular formation, the structure has a resonance at 4.45 GHz, with transmission magnitude of around -30.2 dB. This agrees well with the measured FSS in an unbiased state, with a resonant frequency of 4.44 GHz at -21.5 dB. Furthermore in the parallel state, as the liquid crystal effective relative permittivity is altered from 2.5 to 3.3, the resonant frequency of the proposed FSS shifts to 4.20 GHz with transmission magnitude of -31.1 dB.

However this value was measured to be at 4.30 GHz with transmission magnitude of -15 dB for the biased state. The lower frequency shift in the measurement is owed to the elimination of the polyimide layer, given that this coating was impracticable for a 0.15 mm channel in the standard university research laboratory. This could be additionally investigated and develop through calibration with industry partners (e.g. Melbourne centre for nanofabrication), were by applying polyimide coating inside the channel tuning performance could be well further improved.

In the end, to identify the approximate relative permittivity of the liquid crystal for the measured biased state, curve fitting was employed in the CST simulation, and a relative permittivity of 3.0 and a loss tangent of 0.04 was extracted, Fig. 6.37.

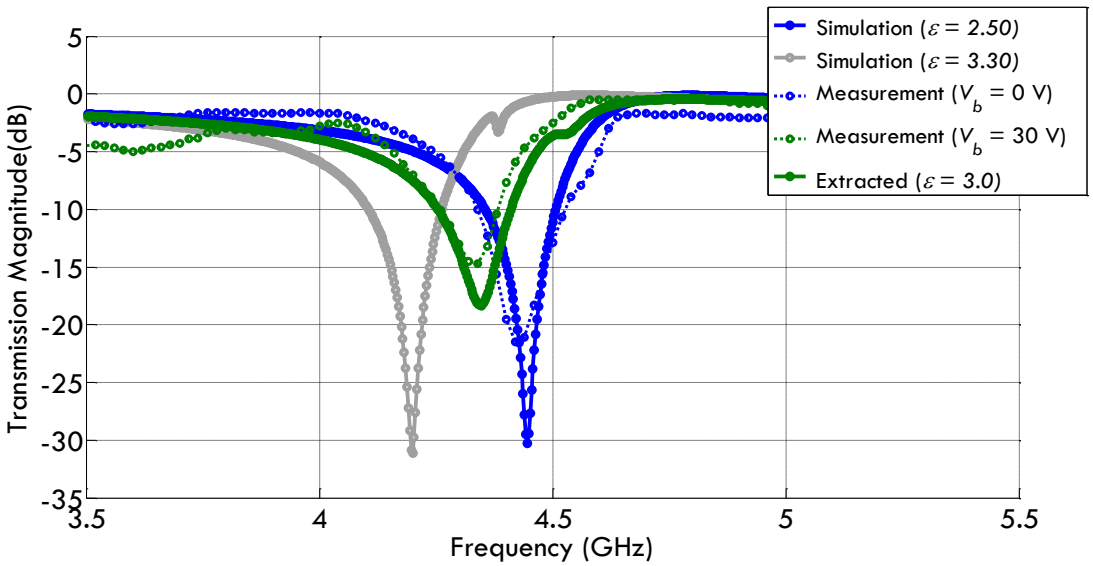

Figure 6.37. Comparison between simulation and measurement. The comparison between the simulation and the prototype fabrication.

Furthermore, the designed FSS was as well tested with PDMS as its top lid (see Sec. 6.64). In the full-wave ideal simulation model, PDMS illustrated around 5.91% of frequency tuning for GT3-23001, 2.14% using BL037 and around 1.37% using standard liquid crystal sample K15.

However in measurement, due to the stickiness of the liquid crystal molecules to the PDMS surface, both the tuning range (τR) and the tuning (τ), reduces to around 1.08%, illustrating a tuning between 4.68 GHz at no zero bias voltage (V_b = 0 V) to 4.63 GHz, when maximum bias voltage is applied (V_{max} = 30 V). Similar to the previous case the parallel waveguide was as well measured between 4.25–5.5 GHz with an empty cavity and the transmission magnitudes (dB) were recorded. These values were then subtracted from the measured data, resulting in normalized transmission magnitude in dB, Fig. 6.38.

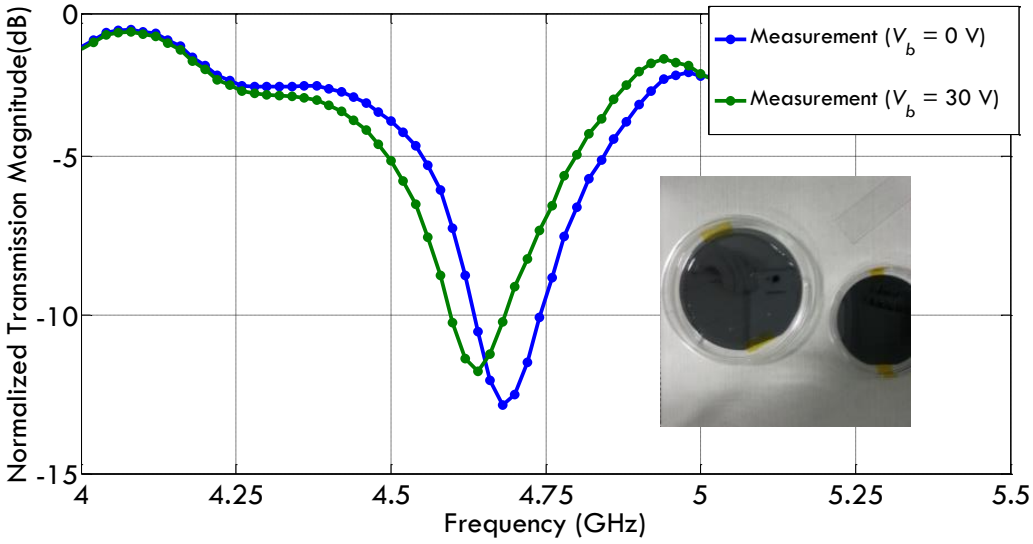

Figure 6.38. Measurement of the tunable FSS. Tuning performance of the designed FSS filled with liquid crystal mixture (GT3-23001) covered with PDMS.

6.10 Conclusion and summary

In this chapter, the ELC (electric-*LC*) resonators which have been discussed as a building block for metamaterials absorbers, reflectors, modulators, and filters, have been modified to incorporate a narrow microfluidic channel in its central capacitive gaps. This modification results into two individual applications: sensors and tunable frequency selective surfaces.

In the initial section the modified ELC resonant design is fabricated and measured through using five different oil and petrol samples. The extracted electrical properties demonstrate a close match between the measurement and the results previously reported in the literature, illustrating oil or liquid sensing using ELC resonators.

In addition the modified ELC resonators have been demonstrated in an array to form continuously tunable frequency selective surfaces at C-band using liquid crystal material. This novel FSS illustrates 6% of continuous tuning in simulation and around 3.15% of tuning for the prototype measurement. The discrepancy is

attributed to the lack of polyimide coating. The achieved results demonstrate ELC resonators in an array to form a tunable liquid crystal frequency selective surface. Finally rather than the common application of continuous tuning, the proposed FSS can be implemented in a microwave device for switching between complete transmission and 20 dB suppression.

Chapter 7

Thesis Summary

THIS chapter concludes the thesis. Chapter 1 and 2 contain review materials on various reconfiguration mechanisms, fundamental design approaches and comprehensive overview of the properties of liquid crystal materials. Chapter 3 and 4 discusses on a novel high performance of tunable liquid crystal S-band resonator design, optimization and prototype measurement. Chapter 5 illustrates the possibility of using lumped-element circuit models for rapid calculation of liquid crystal devices at microwave frequencies. Ultimately, Chapter 6 includes an original tunable liquid crystal FSS which can also be used as an ELC array for sensing. This chapter focuses on summarising the original contributions.

7.1 Reconfigurable/tunable classification: Chapter 1,2

Background: The potential of liquid crystals as reconfigurable/tunable materials arises from their ability for continuous tuning with lower power consumption, transparency and possible integration with printed and flexible circuit technologies. Although examples and applications of these materials have been presented in the past, there is a still a need of gathering all available relevant and applicable literature in a single format to assist future development in liquid crystal technology.

Methodology: Technological, scientific papers and primary text books were reviewed. Additionally the knowledge developed from practical experience and experimental challenges were studied.

Results: This review describes physical theory and fundamental electrical properties arising from the anisotropy of liquid crystals and overviews selected realized liquid crystal devices, throughout four main categories: resonators and filters, phase shifters and delay lines, antennas and finally frequency-selective surfaces and metamaterials.

Future work: The work can be extended to demonstrate complete structures from the literature and their corresponding dimensions in a table format. In addition, it can cover the millimeter-wave and terahertz frequency range, where the dissipation of liquid crystal is lower.

Original contribution: A review journal paper on electrically tuned microwave devices using liquid crystal technology has been written. This work gathers all available liquid crystal mixtures and their electrical properties from the literature in one single table. Furthermore the article describes polyimide coating and molecule alignment in depth, which is commonly omitted in the literature or simply just referred to in a single line. *(see publications, [1] P. Yaghmaee et al. 2013)*

7.2 Tunable and high performance resonator: Chapter 3,4

Background: In the past, various frequency tunable liquid crystal devices have been designed and investigated operating at high microwave or millimetre wave frequencies (> C-band), however less attention has been given to lower microwave frequency range (< C-band) where most current microwave devices operate. In this study a tunable resonator operating at S-band using two different liquid crystal samples is designed, simulated and manufactured.

Methodology: The resonator is initially designed through analytical electromagnetic theory and investigated and modelled using a full-wave electromagnetic simulation tool. On top of that, the final optimized model is then fabricated using standard electronic manufacturing methods.

Results: The experiment is carried out using various liquid crystal samples. The achieved results from both the full-wave electromagnetic simulation and the prototype measurements are compared and the results are evaluated to validate the concept.

Future work: The tuning can be improved by using higher dielectric anisotropy liquid crystal mixtures (if developed in the future). Furthermore switching time improvement can also be expected by reducing the cell thickness and producing finer grooves on the polyimide layer.

Original contribution: For the first time, a tunable resonator operating at S-band is presented which makes use of a new high performance liquid crystal mixture (GT3-23001). The 4% and 8.2% of frequency tuning in this work opens new possibilities for future applications of liquid crystals mixtures at even a lower microwave frequency (e.g. biomedical applications). *(see publications, [2] and [3] P. Yaghmaee et al. 2012)*

7.3 Multilayered tunable SIR resonator: Chapter 5

Background: A range of multi-layered liquid crystal tunable devices have been presented in the literature mainly based on the full-wave electromagnetic simulation model. However even for relatively simple simulations, these require an unacceptably extensive computational time. Therefore demonstration of a simpler model for rapid calculation of liquid crystal microwave device performance is still required.

Methodology: Stepped-impedance resonator theory and ADS lumped-element circuit model simulation were employed as tools for designing a multilayered tunable microwave filter.

Results: By using different liquid crystal samples and comparing the lumped-element circuit simulation with the full-wave electromagnetic simulations and prototype measurements, good agreements were observed. The reported work indicates faster simulation and lower computational cost in the optimization phase of more sophisticated designs.

Future work: The final results can be further improved by taking one more step and considering eliminated losses in the circuit model. Moreover defining the electrical and physical properties of the actual liquid crystal sample at the desired frequency will undoubtedly assist in finer modelling and enhanced fitting of the simulation and measurement curves.

Original contribution: A microwave band-pass filter cell filled with liquid crystal mixture was modelled by a lumped-element circuit. Good agreement between simulations and prototype measurements demonstrate the option of using the lumped element circuit model for rapid simulation of liquid crystal microwave devices, which can provide faster simulation and lower computational cost in the optimization phase of more sophisticated designs. *(see publications, [4] P. Yaghmaee et al. 2012)*

7.4 Sensing and tunable FSS: Chapter 6

Background: Frequency selective surfaces are implemented for designing band-pass filters, polarizers and beamsplitters. Even though considerable work was carried on various geometries and specifications, nevertheless with the recent demand for reconfigurability and current development in the material technology, there is still a need for designing a tunable FSS.

Methodology: In this work the FSS is modified through analytical electromagnetic theory, and investigated through full-wave electromagnetic simulations. In addition, a prototype of the optimized FSS model is then fabricated and validated using liquid crystal material. The FSS is also used for oil/liquid sensing.

Results: In the preliminary section the modified FSS which consists of an array of ELC resonators demonstrated sensing for different oil samples. Furthermore in the second stage the modified FSS was combined with liquid crystal mixture, creating a tunable or switchable FSS with operational frequency in C-band.

Future work: The final results can be further tested by extending the number of prototype cell elements, and to some extent improved through coating the top layer with polyimide film. Ultimately for using lower amount of liquid crystal mixture, the FSS can be design as an interlayer capacitance, with the liquid only in the central layer.

Original contribution: For the first time a tunable liquid crystal FSS with an operational frequency of C-band has been designed and manufactured. This modified ELC cell illustrates both oil/liquid sensing and high tunability at lower microwave frequency range. Moreover the proposed FSS indicates switching between complete transmission and no transmission. *(see publications, [5] P. Yaghmaee et al. 2013, [6] and [7] P. Yaghmaee et al. and [8] A. Ebrahimi and P. Yaghmaee et al. 2013)*

Appendix A

Material Transfer Agreement

A **MATERIAL** transfer agreement for transferring liquid crystal samples from Merck KGaA, Frankfurt Str, 250, 64293, Darmstadt, Germany and Department of Electrical and Electronics Engineering, North Trace Campus, University of Adelaide, Adelaide, South Australia (SA), Australia. This appendix includes the complete agreement and the final approval signed by both institutions.

A.1 Transfer agreement

A material transfer agreement (MTA) was organized by Merck KGaA, Frankfurt Str, 250, 64293, Darmstadt, Germany (hereinafter referred to as "MERCK") and School of Electrical and Electronics Engineering, North Terrace Campus, University of Adelaide, Adelaide, South Australia (SA), Australia (hereinafter referred to as "RECIPIENT").

Through signing this agreement, the university had the legal right to purchase liquid crystal (licristal) and the newly developed mixture (GT3-23001) for validation and testing. However the final data and written article needed to be reviewed by the Merck (PM-LR1 department) in Germany before public publishing. A copy of the final agreement approval is presented in Fig. A.1

MERCK

Merck KGaA · Germany · Frankfurter Str. 250 · 64293 Darmstadt

Mr. Pouria Yaghmaee
PhD Postgraduate Student
School of Electrical & Electronic Engineering
The University of Adelaide
Adelaide SA 5005,
AUSTRALIA

Date 07 June 2011
Division/Dept. PM-LR1
Care of Atsutaka Manabe
Phone +49 6151 728249
Fax +49 6151 723135
E-Mail atsutaka.manabe@merckgroup.com

Material Transfer Agreement between Merck KGaA and University of Adelaide

Dear Mr. Yaghamaee

Please find attached the original Material Transfer Agreement signed by all parties for your documentation.

Yours truly

Merck KGaA

i.A.

Atsutaka Manabe

Encl.

Merck KGaA · Germany
Frankfurter Str. 250
64293 Darmstadt
Phone +49 6151 72-0
Fax +49 6151 72-2000
www.merck.de

Corporation with General Partners
Commercial Register AG Darmstadt HRB 6164
Registered Office: Darmstadt
Chairman of the Supervisory Board:
Rolf Krebs

Executive Board and General Partners:
Karl-Ludwig Kley (Chairman),
Michael Becker, Kai Beckmann, Stefan Oschmann,
Bernd Reckmann, Matthias Zachert

Figure A.1. Final material approval. According to this agreement the University of Adelaide was given the legal right to purchase, test and validate newly developed liquid crystal mixtures from Merck.

References

[1] O. H. Karabey, S. Bildik, S. Bausch, S. Strunck, A. Gaebler, and R. Jakoby, "Continuously polarization agile antenna by using liquid crystal-based tunable variable delay lines," *IEEE Transactions on Antennas and Propagation,* vol. 61, pp. 70-76, 2013.

[2] M. Yazdanpanahi and D. Mirshekar-Syahkal, "Millimeter-wave liquid-crystal-based tunable bandpass filter," *IEEE Radio and Wireless Symposium,* pp. 139-142, 2012.

[3] P. J. Collings and M. Hird, "*Introduction to Liquid Crystals: Chemistry and Physics,*" Philadelphia, PA: CRC Press, 1997.

[4] (25 August 2013). *Lemieux Group*. Available: http://www.chem.queensu.ca

[5] N. Bui-Hai and T. Martinez, "Visualization of microwave radiations with liquid crystals," *International Symposium on Antennas and Propagation Society,* vol. 21, pp. 537-540, 1983.

[6] W. J. Padilla, M. T. Aronsson, C. Highstrete, M. Lee, A. J. Taylor, and R. D. Averitt, "Electrically resonant terahertz metamaterials: Theoretical and experimental investigations," *Physical Review,* vol. 75, p. 041102, 2007.

[7] L. Liu and R. J. Langley, "Liquid crystal tunable microstrip patch antenna," *Electronics Letters,* vol. 44, pp. 1179-1180, 2008.

[8] W. Hu, M. Y. Ismail, R. Cahill, H. S. Gamble, R. Dickie, V. F. Fusco, D. Linton, S. P. Rea, and N. Grant, "Phase control of reflectarray patches using liquid crystal substrate," *First European Conference on Antennas and Propagation,* pp. 1-6, 2006.

[9] M. Boti, L. Dussopt, and J. M. Laheurte, "Circularly polarised antenna with switchable polarisation sense," *Electronics Letters,* vol. 36, pp. 1518-1519, 2000.

[10] F. Goelden, A. Gaebler, M. Goebel, A. Manabe, S. Mueller, and R. Jakoby, "Tunable liquid crystal phase shifter for microwave frequencies," *Electronics Letters,* vol. 45, pp. 686-687, 2009.

[11] G. H. Huff and J. T. Bernhard, "Integration of packaged RF MEMS switches with radiation pattern reconfigurable square spiral microstrip antennas," *IEEE Transactions on Antennas and Propagation,* vol. 54, pp. 464-469, 2006.

[12] O. H. Karabey, A. Gaebler, S. Strunck, and R. Jakoby, "A 2-D electronically steered phased-array antenna with 2 by 2 elements in LC display Technology," *IEEE Transactions on Microwave Theory and Techniques,* vol. 60, pp. 1297-1306, 2012.

[13] M. Sazegar, Z. Yuliang, H. Maune, C. Damm, Z. Xianghui, and R. Jakoby, "Compact tunable phase shifters on screen-printed BST for balanced phased arrays," *IEEE Transactions on Microwave Theory and Techniques,* vol. 59, pp. 3331-3337, 2011.

[14] C. Fritzsch, S. Bildik, and R. Jakoby, "Ka-band frequency tunable patch antenna," *IEEE Antennas and Propagation Society International Symposium,* pp. 1-2, 2012.

[15] F. Goelden, A. Gaebler, O. Karabey, M. Goebel, A. Manabe, and R. Jakoby, "Tunable band-pass filter based on liquid crystal," *German Microwave Conference,* pp. 98-101, 2010.

[16] C. Damm, M. Maasch, R. Gonzalo, and R. Jakoby, "Tunable composite right/left-handed leaky wave antenna based on a rectangular waveguide using liquid crystals," *IEEE MTT-S International Microwave Symposium Digest,* pp. 13-16, 2010.

[17] D. F. Sievenpiper, J. H. Schaffner, H. J. Song, R. Y. Loo, and G. Tangonan, "Two-dimensional beam steering using an electrically tunable impedance surface," *IEEE Transactions on Antennas and Propagation,* vol. 51, pp. 2713-2722, 2003.

[18] E. Erdil, K. Topalli, M. Unlu, O. A. Civi, and T. Akin, "Frequency tunable microstrip patch antenna using RF MEMS technology," *IEEE Transactions on Antennas and Propagation,* vol. 55, pp. 1193-1196, 2007.

[19] C. J. Panagamuwa, A. Chauraya, and J. C. Vardaxoglou, "Frequency and beam reconfigurable antenna using photoconducting switches," *IEEE Transactions on Antennas and Propagation,* vol. 54, pp. 449-454, 2006.

[20] J. T. Bernhard, "*Reconfigurable Antennas,*" Morgan & Claypool Publishers, University of Illinois at Urbana–Champaign, 2007.

[21] D. N. Lapedes, "*McGraw-Hill Dictionary of Scientific and Technical Terms,*". McGraw-Hill, New York, 1978.

[22] A. Petosa, "Frequency agile antennas for wireless communications - A survey," *14th International Symposium on Antenna Technology and Applied Electromagnetics and the American Electromagnetics Conference,* pp. 1-4, 2010.

[23] J. Kiriazi, H. Ghali, H. Ragaie, and H. Haddara, "Reconfigurable dual-band dipole antenna on silicon using series MEMS switches," *IEEE Antennas and Propagation Society International Symposium,* vol. 1, pp. 403-406, 2003.

[24] K. C. Gupta, L. Jun, R. Ramadoss, and W. Chunjun, "Design of frequency-reconfigurable rectangular slot ring antennas," *IEEE Antennas and Propagation Society International Symposium,* vol. 1, p. 326, 2000.

[25] D. Peroulis, K. Sarabandi, and L. P. B. Katehi, "Design of reconfigurable slot antennas," *IEEE Transactions on Antennas and Propagation,* vol. 53, pp. 645-654, 2005.

[26] F. Yang and Y. Rahmat-Samii, "Patch antenna with switchable slot (PASS): Dual-frequency operation," *Microwave and Optical Technology Letters,* vol. 31, pp. 165-168, 2001.

[27] D. Schaubert, F. Farrar, A. Sindoris, and S. Hayes, "Frequency agile microstrip antennas," *Antennas and Propagation Society International Symposium,* vol. 18, pp. 601-604, 1980.

[28] S. Kawasaki and T. Itoh, "A slot antenna with electronically tunable length," *Antennas and Propagation Society International Symposium,* pp. 130-133, 1991.

[29] C. W. Jung, Y. J. Kim, Y. E. Kim, and F. De Flaviis, "Macro-micro frequency tuning antenna for reconfigurable wireless communication systems," *Electronics Letters,* vol. 43, pp. 201-202, 2007.

[30] J. T. Bernhard, E. Kiely, and G. Washington, "A smart mechanically actuated two-layer electromagnetically coupled microstrip antenna with variable frequency, bandwidth, and antenna gain," *IEEE Transactions on Antennas and Propagation,* vol. 49, pp. 597-601, 2001.

[31] J. C. Langer, J. Zou, C. Liu, and J. T. Bernhard, "Micromachined reconfigurable out-of-plane microstrip patch antenna using plastic deformation magnetic actuation," *IEEE Microwave and Wireless Components Letters,* vol. 13, pp. 120-122, 2003.

[32] D. M. Pozar and V. Sanchez, "Magnetic tuning of a microstrip antenna on a ferrite substrate," *Electronics Letters,* vol. 24, pp. 729-731, 1988.

[33] R. K. Mishra, S. S. Pattnaik, and N. Das, "Tuning of microstrip antenna on ferrite substrate," *IEEE Transactions on Antennas and Propagation,* vol. 41, pp. 230-233, 1993.

[34] A. D. Brown, J. L. Volakis, L. C. Kempel, and Y. Botros, "Patch antennas on ferromagnetic substrates," *IEEE Transactions on Antennas and Propagation,* vol. 47, pp. 26-32, 1999.

[35] J. Valasek, "Piezo-electric and allied phenomena in Rochelle salt," *Physic review,* vol. 17, p. 475, 1921.

[36] E. A. Fardin, "*Barium strontium titanate thin films for tunable microwave applications,*". RMIT University, Australia, 2007.

[37] B. A. Baumert, L. H. Chang, A. T. Matsuda, T. L. Tsai, C. J. Tracy, R. B. Gregory, P. L. Fejes, N. G. Cave, W. Chen, D. J. Taylor, T. Otsuki, E. Fujii, S. Hayashi, and K. Suu, "Characterization of sputtered barium strontium titanate and strontium titanate-thin films," *Journal of Applied Physics,* vol. 82, pp. 2558-2566, 1997.

[38] A. Tombak, J. P. Maria, F. Ayguavives, J. Zhang, G. T. Stauf, A. I. Kingon, and A. Mortazawi, "Tunable barium strontium titanate thin film capacitors for RF and microwave applications," *IEEE Microwave and Wireless Components Letters,* vol. 12, pp. 3-5, 2002.

[39] Z. Chenhao, A. Alemayehu, M. A. Patterson, and G. Subramanyam, "Design of high voltage tunable Shunt Interdigitated resonator based on Barium Strontium Titanate thin film," *Proceedings of the 2011 IEEE National Aerospace and Electronics Conference (NAECON),* pp. 305-308, 2011.

[40] M. Nikfalazar, M. Sazegar, Z. Yuliang, H. Maune, A. Mehmood, and R. Jakoby, "Tunable split ring resonators (SRR) filter based on barium-strontium-titanate thick film," *7th German Microwave Conference (GeMiC),* pp. 1-4, 2012.

[41] M. Roig, M. Sazegar, Z. Yuliang, and R. Jakoby, "Tunable Frequency Selective Surface based on ferroelectric ceramics for beam steering antennas," *7th German Microwave Conference (GeMiC),* pp. 1-4, 2012.

[42] M. Sazegar, A. Giere, Z. Yuliang, H. Maune, A. Moessinger, and R. Jakoby, "Reconfigurable unit cell for reflectarray antenna based on barium-strontium-titanate thick-film ceramic," *European Microwave Conference (EuMC),* pp. 598-601, 2009.

[43] A. Giere, Y. Zheng, H. Gieser, K. Marquardt, H. Wolf, P. Scheele, and R. Jakoby, "Coating of planar barium-strontium-titanate thick-film varactors to increase tunability," *European Microwave Conference, ,* pp. 114-117, 2007.

[44] Y. Fan and Y. Rahmat-Samii, "Patch antennas with switchable slots (PASS) in wireless communications: concepts, designs, and applications," *IEEE Antennas and Propagation Magazine,* vol. 47, pp. 13-29, 2005.

[45] Y. Fan and Y. Rahmat-Samii, "A reconfigurable patch antenna using switchable slots for circular polarization diversity," *IEEE Microwave and Wireless Components Letters,* vol. 12, pp. 96-98, 2002.

[46] M. K. Fries, M. Grani, and R. Vahldieck, "A reconfigurable slot antenna with switchable polarization," *IEEE Microwave and Wireless Components Letters,* vol. 13, pp. 490-492, 2003.

[47] R. N. Simons, C. Donghoon, and L. P. B. Katehi, "Polarization reconfigurable patch antenna using microelectromechanical systems (MEMS) actuators," *IEEE Antennas and Propagation Society International Symposium,* vol. 2, pp. 6-9, 2002.

[48] P. J. Rainville and F. J. Harackiewicz, "Magnetic tuning of a microstrip patch antenna fabricated on a ferrite film," *IEEE Microwave and Guided Wave Letters,* vol. 2, pp. 483-485, 1992.

[49] P. Clarricoats and H. Zhou, "Design and performance of a reconfigurable mesh reflector antenna. Part 1: Antenna design ", 1991, pp. 485-492.

[50] G. Washington, Y. Hwan-Sik, M. Angelino, and W. H. Theunissen, "Design, modeling, and optimization of mechanically reconfigurable aperture antennas," *IEEE Transactions on Antennas and Propagation,* vol. 50, pp. 628-637, 2002.

[51] D. Sievenpiper and J. Schaffner, "Beam steering microwave reflector based on electrically tunable impedance surface," *Electronics Letters,* vol. 38, pp. 1237-1238, 2002.

[52] D. Sievenpiper, J. Schaffner, J. J. Lee, and S. Livingston, "A steerable leaky-wave antenna using a tunable impedance ground plane," *IEEE Antennas and Wireless Propagation Letters,* vol. 1, pp. 179-182, 2002.

[53] C. Jung-Chih, F. Yiton, C. Iao Mak, M. DeLisio, and L. Lih-Yuan, "MEMS reconfigurable Vee antenna," *IEEE MTT-S International Microwave Symposium Digest,* vol. 4, pp. 1515-1518, 1999.

[54] R. Harrington, "Reactively controlled directive arrays," *IEEE Transactions on Antennas and Propagation,* vol. 26, pp. 390-395, 1978.

[55] R. Schlub, L. Junwei, and T. Ohira, "Seven-element ground skirt monopole ESPAR antenna design from a genetic algorithm and the finite element method," *IEEE Transactions on Antennas and Propagation,* vol. 51, pp. 3033-3039, 2003.

[56] D. V. Thiel, "Switched parasitic antennas and controlled reactance parasitic antennas: a systems comparison," *IEEE Antennas and Propagation Society International Symposium,* vol. 3, pp. 3211-3214, 2004.

[57] R. Dinger, "Reactively steered adaptive array using microstrip patch elements at 4 GHz," *IEEE Transactions on Antennas and Propagation,* vol. 32, pp. 848-856, 1984.

[58] S. Zhang, G. H. Huff, J. Feng, and J. T. Bernhard, "A pattern reconfigurable microstrip parasitic array," *IEEE Transactions on Antennas and Propagation,* vol. 52, pp. 2773-2776, 2004.

[59] G. H. Huff, J. Feng, S. Zhang, and J. T. Bernhard, "A novel radiation pattern and frequency reconfigurable single turn square spiral microstrip antenna," *IEEE Microwave and Wireless Components Letters,* vol. 13, pp. 57-59, 2003.

[60] C. Shing-Hau, R. Jeen-Sheen, and W. Kin-Lu, "Reconfigurable Square-Ring Patch Antenna With Pattern Diversity," *IEEE Transactions on Antennas and Propagation,* vol. 55, pp. 472-475, 2007.

[61] A. Henderson, J. R. James, A. Fray, and G. D. Evans, "New ideas for beam scanning using magnetised ferrite," *IEEE Colloquium on Electronically Scanned Antennas,* pp. 1-4, 1988.

[62] G. Lovat, P. Burghignoli, and S. Celozzi, "A Tunable Ferroelectric Antenna for Fixed-Frequency Scanning Applications," *IEEE Antennas and Wireless Propagation Letters,* vol. 5, pp. 353-356, 2006.

[63] V. K. Varadan, V. V. Varadan, K. Jose, and J. F. Kelly, "Electronically steerable leaky wave antenna using a tunable ferroelectric material," *Smart Materials and Structures,* vol. 3, p. 470, 1994.

[64] Y. Yashchyshyn and J. W. Modelski, "Rigorous analysis and investigations of the scan antennas on a ferroelectric substrate," *IEEE Transactions onMicrowave Theory and Techniques,* vol. 53, pp. 427-438, 2005.

[65] L. N. Pringle, P. H. Harms, S. P. Blalock, G. N. Kiesel, E. J. Kuster, P. G. Friederich, R. J. Prado, J. M. Morris, and G. S. Smith, "A reconfigurable aperture antenna based on switched links between electrically small metallic patches," *IEEE Transactions on Antennas and Propagation,* vol. 52, pp. 1434-1445, 2004.

[66] P. Yaghmaee, T. Kaufmann, B. Bates, and C. Fumeaux, "Effect of polyimide layers on the permittivity tuning range of liquid crystals," *6th European Conference on Antennas and Propagation,* pp. 3579-3582, 2012.

[67] F. Reinitzer, *Monatsch Chem,* vol. 9, pp. 421-546, 1888.

[68] O. Lehmann, "Über fliessende Krystalle," *Z. Phys. Chem,* vol. 4, pp. 462–472, 1889.

[69] H. Kawamoto, "The history of liquid-crystal displays," *Proceedings of the IEEE,* vol. 90, pp. 460-500, 2002.

[70] N. V. Kamanina, "*Features of Liquid Crystal Display Materials and Processes,*" InTech, 2011.

[71] S. Mueller, A. Penirschke, C. Damm, P. Scheele, M. Wittek, C. Weil, and R. Jakoby, "Broad-band microwave characterization of liquid crystals using a temperature-controlled coaxial transmission line," *IEEE Transactions on Microwave Theory and Techniques* vol. 53, pp. 1937-1945, 2005.

[72] W. H. Jeu, "*Physical properties of liquid crystalline materials,*" Gordon and Breach, United States, 1979.

[73] P.-G. de Gennes, J. Prost, and R. Pelcovits, "The physics of liquid crystals," *Physics Today,* vol. 48, p. 70, 1995.

[74] W. Morris, "*The American heritage dictionary of the English language,*" Houghton Mifflin Boston, United States, 1981.

[75] J. Pearsall and P. Hanks, "*The new Oxford dictionary of English,*" Clarendon Press, United Kingdom, 1998.

[76] A. Gaebler, F. Goelden, S. Mueller, and R. Jakoby, "Efficiency considerations of tuneable liquid crystal microwave devices," *German Microwave Conference,* pp. 1-4, 2008.

[77] S. Mueller, M. Koeberle, F. Goelden, A. Penirschke, A. Gaebler, A. Lapanik, W. Haase, and R. Jakoby, "W-band characterization of anisotropic liquid crystals at room temperature," *38th European Microwave Conference,* pp. 119-122, 2008.

[78] K. Yoshino, M. Inoue, H. Moritake, and K. Toda, "Study of orientation of liquid crystal molecules at interface by shear horizontal wave," *14th International Conference on Dielectric Liquids,* pp. 386-389, 2002.

[79] Y. Garbovskiy, L. Reisman, Z. Celinski, R. E. Camley, and A. Glushchenko, "Metallic surfaces as alignment layers for nondisplay applications of liquid crystals," *Applied Physics Letters,* vol. 98, pp. 073301-073301-3, 2011.

[80] P. G. de Gennes, J. Prost, and R. Pelcovits, "The physics of liquid crystals," *Physics Today,* vol. 48, p. 70, 1995.

[81] A. Gaebler, A. Moessinger, F. Goelden, A. Manabe, M. Goebel, R. Follmann, D. Koether, C. Modes, A. Kipka, M. Deckelmann, T. Rabe, B. Schulz, P. Kuchenbecker, A. Lapanik, S. Mueller, W. Haase, and R. Jakoby, "Liquid crystal-reconfigurable antenna concepts for space applications at microwave and millimeter waves," *International Journal of Antennas and Propagation,* 2009.

[82] V. G. Chigrinov, "*Liquid crystal devices: physics and applications,*" Artech House Publishers, United Kingdom, 1999.

[83] G. Perez-Palomino, J. A. Encinar, and M. Barba, "Accurate electromagnetic modeling of liquid crystal cells for reconfigurable reflectarrays," *Proceedings of the 5th European Conference on Antennas and Propagation* pp. 997-1001, 2011.

[84] A. Petosa, "An overview of tuning techniques for frequency-agile antennas," *IEEE Antennas and Propagation Magazine,* vol. 54, pp. 271-296, 2012.

[85] I.-C. Khoo, Wu, Shin-Tson, "*Optics and nonlinear optics of liquid crystals,*" World Scientific Publishing, Singapore, 1993.

[86] K. Truesdale, "The Measurement of RF-Antenna Near Field Patterns Using Liquid Crystal Sensors," *IEEE GMTT International Microwave Symposium,* pp. 39-42, 1972.

[87] A. Derneryd, "A theoretical investigation of the rectangular microstrip antenna element," *IEEE Transactions on Antennas and Propagation,* vol. 26, pp. 532-535, 1978.

[88] J. F. Bernigaud, N. Martin, P. Laurent, C. Quendo, G. Tanne, B. Della, F. Huret, and P. Gelin, "Liquid crystal tunable filter based on DBR topology," *36th European Microwave Conference,* pp. 368-371, 2006.

[89] W. Hu, M. Y. Ismail, R. Cahill, H. S. Gamble, R. Dickie, V. F. Fusco, D. Linton, S. P. Rea, and N. Grant, "Tunable liquid crystal reflectarray patch element," *Electronics Letters,* vol. 42, pp. 509-511, 2006.

[90] N. Martin, P. Laurent, C. Person, M. Le Roy, A. Perennec, P. Gelin, and F. Huret, "Influence of design liquid crystal-based devices on the agility capability," *IEEE MTT-S International Microwave Symposium Digest,* p. 4, 2005.

[91] M. Y. Ismail and R. Cahill, "Application of liquid crystal technology for electronically scanned reflectarrays," *Asia-Pacific Conference on Applied Electromagnetics,* p. 4, 2005.

[92] D. Dolfi, M. Labeyrie, P. Joffre, and J. P. Huignard, "Liquid crystal microwave phase shifter," *Electronics Letters,* vol. 29, pp. 926-928, 1993.

[93] C. Weil, G. Luessem, and R. Jakoby, "Tunable inverted-microstrip phase shifter device using nematic liquid crystals," *IEEE MTT-S International Microwave Symposium Digest,* vol. 1, pp. 367-370, 2002.

[94] T. Kuki, H. Fujikake, H. Kamoda, and T. Nomoto, "Microwave variable delay line using a membrane impregnated with liquid crystal," *IEEE MTT-S International Microwave Symposium Digest,* vol. 1, pp. 363-366, 2002.

[95] N. Martin, P. Laurent, C. Person, P. Gelin, and F. Huret, "Patch antenna adjustable in frequency using liquid crystal," *33rd European Microwave Conference,* vol. 2, pp. 699-702, 2003.

[96] N. Martin, P. Laurent, C. Person, P. Gelin, and F. Huret, "Size reduction of a liquid crystal-based on frequency-adjustable patch antenna," *34th European Microwave Conference,* vol. 2, pp. 825-828, 2004.

[97] R. Marin, A. Mossinger, J. Freese, A. Manabe, and R. Jakoby, "Realization of 35 GHz steerable reflectarray using highly anisotropic liquid crystal," *IEEE Antennas and Propagation Society International Symposium,* pp. 4307-4310, 2006.

[98] R. Marin, A. Mossinger, J. Freese, S. Muller, and R. Jakoby, "Basic investigations of 35 GHz reflectarrays and tunable unit-cells for beamsteering applications," *European Radar Conference,* pp. 291-294, 2005.

[99] W. Hu, M. Y. Ismail, R. Cahill, J. A. Encinar, V. Fusco, H. S. Gamble, D. Linton, R. Dickie, N. Grant, and S. P. Rea, "Liquid-crystal-based reflectarray antenna with electronically switchable monopulse patterns," *Electronics Letters,* vol. 43, 2007.

[100] D. E. Schaub and D. R. Oliver, "A circular patch resonator for the measurement of microwave permittivity of nematic liquid crystal," *IEEE Transactions on Microwave Theory and Techniques,* vol. 59, pp. 1855-1862, 2011.

[101] A. Moessinger, R. Marin, J. Freese, S. Mueller, A. Manabe, and R. Jakoby, "Investigations on 77 GHz tunable reflectarray unit cells with liquid crystal," *First European Conference on Antennas and Propagation,* pp. 1-4, 2006.

[102] G. Perez-Palomino, J. A. Encinar, M. Barba, and E. Carrasco, "Design and evaluation of multi-resonant unit cells based on liquid crystals for reconfigurable reflectarrays," *IET Microwaves, Antennas & Propagation,* vol. 6, pp. 348-354, 2012.

[103] G. Perez-Palomino, P. Baine, R. Dickie, M. Bain, J. A. Encinar, R. Cahill, M. Barba, and G. Toso, "Design and experimental validation of liquid crystal-based reconfigurable reflectarray elements with improved bandwidth in F-band," *IEEE Transactions on Antennas and Propagation,* vol. 61, pp. 1704-1713, 2013.

[104] H. Wenfei, R. Cahill, J. A. Encinar, R. Dickie, H. Gamble, V. Fusco, and N. Grant, "Design and measurement of reconfigurable millimeter wave reflectarray cells with nematic liquid crystal," *IEEE Transactions on Antennas and Propagation,* vol. 56, pp. 3112-3117, 2008.

[105] O. H. Karabey, S. Bausch, S. Bildik, S. Strunck, A. Gaebler, and R. Jakoby, "Design and application of a liquid crystal varactor based tunable coupled line for polarization agile antennas," *42nd European Microwave Conference,* pp. 739-742, 2012.

[106] H. Wenfei, R. Dickie, R. Cahill, H. Gamble, Y. Ismail, V. Fusco, D. Linton, N. Grant, and S. Rea, "Liquid crystal tunable mm wave frequency selective surface," *IEEE Microwave and Wireless Components Letters,* vol. 17, pp. 667-669, 2007.

[107] F. Zhang, Q. Zhao, L. Kang, D. P. Gaillot, Z. Xiaopeng, J. Zhou, and D. Lippens, "Magnetic control of negative permeability metamaterials based on liquid crystals," *38th European Microwave Conference (EuMC),* pp. 801-804, 2008.

[108] J. A. Bossard, L. Xiaotao, L. Ling, Y. Seokho, D. H. Werner, B. Weiner, T. S. Mayer, P. F. Cristman, A. Diaz, and I. C. Khoo, "Tunable frequency selective surfaces and negative-zero-positive index metamaterials based on liquid crystals," *IEEE Transactions on Antennas and Propagation,* vol. 56, pp. 1308-1320, 2008.

[109] I. C. Khoo, A. Diaz, J. Bossard, X. Liang, and D. Werner, "Nano-dispersed liquid crystalline structures for tunable negative-, zero-, and positive index materials in the optical-terahertz regimes," *International Symposium on Biophotonics, Nanophotonics and Metamaterials,* pp. 412-416, 2006.

[110] J. A. Bossard, L. Li, D. H. Werner, and I. C. Khoo, "Infrared liquid crystal tunable frequency selective surfaces," *IEEE Antennas and Propagation Society International Symposium* pp. 4489-4492, 2006.

[111] "Documents of the International Radio Conference," p. 466, 1947.

[112] R. Bose and A. Sinha, "Tunable patch antenna using a liquid crystal substrate," *IEEE Radar Conference,* pp. 1-6, 2008.

[113] L. Luyi and R. Langley, "Electrically small antenna tuning techniques," *Antennas and Propagation Conference,* pp. 313-316, 2009.

[114] C. A. Balanis, "*Antenna Theory: Analysis and Design,*" J. Wiley, New York, 1982.

[115] C. Coleman, "*An Introduction to Radio Frequency Engineering,*" Cambridge University Press, United Kingdom, 2004.

[116] (25 August 2013). *National Instruments Company (AWR)*. Available: http://awrcorp.com

[117] (15 January 2013). *Computer Simulation Technology (CST)*. Available: http://www.cst.com/

[118] S. T. Wu and D. K. Yang, "*Fundamentals of Liquid Crystal Devices,*". United States: Wiley, 2006.

[119] B. Bahadur, *Liquid Crystals: Applications and Uses*. Singapore: World Scientific Publishing Company Incorporated, 1990.

[120] P. Yaghmaee, C. Fumeaux, B. Bates, A. Manabe, O. H. Karabey, and R. Jakoby, "Frequency tunable S-band resonator using nematic liquid crystal," *IET Electronics Letters,* vol. 48, 2012.

[121] C. Wei-Shin and C. Chi-Yang, "Analytical design of microstrip short-circuit terminated stepped-impedance resonator dual-band filters," *IEEE Transactions on Microwave Theory and Techniques,* vol. 59, pp. 1730-1739, 2011.

[122] H. Zhang-Cheng and H. Jia-Sheng, "Ultra wideband bandpass filter using embedded stepped impedance resonators on multilayer liquid crystal polymer substrate," *IEEE Microwave and Wireless Components Letters,* vol. 18, pp. 581-583, 2008.

[123] Z. C. Hao, J. S. Hong, S. K. Alotaibi, J. P. Parry, and D. P. Hand, "Ultra-wideband bandpass filter with multiple notch-bands on multilayer liquid crystal polymer substrate," *IET Microwaves, Antennas & Propagation,* vol. 3, pp. 749-756, 2009.

[124] S. Pinel, R. Bairavasubramanian, J. Laskar, and J. Papapolymerou, "Compact planar and vialess composite low-pass filters using folded stepped-impedance resonator on liquid-Crystal-polymer substrate," *IEEE Transactions on Microwave Theory and Techniques,* vol. 53, pp. 1707-1712, 2005.

[125] S. K. Hashemi, "Lumped-element equivalent circuit models for multilayer ring resonators filters," *IEEE International Conference on Ultra-Wideband (ICUWB),* pp. 512-515, 2011.

[126] J. G. Hong and M. J. Lancaster, *Microstrip Filters for RF/Microwave Applications*. United States: Wiley-Interscience, 2001.

[127] H. R. Kaupp, "Characteristics of microstrip transmission lines," *IEEE Transactions on Electronic Computers,* vol. 16, pp. 185-193, 1967.

[128] (25 August 2013). *Advanced Design System (ADS)*. Available: http://agilent.com

[129] W. Withayachumnankul, C. Fumeaux, and D. Abbott, "Planar array of electric-LC resonators with broadband tunability," *IEEE Antennas and Wireless Propagation Letters,* vol. 10, pp. 577-580, 2011.

[130] Q. Cheng, T. J. Cui, W. X. Jiang, and B. G. Cai, "An omnidirectional electromagnetic absorber made of metamaterials," *New Journal of Physics,* vol. 12, p. 063006, 2010.

[131] S. Fallahzadeh, K. Forooraghi, and Z. Atlasbaf, "A polarization-insensitive metamaterial absorber with a broad angular band," in *20th Iranian Conference on Electrical Engineering (ICEE)*, 2012, pp. 1540-1543.

[132] B. Zhu, Y. Feng, J. Zhao, C. Huang, and T. Jiang, "Switchable metamaterial reflector/absorber for different polarized electromagnetic waves," *Applied Physics Letters,* vol. 97, pp. 051906-051906-3, 2010.

[133] H.-T. Chen, W. J. Padilla, M. J. Cich, A. K. Azad, R. D. Averitt, and A. J. Taylor, "A metamaterial solid-state terahertz phase modulator," *Nature Photonics,* vol. 3, pp. 148-151, 2009.

[134] J. Y. Chin, L. Mingzhi, and T.-J. Cui, "Metamaterial polarizers by electric-field-coupled resonators," *Applied Physics Letters,* vol. 93, pp. 251903-251903-3, 2008.

[135] B. Zhu, Y. F. J. Zhao, C. Huang, Z. Wang, and T. Jiang, "Polarization modulation by tunable electromagnetic metamaterial reflector/absorber," *arXiv preprint arXiv:1010.4378,* 2010.

[136] J. A. Gordon, C. L. Holloway, J. Booth, S. Kim, Y. Wang, J. Baker-Jarvis, and D. R. Novotny, "Fluid interactions with metafilms/metasurfaces for tuning, sensing, and microwave-assisted chemical processes," *Physical Review,* vol. 83, p. 205130, 2011.

[137] A. K. Horestani, C. Fumeaux, S. F. Al-Sarawi, and D. Abbott, "Split ring resonators with tapered strip width for wider bandwidth and enhanced resonance," *IEEE Microwave and Wireless Components Letters,* vol. 22, pp. 450-452, 2012.

[138] (06 October 2013). *AutoCAD*. Available: http://www.autodesk.com

[139] D. M. Pozar, "*Microwave Engineering*": John Wiley & Sons, United States, 2009.

[140] (08 September 2013). *Material dielectric constant*. Available: http://www.clippercontrols.com/pages/Dielectric-Constant-Values.html

[141] X. Geng, Y. Yong, D. Lu, and S. Zhao, "Dielectric log-A logging method for determining oil saturation," *Journal of Petroleum Technology,* vol. 35, pp. 1797-1805, 1983.

[142] S. RB, M. Halleraker, and B. Engebretsen, "Advanced profile gauge for multiphase systems," *1st Word Congress on Industrial Process Tomography* 1999.

Physical constants

The physical constants used in this thesis are in accordance with a recommendation of the Committee on Data for Science and Technology (Mohr and Taylor 2005).

Quantity	Symbol	Value
vacuum permittivity (electronic constant)	ε_0	8.8541 187 817 …× 10^{-12} F/m
vacuum permittivity (magnetic constant)	μ_0	$4\pi \times 10^{-7}$ N/A^2
speed of light in vacuum	c	299 792 458 m/s

Acronyms

FSS	frequency selective surfaces, 3
MEMS	micro-electromechanical systems, 5
CPW	coplanar waveguide, 6
BST	barium strontium titanate, 9
MOCVD	metalorganic chemical vapour deposition, 9
IDC	interdigitated capacitor, 10
SRR	split ring resonators, 10
RHCP	right-hand circular polarization, 11
LHCP	left-hand circular polarization, 11
DCBRA	dual-offset contour beam reflector antenna, 13
LCP	liquid crystal polymer, 36
ISM	industrial, scientific and medical, 43
PEC	perfect electric conductor, 47
CST	Computer Simulation Technology, 48
DSTO	Defence Science and Technology Organization, 55
TUD	Technische Universität Darmstadt, 68
PI	polyimide film, 68
LCD	liquid crystal display. 71
SIR	stepped-impedance resonators, 79
LCP	liquid crystal polymer, 79
MRR	multi-layer ring resonator,80
ADS	advanced design system, 82
ELC	electric inductor capacitor, 93
ANFF	Australian National Fabrication Facility, 109

Biography

Pouria Yaghmaee was born in Tehran, Iran in 1983. From 2001 to 2006, he was educated at Tehran University-Azad Central, in his home town, where he obtained a Bachelor's Degree in Electrical Engineering-Electronics Engineering. While working at Prof Mahmoud Hessaby research centre during his undergraduate degree, he became interested in RF analog designs.

In 2007, he was given an offer of Master's degree in the field of Telecommunications Engineering from the University of Adelaide, Australia, where he completed a advanced postgraduate degree under supervision of Dr Behnam Jamali and Prof Peter Cole on RFID readers. In 2010, he was granted both an Australian Postgraduate Awards (APAs) and Divisional Scholarship from Australian Federal Government and University of Adelaide respectively to undertake Doctor of Philosophy (PhD) in Electrical Engineering, under Adj Prof Bevan Bates and Prof Christophe Fumeaux.

Since 2010, he has been with the Applied Electromagnetics Group as a researcher working on reconfigurable/tunable microwave structures. In summer 2011, he was a visiting researcher at Institution of Microwave and Photonics, Technische Universität Darmstadt and Merck KGaA laboratory in Germany working on a collaborative project. During his PhD candidate, Mr Yaghmaee was a reviewer for EDAS conference services, tutor and demonstrator for over ten undergraduate and postgraduate courses, IEEE South Australia invited guest speaker at Defence Science and Technology Organization and was awarded the 2nd prize for South Australian microscopic competition.

Pouria Yaghmaee
pouria@eleceng.adelaide.edu.au

Scientifc Genealogy of

Pouria Yaghmaee

Formalised supervisor relationship
Mentoring relationship
Nobel prize

"If I have seen further it is by standing on the shoulders of Giants."
Isaac Newton